

Spring 2021

## Exploring QCD Factorization at Moderate Energy Scales

Eric Alan Moffat

*Old Dominion University*, [emoff003@odu.edu](mailto:emoff003@odu.edu)

Follow this and additional works at: [https://digitalcommons.odu.edu/physics\\_etds](https://digitalcommons.odu.edu/physics_etds)



Part of the [Elementary Particles and Fields and String Theory Commons](#), [Nuclear Commons](#), and the [Quantum Physics Commons](#)

---

### Recommended Citation

Moffat, Eric A.. "Exploring QCD Factorization at Moderate Energy Scales" (2021). Doctor of Philosophy (PhD), Dissertation, Physics, Old Dominion University, DOI: 10.25777/weqn-7x05  
[https://digitalcommons.odu.edu/physics\\_etds/131](https://digitalcommons.odu.edu/physics_etds/131)

This Dissertation is brought to you for free and open access by the Physics at ODU Digital Commons. It has been accepted for inclusion in Physics Theses & Dissertations by an authorized administrator of ODU Digital Commons. For more information, please contact [digitalcommons@odu.edu](mailto:digitalcommons@odu.edu).

# EXPLORING QCD FACTORIZATION AT MODERATE ENERGY SCALES

by

Eric Alan Moffat

B.S. December 2002, Purdue University

M.S. December 2015, Old Dominion University

A Dissertation Submitted to the Faculty of  
Old Dominion University in Partial Fulfillment of the  
Requirements for the Degree of

DOCTOR OF PHILOSOPHY

PHYSICS

OLD DOMINION UNIVERSITY

May 2021

Approved by:

Ted Rogers (Director)

Anatoly Radyushkin (Member)

Wally Van Orden (Member)

Sebastian Kuhn (Member)

John Adam (Member)

## ABSTRACT

### EXPLORING QCD FACTORIZATION AT MODERATE ENERGY SCALES

Eric Alan Moffat  
Old Dominion University, 2021  
Director: Dr. Ted Rogers

Asymptotic freedom in QCD facilitates the use of partonic degrees of freedom over short distances, but physical processes are sensitive to a wide range of scales. Thus, it is necessary in QCD calculations to utilize a factorization scheme to separate a process into perturbative and non-perturbative factors. This separation relies on an assumption that one energy scale is infinitely larger than the other scales involved in the process. However, much experimental research in areas such as nucleon structure and quark-hadron duality occur at more moderate energy scales where that basic assumption may not be true but perturbative calculations should still be useful. Thus, an exploration of the limits of factorization at more moderate energy scales is needed. This dissertation examines various aspects of factorization at these energy scales first by applying the necessary approximations to a simple model where exact calculations are possible and so the effects of these approximations can be quantified. This is followed by examining areas where corrections are known to be needed. First is an exploration of target mass corrections (TMCs) in the case of deep inelastic scattering (DIS), including a discussion of what large corrections imply about the target structure. Second, is a general examination of PDFs and FFs at moderate scales. Third, I will discuss how this fits into the long-term effort to study the transition between small transverse momentum (generated non-perturbatively) and large transverse momentum (generated in the hard process).

This thesis is dedicated to my mother and father who always believed in me.

## ACKNOWLEDGEMENTS

Throughout the writing of this dissertation I have received a great deal of support and assistance.

First and foremost, I'd like to express my deepest gratitude to my advisor Ted Rogers for his guidance and patience throughout my time as a PhD student.

I would also like to thank the other members of my dissertation committee, namely Anatoly Radyushkin, Wally Van Orden, Sebastian Kuhn, and John Adam for their insights on the development of this thesis.

I'm also extremely grateful to Nobuo Sato, Wally Melnitchouk, Fernanda Steffens, and Andrea Signori whose collaboration over the years resulted in several publications based on this work.

## TABLE OF CONTENTS

	Page
LIST OF TABLES .....	vii
LIST OF FIGURES .....	ix
Chapter	
1. INTRODUCTION .....	1
2. QCD PROCESSES .....	8
2.1 DIS KINEMATICS .....	8
2.2 SEMI-INCLUSIVE $e^+/e^-$ ANNIHILATION KINEMATICS .....	13
2.3 DRELL-YAN KINEMATICS .....	20
3. COLLINEAR FACTORIZATION IN INCLUSIVE DIS .....	23
4. EXPLORING FACTORIZATION USING A SIMPLE FIELD THEORY .....	30
4.1 DIS IN A SIMPLE MODEL .....	31
4.2 EXACT KINEMATICS .....	36
4.3 FACTORIZATION .....	41
4.4 EXACT AND FACTORIZED STRUCTURE FUNCTIONS: A COM- PARISON .....	44
5. TARGET MASS CORRECTIONS .....	61
5.1 MASSLESS TARGET APPROXIMATION (MTA) .....	63
5.2 THE MTA AND COLLINEAR FACTORIZATION .....	66
5.3 CONTRAST WITH OTHER TMC METHODS .....	71
5.4 WHEN ARE TARGET MASS KINEMATICS RELEVANT? .....	73
6. TRANSVERSE MOMENTUM DEPENDENCE IN $e^+/e^-$ ANNIHILATION .....	81
6.1 FACTORIZATION AT LARGE, MODERATE, AND SMALL TRANS- VERSE MOMENTUM .....	84
6.2 TRANSVERSE MOMENTUM HARDNESS .....	92
6.3 LARGE AND SMALL TRANSVERSE MOMENTUM COMPARISON ..	95
7. EXPLORING TRANSVERSE MOMENTUM DEPENDENCE IN SIDIS USING A NEW PDF AND FF FIT .....	100
7.1 THEORETICAL FRAMEWORK .....	102

	Page
7.2 DATA SETS .....	112
7.3 ASSESSING UNIVERSALITY .....	115
7.4 NUMERICAL ANALYSIS .....	117
7.5 TRANSVERSE MOMENTUM DEPENDENT SIDIS PREDICTIONS ...	133
8. CONCLUSIONS.....	135
BIBLIOGRAPHY .....	142
VITA .....	158

## LIST OF TABLES

Table	Page
1. Ratios of exact to collinear integrated structure functions .....	54
2. $\chi_{\text{red}}^2$ results by process .....	120

## LIST OF FIGURES

Figure	Page
1. The DIS process .....	9
2. The SIDIS process .....	12
3. The single hadron SIA process .....	14
4. The hadron pair SIA process .....	16
5. $e^+/e^-$ annihilation photon frame .....	17
6. Illustration of dilepton production from the DY process.....	20
7. Basic handbag diagram for inclusive DIS. ....	24
8. The sequence of approximations leading to the canonical parton model .....	33
9. Diagrams contributing to the DIS hadronic tensor in the simple field theory.....	36
10. Results of collinear factorization in the simple field theory.....	41
11. Exact and approximated unintegrated structure functions .....	49
12. Parton virtuality vs. $k_T$ in the simple field theory .....	51
13. Impact of the replacement $x_{Bj} \rightarrow x_N$ .....	57
14. DIS from a composite target.....	67
15. DIS from a subsystem within a composite target .....	75
16. Contributing diagrams for hadron pair production in SIA .....	86
17. Order $\alpha_s$ partonic channels .....	87
18. LO collinear factorization predictions.....	97

Figure	Page
19. FO calculations compared with simulated data .....	99
20. Schematic illustration of the multi-step workflow .....	112
21. Kinematic coverage of data .....	113
22. $\chi_{\text{red}}^2$ values .....	118
23. Pion SIDIS data and theory .....	121
24. Kaon SIDIS data and theory .....	122
25. Charged hadron SIDIS data and theory .....	122
26. Pion SIA data over theory .....	123
27. Kaon SIA data over theory .....	124
28. Charged hadron SIA data over theory .....	124
29. PDF results .....	127
30. FF results .....	128
31. FF Normalized yields.....	130
32. Strange PDF suppression .....	132
33. Comparison of theoretical predictions to SIDIS data. ....	134

## CHAPTER 1

### INTRODUCTION

Since the Rutherford gold foil experiments in the early 1900s revealed the presence of a positively charged nucleus within the atom [1], understanding nuclear structure and the forces that bind it together has been a prominent goal in physics research. Further research by Rutherford demonstrated that the hydrogen nucleus (eventually called the proton) was contained in other nuclei [2]. Then in 1932, research by James Chadwick for which he won the Nobel prize in 1935, proved that neutral particles about the same mass as a proton called neutrons are also present in the nucleus [3, 4]. Nuclei consisting of protons and neutrons meant that a previously unknown force had to exist that was strong enough to counter the Coulomb repulsion between the positively charged protons.

Early theories for this strong nuclear force involved the nucleons (protons and neutrons) exchanging particles similar to the exchange of photons in electromagnetic interactions. The first example of such a theory, developed by Hideki Yukawa in 1935 [5], predicted these force carrying particles carried only a fraction of the nucleon mass. These particles were eventually called mesons and Yukawa was awarded the Nobel prize in 1949 after the lightest meson (the pion) was observed experimentally. In the 1950's and 60's a wide variety of other strongly interacting particles (called hadrons) were observed experimentally.

Though no constituent particles had ever been observed, in 1964 Murray Gell-Mann [6] and George Zweig [7, 8] independently devised a scheme for organizing the known hadrons in terms of three flavors of constituent particles. Gell-Mann called these particles quarks and the three flavors were up, down, and strange. Baryons (like protons and neutrons) were combinations of three quarks and mesons (like pions) were made of a quark and an anti-quark. The existence of baryons that consisted of three quarks of the same flavor ( $\Delta^{++}$  for example consists of three up quarks) led to the conclusion that quarks had to have an additional quantum number in order to avoid violating the Pauli exclusion principle [9–11]. This quantum number would eventually be called color charge. Quarks could be red,

green, or blue and anti-quarks could be anti-red, anti-green, or anti-blue and all hadrons were color neutral. It was also postulated that quarks could interact through the exchange of eight vector bosons [10, 11] which would eventually be called gluons. The quark model was initially met with skepticism as no experimental evidence of quarks had been found. Even in 1969 when deep inelastic scattering (DIS) of electrons and protons at SLAC demonstrated that the proton had an internal structure [12–14], scientists referred to the dynamical constituents as “partons” (originally coined by Richard Feynman [15]) rather than quarks. Eventually, the discovery of the charm quark through the observation of the  $J/\Psi$  meson solidified the belief that partons were quarks and gluons.

In 1973, the field theory of Quantum Chromodynamics (QCD) was introduced by Fritzsche, Gell-Mann, and Leutwyler [16] to express the strong nuclear force in terms of quarks, gluons, and color charge. QCD proved to come with difficulties, just a proton-proton collision at first glance would seem to be a six-body problem and impossible to solve analytically. This was not the limit of its complexity, however. Fortunately, in 1973, Gross and Wilczek and independently Politzer discovered that QCD and other field theories like it were asymptotically free [17, 18], allowing for controllable calculations over short distances. All three were awarded the Nobel Prize for this work in 2004. Asymptotic freedom means that the QCD coupling  $\alpha_s$  is smallest for high-energy, short-distance interactions and largest for small-energy, long-distance interactions. The consequence of this is that only the high-energy, short-distance portions of a QCD process (partonic or hard parts) can be accurately approximated by a truncated perturbative expansion in  $\alpha_s$ . Thus, a method for separating these hard portions of a process from those portions where perturbative calculations fail (non-perturbative parts) is needed. Factorization techniques are methods that achieve this separation.

Factorization techniques are prescriptions for applying approximations so that a particular QCD process can be separated into individual perturbative and non-perturbative factors. Specifically, they involve taking the limit that one energy scale  $Q$  (usually the momentum

scale of the exchanged particle) is significantly larger than the other energy scales involved ( $\Lambda_{QCD}$ , particle masses, parton virtualities, etc.) which will be referred to generically as  $m$ . Factorization amounts to expanding the expression for an observable in powers of  $m/Q$  and neglecting higher power terms. What remains is an approximation of the observable consisting of separate hard and non-perturbative factors. The two main types of factorization that will be discussed in this dissertation are collinear and transverse momentum dependent (TMD) factorization, transverse momentum being the  $x$  and  $y$  components of momentum. The axes of course vary from process to process and the choice of reference frame but typically the  $z$ -axis is defined by choosing two initial and/or final state particle momenta to be back-to-back. These details are reviewed for the processes included in this research in Chapter 2.

In the case of observables where the transverse momentum dependence has been integrated over, *collinear* factorization is the prescription used to obtain the approximated observable. An example of this is collinear factorization of the  $F_1$  structure function for inclusive lepton-hadron deep inelastic scattering (DIS) and the result is:

$$\begin{aligned} F_1(x_{Bj}, Q^2) &= \sum_{f,f'} \int_{x_{Bj}}^1 \frac{d\xi}{\xi} \widehat{\mathcal{F}}_{1,f/f'}(x_{Bj}/\xi, Q^2) f_{f'/p}(\xi) + O(m^2/Q^2) \\ &= \sum_{f,f'} \widehat{\mathcal{F}}_{1,f/f'} \otimes f_{f'/p} + O(m^2/Q^2). \end{aligned} \quad (1)$$

Here  $x_{Bj} = Q^2/2P \cdot q$  is the Bjorken scaling variable [19].  $P$  is the momentum of the hadron target and  $q$  is the momentum of the exchanged virtual photon with  $Q^2 = -q^2$ .  $\xi$  is the fraction of  $P^+$  carried by the parton. The hard factor  $\widehat{\mathcal{F}}_{1,f/f'}(x_{Bj}/\xi, Q^2)$  is simply a partonic level function analogous to the  $F_1$  structure function calculated perturbatively for the lepton scattering off of the target parton. The indices  $f$  and  $f'$  are the flavors of the final and initial parton respectively in the hard scatter. The non-perturbative factor  $f_{f'/p}(\xi)$  is a collinear parton distribution function (PDF) which represents the probability that the target parton  $f'$  coming from the target hadron ( $p$ ) will have a fraction  $\xi$  of the hadron's momentum. The

result is a convolution of hard factors with PDFs summed over all parton flavors  $f$  and  $f'$  which approximates  $F_1$  with an accuracy of order  $(m^2/Q^2)$ . In the second line of Eq. (1), the  $\otimes$  is shorthand notation for the convolution integral

$$(A \otimes B)(x) = \int_x^1 \frac{d\xi}{\xi} A(x/\xi) B(\xi). \quad (2)$$

Factorization in the case of transverse momentum dependent observables is more complex. This is because the required prescription for factorization depends on the scale of the transverse momentum relative to  $Q$ . When the transverse momentum is large ( $\gg \Lambda_{QCD}$ ), it is generated in the hard factor. In this case, collinear factorization is used to calculate the approximated observable. This contribution to the transverse momentum dependence is called the fixed order (FO) term. An example of collinear factorization for an observable that is dependent on transverse momentum would be the  $F_1$  structure function for large transverse momentum semi-inclusive DIS (SIDIS). This is DIS where the momentum of a hadron in the final state is measured. The resulting expression is:

$$\begin{aligned} F_1^{h,\text{FO}}(x_{\text{Bj}}, z_h, Q^2, \mathbf{P}_{h\text{T}}) &= \sum_{f,f'} \int \frac{d\xi}{\xi} \frac{d\zeta}{\zeta^2} \widehat{\mathcal{F}}_{1,f/f'}^h(x_{\text{Bj}}/\xi, z_h/\zeta, Q^2, \mathbf{P}_{h\text{T}}) f_{f'/p}(\xi) d_{h/f}(\zeta) \\ &\quad + O\left(\frac{m^2}{Q^2}\right), \\ &= \sum_{f,f'} \widehat{\mathcal{F}}_{1,f/f'}^h \otimes f_{f'/p} \otimes d_{h/f} + O\left(\frac{m^2}{Q^2}\right). \end{aligned} \quad (3)$$

Here the measured final state hadron ( $h$ ) has momentum  $P_h$  with transverse momentum  $\mathbf{P}_{h\text{T}} \gg m$ . The variable  $z_h$  is defined by the ratio  $z_h = (P \cdot P_h)/(P \cdot q)$  and  $\zeta$  is the fraction of the minus momentum of parton  $f$  carried by the final state hadron. Again, the factorized expression involves a convolution of a partonic structure function ( $\widehat{\mathcal{F}}_{1,f/f'}^h(x_{\text{Bj}}/\xi, z_h/\zeta, Q^2, \mathbf{P}_{h\text{T}})$ ) with a collinear PDF ( $f_{f'/p}(\xi)$ ), but there is also a convolution with a second non-perturbative factor.  $d_{h/f}(\zeta)$  is a collinear fragmentation function (FF) which is the probability of the final

state hadron having momentum fraction  $\zeta$ .

TMD factorization is used in the case where the transverse momentum is generated by non-perturbative interactions (intrinsic transverse momentum) and so is small ( $\mathbf{P}_{hT} \ll Q$ ). This contribution is known as the W term. The factorization of the  $F_1$  structure function in small transverse momentum SIDIS is an example of TMD factorization. The result is:

$$\begin{aligned}
 F_1^{h,W}(x_{Bj}, z_h, Q^2, \mathbf{P}_{hT}) = & \\
 & \sum_{f,f'} \widehat{\mathcal{F}}_{1,f/f'}^h(x_{Bj}, z_h, Q^2, \mathbf{P}_{hT}) \int \frac{d^2\mathbf{b}_T}{(2\pi)^2} e^{-i\mathbf{P}_{hT} \cdot \mathbf{b}_T} \tilde{f}_{f'/p}(x, \mathbf{b}_T; Q) \tilde{D}_{h/f}(z, \mathbf{b}_T; Q) \\
 & + O\left(\frac{m^2}{Q^2}\right). \tag{4}
 \end{aligned}$$

Here  $\tilde{f}$  and  $\tilde{D}$  are the inverse fourier transforms of a TMD pdf and a TMD ff respectively. These TMD non-perturbative functions not only give the probability of a particular momentum fraction but also a particular transverse momentum.

The approximations for the FO and W terms are not mutually exclusive. They overlap in the region where  $m \ll \mathbf{P}_{hT} \ll Q$ . Therefore to avoid double counting, a term where both approximations are applied must be subtracted. This contribution is called the asymptotic (ASY) term. In the case of the  $F_1$  structure function for SIDIS, the ASY term would be the limit of Eq. (3) when  $\mathbf{P}_{hT} \rightarrow 0$ . The difference between the FO term and the ASY term is usually referred to as the Y term and W+Y represents the full transverse momentum spectrum after factorization.

Factorized expressions like Eqs. 1, 3, and 4 work best in the extreme limit of  $m^2/Q^2 \rightarrow 0$ , which is where they have been most successfully applied. However, for research in phenomena of great interest in nuclear physics, such as quark-hadron duality and 3-D hadronic structure, valuable information lies in data at more moderate energy scales where  $Q$  is not so large and there extra considerations need to be taken into account. At these energies some of the energy scales typically included in the small scale  $m$  (such as the target hadron mass in DIS)

may actually be on the same order as  $Q$ . Therefore, a proper interpretation of data at these moderate energy scales requires careful application of factorization in which corrections due to the not so small scales are properly included. The goal of this dissertation is to review the basic steps of factorization and discuss improvements and enhancements that are needed at moderate  $Q$ .

To facilitate this exploration, I will first review the QCD processes that will be discussed in this dissertation. Chapter 2 provides a review of the kinematics and expressions associated with these processes. Along with inclusive DIS and SIDIS that have already been mentioned, this includes  $e^+/e^-$  annihilation and Drell-Yan (DY) hadron-hadron scattering. After this review, Chapter 3 begins the exploration of factorization by carefully reviewing the basic steps of collinear factorization in the case of inclusive DIS. Chapter 4 then demonstrates how the corrections to factorization can be examined by applying factorization to a simple field theory in which it is possible to perform the calculations without needing approximation. This allows examining the corrections quantitatively by directly comparing the factorized (approximated) solutions with the exact ones. This work specifically examines DIS in the simple theory.

One correction known to be necessary at moderate  $Q$  is the correction to factorization in DIS due to the mass of the target hadron. Though there are a number of different prescriptions for calculating target mass corrections (TMCs), Chapter 5 focuses on the method utilized by Aivazis, Olness and Tung (AOT) [20] in the context of heavy quark contributions in DIS. The chapter begins with describing the AOT methodology then discusses why this method has been chosen over the other TMC prescriptions. The chapter demonstrates that significant improvement relative to data when these corrections are included indicates a hierarchy of non-perturbative scales within the target.

Moderate  $Q$  also plays an important role in the transition between small transverse momentum where TMD factorization applies and large transverse momentum where collinear factorization is used. Chapter 6 explores this in the case of  $e^+/e^-$  annihilation with two mea-

sured final state hadrons. This is done by calculating and comparing graphically the W, FO, and ASY contributions to the cross-section. Doing this demonstrates that smaller  $Q$  leads to a wider transition region of transverse momentum where neither the W nor the FO alone represent the full value of the cross-section. Additionally, calculations of the large transverse momentum contributions to TMD observables in SIDIS [21–24] and hadron-hadron scattering (Drell-Yan) [25] have shown significant discrepancies between the theoretical FO calculations and data. In Chapter 6, the FO results are compared with simulated data generated using PYTHIA 8 [26, 27]. Simulated data was used because experimental data for hadron pair production from  $e^+/e^-$  annihilation was not available. Discrepancies between the FO predictions and the simulated data are visible particularly at lower  $Q$ .

The results of Chapter 6 motivated performing a new fit of collinear PDFs and FFs in order to determine if improvements in the fitted functions can help reduce the observed discrepancies between FO calculations and large transverse momentum data. Chapter 7 discusses the new fit which uses the same methodology used by the Jefferson Lab Angular Momentum (JAM) collaboration in the JAM19 [28] analysis of unpolarized PDFs and FFs. This method utilizes a Bayesian Monte Carlo approach to achieve a simultaneous extraction of the PDFs and FFs. The difference between this fit (called “JAM20-SIDIS”) and JAM19 is the inclusion of unidentified charged hadron data from COMPASS [29, 30] in the analysis. Theoretical predictions for large transverse momentum SIDIS using the results of the fit are then compared with transverse momentum dependent data from COMPASS [31].

Finally, Chapter 8 summarizes the results of this work and the conclusions drawn. Then potential future developments from this work are discussed.

## CHAPTER 2

### QCD PROCESSES

I begin with a review of the kinematics and relevant expressions for the various QCD processes that will be discussed throughout this work. These processes include lepton-hadron scattering (both inclusive DIS and SIDIS), semi-inclusive  $e^+/e^-$  annihilation (SIA), and dilepton production from hadron-hadron scattering (Drell-Yan (DY)).

#### 2.1 DIS kinematics

The DIS process is defined as a lepton scattering off of a single parton within a hadron target. The hadron breaks apart and jets of hadrons are produced. In inclusive DIS, the initial momenta of the lepton ( $l$ ) and target hadron ( $P$ ) and the final momentum of the lepton ( $l'$ ) are the measured kinematic variables. In addition to these, in SIDIS the momentum of a final state hadron ( $P_h$ ) is also measured. The conventions reviewed here follow those found in [32].

##### 2.1.1 Inclusive DIS

Fig. 1 illustrates electron-proton inclusive DIS given by the expression

$$e^-(l) + p(P) \rightarrow e^-(l') + X(P_X). \quad (5)$$

This process involves the exchange of a virtual photon of momentum  $q = l - l'$  and I define the energy scale of the process as  $Q = \sqrt{-q^2}$ . For DIS calculations it is convenient to work in what is called the Breit frame where the target hadron momentum is in the  $+z$  direction and the photon has momentum  $Q$  in the  $-z$  direction. The target, photon, and lepton four-momenta in this frame are

$$P^\mu = \left( \frac{Q}{\sqrt{2}x_N}, \frac{x_N M^2}{\sqrt{2}Q}, \mathbf{0}_T \right), \quad (6)$$

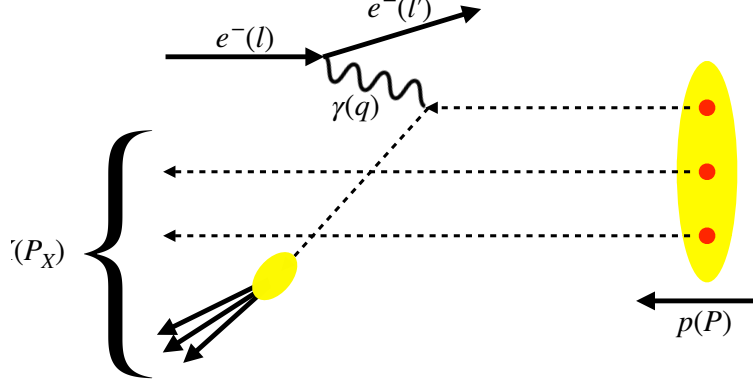


Figure 1: Illustration of the inclusive DIS process.

$$q^\mu = \left( -\frac{Q}{\sqrt{2}}, \frac{Q}{\sqrt{2}}, \mathbf{0}_T \right), \quad (7)$$

$$l^\mu = \left( \frac{Q(1-y)}{\sqrt{2}y}, \frac{Q}{\sqrt{2}y}, \left( \frac{Q\sqrt{1-y}}{y} \cos \phi, \frac{Q\sqrt{1-y}}{y} \sin \phi \right) \right), \quad (8)$$

$$l'^\mu = \left( \frac{Q}{\sqrt{2}y}, \frac{Q(1-y)}{\sqrt{2}y}, \left( \frac{Q\sqrt{1-y}}{y} \cos \phi, \frac{Q\sqrt{1-y}}{y} \sin \phi \right) \right). \quad (9)$$

Here I am using light-cone coordinates where  $v^\mu = (v^+, v^-, \mathbf{v}_T)$  with  $v^\pm = (v^0 \pm v^3) / \sqrt{2}$  and  $\mathbf{v}_T = (v^1, v^2)$ .  $M$  is the mass of the hadron target. The variable  $x_N$  is the Nachtmann scaling variable [33, 34] defined as  $x_N = -q^+ / P^+$ . This is related to the Bjorken scaling variable [19]  $x_{\text{Bj}} = Q^2 / 2P \cdot q$  by

$$x_N = \frac{2x_{\text{Bj}}}{1 + \sqrt{1 + \frac{4x_{\text{Bj}}^2 M^2}{Q^2}}} \text{ and } x_{\text{Bj}} = \frac{x_N}{1 - \frac{x_N^2 M^2}{Q^2}}. \quad (10)$$

Note that in the case where target masses are neglected,  $x_N = x_{\text{Bj}}$ . In the lepton momenta,  $\phi$  is the azimuthal angle of the lepton momentum and

$$y = \frac{P \cdot q}{P \cdot l} = \frac{Q^2}{x_{\text{Bj}}(s - M^2)}. \quad (11)$$

The invariant mass squared of the photon–nucleon system is

$$W^2 = (P + q)^2 = (p_q + p_s)^2 = M^2 + \frac{Q^2(1 - x_{\text{Bj}})}{x_{\text{Bj}}}. \quad (12)$$

The expression for the inclusive DIS cross section is

$$E' \frac{d\sigma_{\text{DIS}}}{d^3\mathbf{l}'} = \frac{2\alpha_{\text{em}}^2}{(s - M^2)Q^4} L_{\mu\nu} W_{\text{DIS}}^{\mu\nu} \quad (13)$$

where  $E'$  is the energy of the outgoing electron,  $\alpha_{\text{em}}$  is the electromagnetic fine structure constant, and  $s = (P + l)^2$  is the standard Mandelstam variable. Note I am neglecting the mass of the lepton. The two tensors in Eq. (13) are the leptonic tensor defined as

$$L_{\mu\nu} = 2 \left( l_\mu l'_\nu + l_\nu l'_\mu - g_{\mu\nu} (l \cdot l') \right) \quad (14)$$

and the hadronic tensor defined as

$$W_{\text{DIS}}^{\mu\nu}(P, q) = 4\pi^3 \sum_X \langle P, S | j^\mu(0) | X \rangle \langle X | j^\nu(0) | P, S \rangle \delta^{(4)}(q + P - P_X), \quad (15)$$

where  $\sum_X$  represents the sum over all final states  $|X\rangle$  which includes momentum integrals of the form

$$\int \frac{d^3\mathbf{p}_i}{2E_{p_i} (2\pi)^3}. \quad (16)$$

In the case of an unpolarized lepton scattering off of an unpolarized target, the structure function decomposition of the hadronic tensor is

$$\begin{aligned} W_{\text{DIS}}^{\mu\nu}(P, q) = & \left( -g^{\mu\nu} - \frac{q^\mu q^\nu}{Q^2} \right) F_1(x_{\text{Bj}}, Q^2) \\ & + \left( P^\mu + \frac{P \cdot q}{Q^2} q^\mu \right) \left( P^\nu + \frac{P \cdot q}{Q^2} q^\nu \right) \frac{F_2(x_{\text{Bj}}, Q^2)}{P \cdot q}. \end{aligned} \quad (17)$$

The structure functions can be obtained by contracting the hadronic tensor with extraction

tensors

$$F_i(x_{\text{Bj}}, Q^2) = P_i^{\mu\nu} W_{\mu\nu}^{\text{DIS}}(P, q), \quad i = 1, 2, \quad (18)$$

where

$$P_1^{\mu\nu} \equiv -\frac{1}{2}g^{\mu\nu} + \frac{2Q^2x_{\text{N}}^2}{(Q^2 + M^2x_{\text{N}}^2)^2}P^\mu P^\nu, \quad (19a)$$

$$P_2^{\mu\nu} \equiv \frac{12Q^4x_{\text{N}}^3(Q^2 - M^2x_{\text{N}}^2)}{(Q^2 + M^2x_{\text{N}}^2)^4} \left( P^\mu P^\nu - \frac{(Q^2 + M^2x_{\text{N}}^2)^2}{12Q^2x_{\text{N}}^2}g^{\mu\nu} \right). \quad (19b)$$

The inclusive DIS cross section is commonly presented as  $d\sigma_{\text{DIS}}/dx_{\text{N}}dy$  or  $d\sigma_{\text{DIS}}/dx_{\text{N}}dQ^2$ .

These can be obtained from Eq. (13) using the following change of variables:

$$\frac{d^3\mathbf{l}'}{E'} = \frac{dl'^+ dl'_{\text{T}} d\phi}{l'^+} = \frac{(s - M^2)y}{2} dx_{\text{N}} dy d\phi = \frac{y}{2x_{\text{N}}} dx_{\text{N}} dQ^2 d\phi, \quad (20)$$

and integrating over  $\phi$ . The results are

$$\frac{d\sigma_{\text{DIS}}}{dx_{\text{N}}dy} = \frac{Q^2}{y} \frac{d\sigma_{\text{DIS}}}{dx_{\text{N}}dQ^2} = \frac{2\pi\alpha_{\text{em}}^2 y}{Q^4} L_{\mu\nu} W_{\text{DIS}}^{\mu\nu}. \quad (21)$$

### 2.1.2 SIDIS

Fig. 2 illustrates electron-proton SIDIS given by the expression

$$e^-(l) + p(P) \rightarrow e^-(l') + H(P_h) + X(P_X). \quad (22)$$

This process and its kinematics are the same as inclusive DIS (Section 2.1.1) with the exception of adding a final-state hadron. In the Breit frame defined in Section 2.1.1, the final-state hadron four-momentum is

$$P_h^\mu = \left( \frac{M_h^2 + P_{h\text{T}}^2}{\sqrt{2}z_{\text{N}}Q}, \frac{z_{\text{N}}Q}{\sqrt{2}}, \mathbf{P}_{h\text{T}} \right), \quad (23)$$

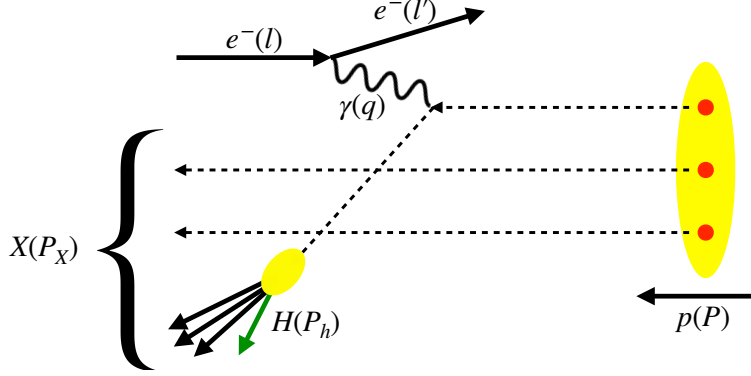


Figure 2: Illustration of the SIDIS process.

where  $\mathbf{P}_{hT}$  defines the direction of the x-axis.  $M_h$  is the mass of the final-state hadron. The parameter  $z_N$  is a ratio analogous to  $x_N$  defined as  $z_N = P_h^-/q^-$ . The parameter analogous to  $x_{Bj}$  is  $z_h = P \cdot P_h/P \cdot q$ . These are related by the expressions

$$z_N = \frac{x_N z_h}{2x_{Bj}} \left( 1 + \sqrt{1 - \frac{4x_{Bj}^2 M^2 (M_h^2 + P_{hT}^2)}{Q^4 z_h^2}} \right) \quad \text{and} \quad z_h = \frac{x_{Bj} z_N}{x_N} \left( 1 + \frac{x_N^2 M^2 (M_h^2 + P_{hT}^2)}{z_N^2 Q^4} \right). \quad (24)$$

In the case where the target and final-state hadron masses are neglected  $z_N = z_h$  and if only the final-state hadron mass is neglected  $z_N = x_N z_h/x_{Bj}$ .

It is also sometimes convenient to work in a frame where the target and final-state momenta are in opposite directions along the z-axis which I will call the hadron frame. In this frame the relevant four-momenta are

$$P^\mu = \left( \frac{Q}{\sqrt{2}x_N}, \frac{x_N M^2}{\sqrt{2}Q}, \mathbf{0}_T \right), \quad (25)$$

$$P_h^\mu = \left( \frac{M_h^2}{\sqrt{2}z_N Q}, \frac{z_N Q}{\sqrt{2}}, \mathbf{0}_T \right), \quad (26)$$

$$q^\mu = \left( -\frac{Q}{\sqrt{2}}, \frac{Q}{\sqrt{2}}, \mathbf{q}_T \right). \quad (27)$$

The expression for the SIDIS cross section is

$$4P_h^0 E' \frac{d\sigma_{\text{SIDIS}}}{d^3\mathbf{l}' d^3\mathbf{P}_h} = \frac{2\alpha_{\text{em}}^2}{(s - M^2) Q^4} L_{\mu\nu} W_{\text{SIDIS}}^{\mu\nu}, \quad (28)$$

where the hadronic tensor is defined as

$$W_{\text{SIDIS}}^{\mu\nu}(P, q, P_h) = \sum_X \langle P, S | j^\mu(0) | P_h, X \rangle \langle P_h, X | j^\nu(0) | P, S \rangle \delta^{(4)}(q + P - P_h - P_X). \quad (29)$$

The structure function decomposition of the hadronic tensor is similar to that for inclusive DIS,

$$\begin{aligned} W_{\text{SIDIS}}^{\mu\nu}(P, q, P_h) = & \left( -g^{\mu\nu} - \frac{q^\mu q^\nu}{Q^2} \right) F_1(x_{\text{Bj}}, z_h, \mathbf{P}_{h\text{T}}, Q^2) \\ & + \left( P^\mu + \frac{P \cdot q}{Q^2} q^\mu \right) \left( P^\nu + \frac{P \cdot q}{Q^2} q^\nu \right) \frac{F_2(x_{\text{Bj}}, z_h, \mathbf{P}_{h\text{T}}, Q^2)}{P \cdot q}. \end{aligned} \quad (30)$$

The structure functions can be obtained by contracting the hadronic tensor with the extraction tensors in Eq. (19).

Using the following change of variables:

$$\frac{d^3\mathbf{l}' d^3\mathbf{P}_h}{E' P_h^0} = \frac{dl'^+ dl'_T d\phi dP_h^+ d^2\mathbf{P}_{h\text{T}}}{l'^+ P_h^+} = \frac{(s - M^2) y}{2z_{\text{N}}} dx_{\text{N}} dy d\phi dz_{\text{N}} d^2\mathbf{P}_{h\text{T}}, \quad (31)$$

and integrating over  $\phi$ , the expression for the cross section becomes

$$\frac{d\sigma_{\text{SIDIS}}}{dx_{\text{N}} dy dz_{\text{N}} d^2\mathbf{P}_{h\text{T}}} = \frac{\pi\alpha_{\text{em}}^2 y}{2Q^4 z_{\text{N}}} L_{\mu\nu} W_{\text{SIDIS}}^{\mu\nu}. \quad (32)$$

## 2.2 Semi-inclusive $e^+/e^-$ annihilation kinematics

The  $e^+/e^-$  annihilation process is the generation of a virtual photon from the annihilation of an electron and positron where the photon then produces a quark/antiquark pair that form jets of hadrons. The momenta of the initial electron ( $l$ ) and positron ( $l'$ ) and either

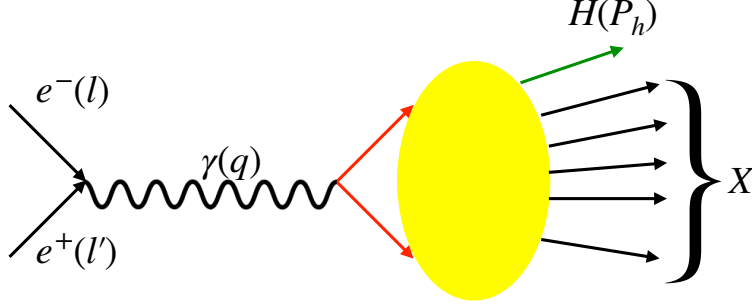


Figure 3: Illustration of the single hadron electron-positron annihilation process.

one final-state hadron ( $P_h$ ) or a pair of final-state hadrons ( $P_A$  and  $P_B$ ) are the measured quantities. The photon has momentum  $q = l + l'$  and the hard scale is  $Q^2 = q^2$ . The conventions used here are consistent with those found in [35].

### 2.2.1 Single hadron production

Fig. 3 illustrates single hadron production from electron-positron annihilation (SHSIA) given by the expression

$$e^-(l) + e^+(l') \rightarrow H(P_h) + X(P_X). \quad (33)$$

It is convenient to work in the center of mass frame with the final-state hadron momentum on the z-axis. If I neglect the hadron mass, the photon and hadron four-momenta are

$$q^\mu = \left( \frac{Q}{\sqrt{2}}, \frac{Q}{\sqrt{2}}, \mathbf{0}_T \right), \quad (34)$$

$$P_h^\mu = \left( \frac{z_h Q}{\sqrt{2}}, 0, \mathbf{0}_T \right), \quad (35)$$

where  $z_h = 2P_h \cdot q / Q^2$ .

The expression for the single hadron production cross section is

$$E_h \frac{d\sigma_{\text{SHSIA}}}{d^3\mathbf{P}_h} = \frac{\alpha_{\text{em}}^2}{Q^6} L_{\mu\nu} W_{\text{SHSIA}}^{\mu\nu} \quad (36)$$

where the hadronic tensor is defined as

$$W_{\text{SHSIA}}^{\mu\nu}(P_h, q) = 4\pi^3 \sum_X \langle 0 | j^\mu(0) | P_h, X, \text{out} \rangle \langle P_h, X, \text{out} | j^\nu(0) | 0 \rangle \delta^{(4)}(q - P_h - P_X). \quad (37)$$

In the unpolarized case, the structure function decomposition of the hadronic tensor is

$$W_{\text{SHSIA}}^{\mu\nu}(P_h, q) = \left( -g^{\mu\nu} + \frac{q^\mu q^\nu}{Q^2} \right) F_1(z_h, Q^2) + \left( P_h^\mu - \frac{P_h \cdot q}{Q^2} q^\mu \right) \left( P_h^\nu - \frac{P_h \cdot q}{Q^2} q^\nu \right) \frac{F_2(z_h, Q^2)}{P_h \cdot q}. \quad (38)$$

The structure functions can be obtained by contracting the hadronic tensor with extraction tensors

$$F_i(z_h, Q^2) = P_i^{\mu\nu} W_{\mu\nu}^{\text{SHSIA}}(P_h, q), \quad i = 1, 2, \quad (39)$$

where

$$P_1^{\mu\nu} \equiv -\frac{1}{2} g^{\mu\nu} - \frac{2}{z_h^2 Q^2} P_h^\mu P_h^\nu, \quad (40a)$$

$$P_2^{\mu\nu} \equiv \frac{1}{2} g^{\mu\nu} + \frac{6}{z_h^2 Q^2} P_h^\mu P_h^\nu. \quad (40b)$$

I can put the cross section in a more commonly used form using the following change of variables:

$$\frac{d^3 \mathbf{P}_h}{E_h} = \frac{dE_h d \cos \theta d\phi}{E_h} = \frac{1}{z_h} dz_h d \cos \theta d\phi, \quad (41)$$

where  $\theta$  and  $\phi$  are the polar and azimuthal angles of  $P_h$  in a center-of-mass frame where  $l$  is on the z-axis. Substituting this and integrating over  $\phi$  gives

$$\frac{d\sigma_{\text{SHSIA}}}{dz_h d \cos \theta} = \frac{2\pi \alpha_{\text{em}}^2}{z_h Q^6} L_{\mu\nu} W_{\text{SHSIA}}^{\mu\nu}. \quad (42)$$

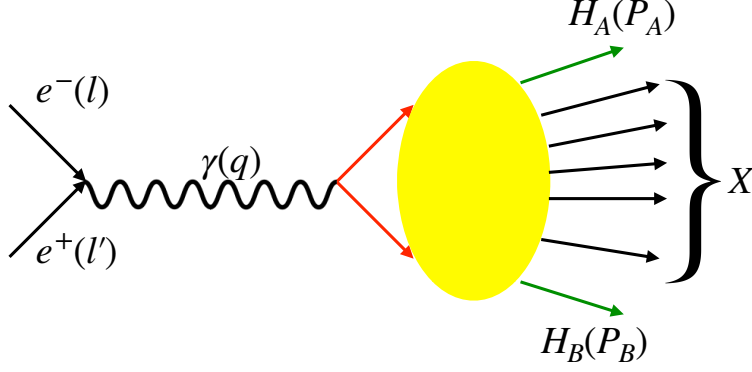


Figure 4: Illustration of the hadron pair electron-positron annihilation process.

### 2.2.2 Hadron pair production

Fig. 4 illustrates hadron pair production from electron-positron annihilation (HPSIA) given by the expression

$$e^-(l) + e^+(l') \rightarrow H_A(P_A) + H_B(P_B) + X(P_X). \quad (43)$$

It is convenient to work in a frame (called the hadron frame) with the final-state hadron momenta back-to-back on the  $z$ -axis. If I neglect the hadron masses, the photon and hadron four-momenta are

$$q^\mu = \left( \sqrt{\frac{Q^2 + q_T^2}{2}}, \sqrt{\frac{Q^2 + q_T^2}{2}}, \mathbf{q}_T \right), \quad (44)$$

$$P_A^\mu = \left( z_A \sqrt{\frac{Q^2 + q_T^2}{2}}, 0, \mathbf{0}_T \right), \quad (45)$$

$$P_B^\mu = \left( 0, z_B \sqrt{\frac{Q^2 + q_T^2}{2}}, \mathbf{0}_T \right), \quad (46)$$

where

$$z_A = \frac{P_A \cdot P_B}{q \cdot P_B}, \quad z_B = \frac{P_A \cdot P_B}{q \cdot P_A}. \quad (47)$$

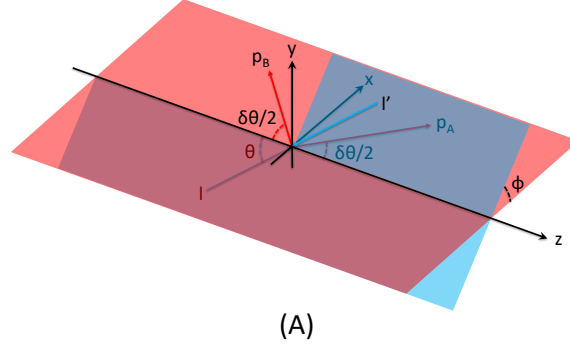


Figure 5: Diagram taken from [36]. The photon frame. The  $x$  and  $z$  axes have been aligned with the spatial components of  $X^\mu$  and  $Z^\mu$  from Eq. (54). The blue plane is the  $e^+e^-$  plane.

The transverse momentum of the photon  $\mathbf{q}_T$  is along the negative x-axis and

$$q_T^2 = \frac{2 P_A \cdot q P_B \cdot q}{P_A \cdot P_B} - Q^2. \quad (48)$$

The transverse momentum has an absolute kinematical upper bound:

$$q_T^{\text{Max}^2} \leq \frac{Q^2(1 - z_A)(1 - z_B)}{1 - (1 - z_A)(1 - z_B)}. \quad (49)$$

By boosting along the x-axis until  $\mathbf{q}_T$  equals zero, I define another convenient frame (called the photon frame and illustrated in Fig. 5) based on the center-of-mass of the system.

The momenta in this frame given in Minkowski coordinates are

$$q^\mu = (Q, 0, 0, 0), \quad (50)$$

$$P_A^\mu = E_A (1, \mathbf{n}_A) \quad (51)$$

$$P_B^\mu = E_B (1, \mathbf{n}_B), \quad (52)$$

where  $\mathbf{n}_A$  and  $\mathbf{n}_B$  are spatial unit vectors in the direction of  $\mathbf{P}_A$  and  $\mathbf{P}_B$ . The hadron energies

are given by

$$E_i = \frac{z_i}{2Q} (Q^2 + q_T^2), \quad i = A, B. \quad (53)$$

Unit vectors in the direction of the x and z axes in Fig. 5 are built from the vectors  $\mathbf{n}_A$  and  $\mathbf{n}_B$  as follows:

$$Z_\gamma^\mu = \frac{(0, \mathbf{n}_{A,\gamma} - \mathbf{n}_{B,\gamma})}{|\mathbf{n}_{A,\gamma} - \mathbf{n}_{B,\gamma}|}, \quad X_\gamma^\mu = \frac{(0, \mathbf{n}_{A,\gamma} + \mathbf{n}_{B,\gamma})}{|\mathbf{n}_{A,\gamma} + \mathbf{n}_{B,\gamma}|}. \quad (54)$$

In this frame the z-axis bisects the angle between  $\mathbf{P}_A$  and  $-\mathbf{P}_B$  and the x-axis is orthogonal in the plane formed by  $\mathbf{P}_A$  and  $\mathbf{P}_B$ .

The expression for the hadron pair production cross section is

$$E_A E_B \frac{d\sigma_{AB}}{d^3\mathbf{P}_A d^3\mathbf{P}_B} = \frac{\alpha_{\text{em}}^2}{16\pi^3 Q^6} L_{\mu\nu} W_{\text{HPSIA}}^{\mu\nu}, \quad (55)$$

where the hadronic tensor is defined as

$$W_{\text{HPSIA}}^{\mu\nu} \equiv 4\pi^3 \sum_X \langle 0 | j^\mu(0) | P_A, P_B, X \rangle \langle P_A, P_B, X | j^\nu(0) | 0 \rangle \delta^{(4)}(q - P_A - P_B - P_X). \quad (56)$$

In the unpolarized case, the structure function decomposition of the hadronic tensor is

$$W_{\text{HPSIA}}^{\mu\nu}(q, P_A, P_B) = \left( -g^{\mu\nu} + \frac{q^\mu q^\nu}{Q^2} - Z^\mu Z^\nu \right) W_T(z_A, z_B, Q^2) + Z^\mu Z^\nu W_L(z_A, z_B, Q^2). \quad (57)$$

where  $W_T$  and  $W_L$  are the transverse and longitudinal structure functions and  $Z$  is the unit vector in Eq. (54). The structure functions can be obtained by contracting the hadronic tensor with extraction tensors

$$W_i(z_A, z_B, Q^2) = P_i^{\mu\nu} W_{\mu\nu}^{\text{HPSIA}}(q, P_A, P_B), \quad i = T, L, \quad (58)$$

where

$$P_T^{\mu\nu} \equiv \frac{1}{3} (-g^{\mu\nu} - Z^\mu Z^\nu + X^\mu X^\nu), \quad (59a)$$

$$P_L^{\mu\nu} \equiv Z^\mu Z^\nu, \quad (59b)$$

where  $X$  and  $Z$  are the unit vectors in Eq. (54).

I can put the cross section in a more commonly used form using a change of variables. This is easiest in a center of mass frame where  $p_B$  is on the z-axis. In this frame, the hadron momenta in terms of  $Q$ ,  $q_T$ ,  $z_A$ , and  $z_B$  (in Cartesian coordinates) are:

$$P_A = \left( \frac{z_A}{2Q} (Q^2 + q_T^2), -z_A \mathbf{q}_T, -\frac{z_A}{2Q} (Q^2 - q_T^2) \right) \quad (60)$$

$$P_B = \left( \frac{z_B}{2Q} (Q^2 + q_T^2), \mathbf{0}_T, \frac{z_B}{2Q} (Q^2 + q_T^2) \right). \quad (61)$$

and the lepton momentum  $l$  is:

$$l = \left( \frac{Q}{2}, \frac{Q}{2} \sin \theta \cos \phi, \frac{Q}{2} \sin \theta \sin \phi, \frac{Q}{2} \cos \theta \right). \quad (62)$$

The change of variables is then

$$\frac{d^3 \mathbf{P}_A d^3 \mathbf{P}_B}{E_A E_B} = \frac{E_B d^3 \mathbf{P}_A dE_B d \cos \theta d\phi d\phi_A}{E_A} = \frac{q_T (Q^2 + q_T^2)^2 z_A z_B}{4Q^2} dz_A dz_B dq_T d\phi_A d \cos \theta d\phi. \quad (63)$$

Substituting this and integrating over  $\phi_A$  gives

$$\frac{d\sigma_{\text{HPSIA}}}{dz_A dz_B dq_T d \cos \theta d\phi} = \frac{\alpha_{\text{em}}^2 z_A z_B (Q^2 + q_T^2)^2 q_T}{32\pi^2 Q^8} L_{\mu\nu} W_{\text{HPSIA}}^{\mu\nu}. \quad (64)$$

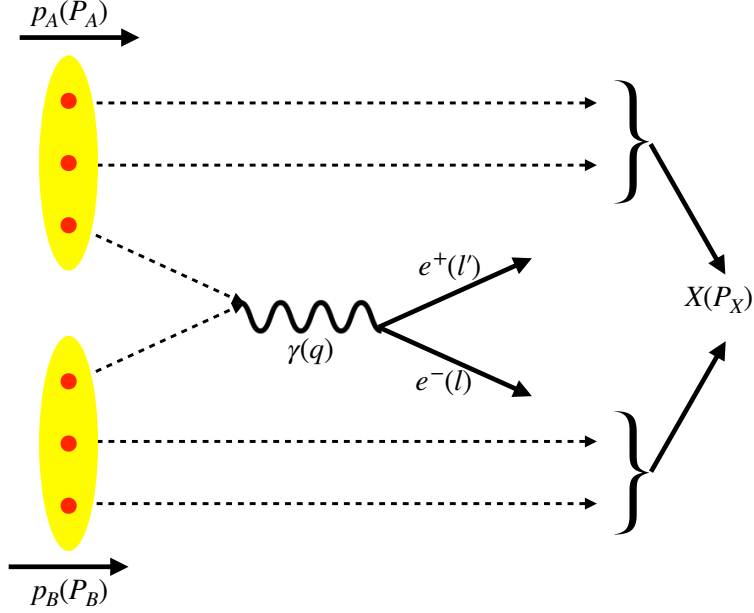


Figure 6: Illustration of dilepton production from the DY process.

### 2.3 Drell-Yan kinematics

Drell-Yan scattering is between two hadrons. Specifically, a quark from one hadron and an anti-quark from the other annihilate to produce a virtual photon. The photon then produces a final-state lepton pair and the remnants of the two hadrons produce jets of final-state hadrons. The momenta of the two initial hadrons ( $P_A$  and  $P_B$ ) and the lepton pair ( $l$  and  $l'$ ) are measured. The photon has momentum  $q = l + l'$  and the hard scale is  $Q^2 = q^2$  also called the invariant mass of the lepton pair. Conventions used here are consistent with those in [35, 37].

Fig. 6 illustrates dilepton production from Drell-Yan hadron-hadron scattering given by the expression

$$H_A(P_A) + H_B(P_B) \rightarrow e^-(l) + e^+(l') + X(P_X). \quad (65)$$

In a center of mass frame where the two hadron momenta are back-to-back on the z-axis,

the momenta when neglecting masses are given by

$$P_A^\mu = \left( \sqrt{\frac{s}{2}}, 0, \mathbf{0}_T \right), \quad (66)$$

$$P_B^\mu = \left( 0, \sqrt{\frac{s}{2}}, \mathbf{0}_T \right), \quad (67)$$

$$q^\mu = \left( x_A \sqrt{\frac{s}{2} \left( 1 + \frac{q_T^2}{Q^2} \right)}, x_B \sqrt{\frac{s}{2} \left( 1 + \frac{q_T^2}{Q^2} \right)}, \mathbf{q}_T \right), \quad (68)$$

where  $s = (P_A + P_B)^2$ ,  $x_A = Qe^y/\sqrt{s}$ , and  $x_B = Qe^{-y}/\sqrt{s}$ . The rapidity of the lepton pair  $y$  is defined as

$$y = \frac{1}{2} \ln \frac{q^+}{q^-}. \quad (69)$$

The expression for the single hadron production cross section is

$$EE' \frac{d\sigma_{\text{DY}}}{d^3\mathbf{l}d^3\mathbf{l}'} = \frac{\alpha_{\text{em}}^2}{(2\pi)^4 s^2 Q^2} L_{\mu\nu} W_{\text{DY}}^{\mu\nu} \quad (70)$$

where the hadronic tensor is defined as

$$W_{\text{DY}}^{\mu\nu}(P_A, P_B, q) = s \int d^4z e^{iq \cdot z} \langle P_A, P_B | j^\mu(z) j^\nu(0) | P_A, P_B \rangle. \quad (71)$$

In the unpolarized case, the structure function decomposition of the hadronic tensor is

$$\begin{aligned} W_{\text{DY}}^{\mu\nu}(P_A, P_B, q) &= \left( g^{\mu\nu} - \frac{q^\mu q^\nu}{Q^2} \right) W_1(x_A, x_B, Q^2) \\ &+ \left( P_+^\mu - \frac{P_+ \cdot q}{Q^2} q^\mu \right) \left( P_+^\nu - \frac{P_+ \cdot q}{Q^2} q^\nu \right) \frac{W_2(x_A, x_B, Q^2)}{s}, \end{aligned} \quad (72)$$

where  $P_+ = P_A + P_B$ . The structure functions can be obtained by contracting the hadronic tensor with extraction tensors

$$W_i(x_A, x_B, Q^2) = P_i^{\mu\nu} W_{\mu\nu}^{\text{DY}}(P_A, P_B, q), \quad i = 1, 2, \quad (73)$$

where

$$P_1^{\mu\nu} \equiv -\frac{1}{2}g^{\mu\nu} - \frac{2}{z_h^2 Q^2} P_h^\mu P_h^\nu, \quad (74a)$$

$$P_2^{\mu\nu} \equiv \frac{1}{2}g^{\mu\nu} + \frac{6}{z_h^2 Q^2} P_h^\mu P_h^\nu. \quad (74b)$$

I can put the cross section in a more commonly used form using the following change of variables:

$$\frac{d^3\mathbf{l}}{E} \frac{d^3\mathbf{l}'}{E'} = \frac{E}{E'} dE d\cos\theta d\phi d^3\mathbf{q} = dq_0 dq_z d^2\mathbf{q}_T d\cos\theta d\phi = \frac{s}{2} \left(1 + \frac{q_T^2}{Q^2}\right) dx_A dx_B d^2\mathbf{q}_T d\cos\theta d\phi. \quad (75)$$

Substituting this and integrating over  $\phi$  gives

$$\frac{d\sigma_{DY}}{dx_A dx_B d^2\mathbf{q}_T d\cos\theta} = \frac{\alpha_{\text{em}}^2}{16\pi^3 s Q^4} \left(1 + \frac{q_T^2}{Q^2}\right) L_{\mu\nu} W_{DY}^{\mu\nu}. \quad (76)$$

## CHAPTER 3

### COLLINEAR FACTORIZATION IN INCLUSIVE DIS

This chapter will review in detail the steps necessary to obtain the collinear factorized expression for the inclusive DIS cross section. These steps and their justification are discussed in more detail in [35]. Fig. 7 shows the leading (in  $m/Q$ ) region graphical topology that contributes at zero order in  $\alpha_s$  to the inclusive DIS hadronic tensor. The general form of the contribution to the hadronic tensor from this figure can be expressed as

$$W^{\mu\nu}(P, q) = \sum_j \frac{e_j^2}{4\pi} \int \frac{d^4k}{(2\pi)^4} \text{Tr} \left[ H^\mu(k, k') U(k') H^{\nu\dagger}(k, k') L(P, k) \right], \quad (77)$$

where the sum is over all quark and antiquark flavors and  $e_j$  is the fraction of charge carried by quark flavor  $j$ .

In the hard scattering subgraphs,  $H^\mu(k, k')$  and  $H^{\nu\dagger}(k, k')$ , all internal lines are off-shell by  $O(Q^2)$ . The lower subgraph,  $L(P, k)$ , represents the target and the hadronization of its remnant while the upper subgraph,  $U(k')$ , is the hadron jet generated from the struck quark. The internal lines in these subgraphs are off-shell by  $O(m^2)$ . Recall  $m$  is a generic small scale typically on the order of  $\Lambda_{QCD}$ . The parton lines connecting the subgraphs ( $k$  and  $k'$ ) are also off-shell by  $O(m^2)$ . Note at higher orders of  $\alpha_s$  in the hard parts, there could be multiple upper subgraphs, but for the purposes of illustrating the steps of factorization, I will consider the single jet case.

The goal of factorization is to separate this graph into two parts, one containing  $L(P, k)$  with non-perturbative contributions and the second encompassing the remainder of the diagram containing only partonic interactions. Assuming  $k$  is collinear to the target momentum  $P$ , the power counting is

$$k \sim \left( O(Q), O\left(\frac{m^2}{Q}\right), O(\mathbf{m}_T) \right), \quad (78)$$

where  $O(\mathbf{m}_T)$  means both components of the transverse momentum are  $O(m)$ . I can exploit

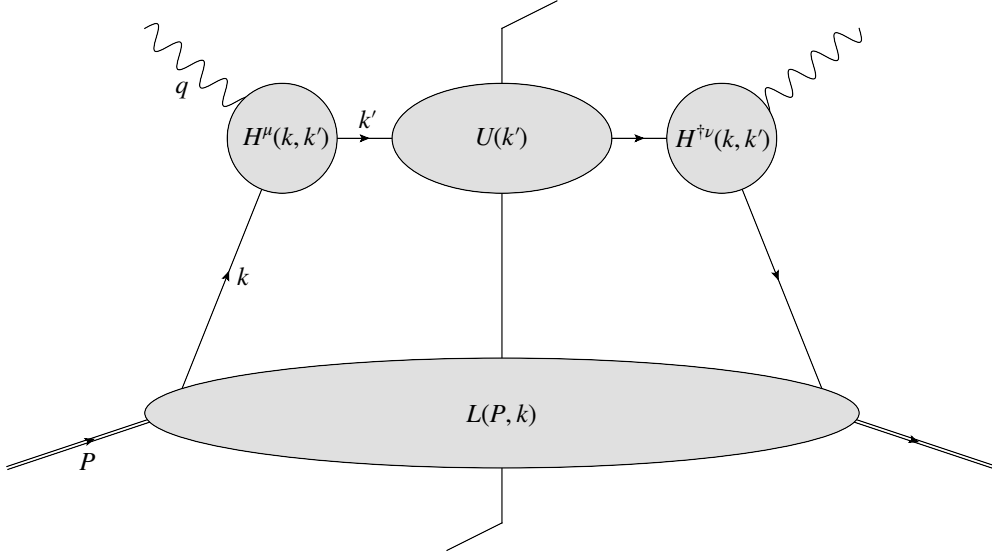


Figure 7: Basic handbag diagram for inclusive DIS.

this to justify the set of standard approximations necessary to achieve factorization.

In the hard subgraphs, the relevant Laurentz invariants are

$$\begin{aligned}
 k^2 &= O(m^2) \sim 0, \\
 k'^2 &= O(m^2) \sim 0, \\
 k \cdot k' &= k \cdot (k + q) = k^+ q^- + O(m^2) \sim k^+ q^-.
 \end{aligned} \tag{79}$$

I can make the approximations in Eq. (79) because the internal lines in the hard parts are off-shell by  $O(Q^2)$ . Thus I can replace  $k$  and  $k'$  in the hard parts with the following “hatted” variables:

$$k \rightarrow \hat{k} = (\xi P^+, 0, \mathbf{0}_T), \tag{80}$$

$$k' \rightarrow \hat{k}' = \hat{k} + q = (0, q^-, \mathbf{0}_T). \tag{81}$$

with

$$\hat{k}^2 = \hat{k}'^2 = 0. \quad (82)$$

Therefore the replacement of  $H^\mu(k, k')$  with  $H^\mu(\hat{k}, \hat{k}')$  is a good approximation up to  $O(m^2/Q^2)$  corrections. In the specific case of Fig. 7, conservation of momentum gives  $\xi = x_N$  and in the case where  $Q \gg M$ ,  $x_N \rightarrow x_{\text{Bj}}$ . Note that the use of  $x_N \rightarrow x_{\text{Bj}}$  is not necessary to achieve factorization, but it is conventional to use  $x_{\text{Bj}}$ . This will be discussed in more detail in Chapter 5. With the value of  $\xi$  fixed like this  $H^\mu(\hat{k}, \hat{k}')$  is actually just a function of  $Q^2$ .

In the lower subgraph, the internal lines are off-shell by only  $O(m^2)$  and with the replacement of  $k^+ \rightarrow x_{\text{Bj}}P^+ + O(m^2/Q)$ ,

$$\begin{aligned} k^2 &= 2k^+k^- - k_{\text{T}}^2 \\ &= \underbrace{2(x_{\text{Bj}}P^+)k^- - k_{\text{T}}^2}_{O(m^2)} + O(m^4/Q^2), \end{aligned} \quad (83)$$

$$\begin{aligned} (P+k)^2 &= M^2 + 2P^+k^- + 2P^-k^+ + 2k^+k^- - k_{\text{T}}^2 \\ &= \underbrace{M^2 + 2P^+k^- + 2P^-(x_{\text{Bj}}P^+) + 2(x_{\text{Bj}}P^+)k^- - k_{\text{T}}^2}_{O(m^2)} + O(m^4/Q^2). \end{aligned} \quad (84)$$

Thus in order to avoid introducing unsuppressed errors, it is necessary to keep the exact values of the small components of  $k$  ( $k^-$  and  $k_{\text{T}}$ ). Therefore  $k$  in the lower subgraph is approximated with another momentum four-vector  $\tilde{k}^\mu$ , defined in the Breit frame as

$$\tilde{k} \equiv (x_{\text{Bj}}P^+, k^-, \mathbf{k}_{\text{T}}), \quad (85)$$

so that the replacement  $L(k, P) \rightarrow L(\tilde{k}, P)$  is a good approximation up to  $O(m^2/Q^2)$  corrections.

The internal lines of  $U(k')$  are also off-shell by  $O(m^2)$ , while the power counting for  $k'$  is

$$k' \sim (O(m^2/Q), O(Q), O(\mathbf{m}_{\text{T}})). \quad (86)$$

A Lorentz transformation to a frame labeled by “\*”, where the outgoing transverse momentum vanishes,  $k_{\text{T}}'^* = 0$  reveals the appropriate approximation for the upper subgraph. In terms of the Breit frame variables, one has

$$k'^* = \left( k^+ + q^+ - \frac{k_{\text{T}}^2}{2(q^- + k^-)}, q^- + k^-, \mathbf{0}_{\text{T}} \right), \quad (87)$$

so that the outgoing parton’s virtuality is

$$\begin{aligned} k'^{*2} &= 2(k^+ + q^+)(k^- + q^-) - k_{\text{T}}^2 \\ &\sim 2(k^+ + q^+)q^- - k_{\text{T}}^2 + O\left(\frac{m^3}{Q}\right). \end{aligned} \quad (88)$$

Since  $q^-$  is  $O(Q)$ , the smallest component of  $k$ , namely  $k^-$ , can be neglected in  $U(k')$ . Therefore, I define the approximate outgoing momentum four-vector

$$k' \rightarrow \tilde{k}' \equiv (l^+, q^-, \mathbf{0}_{\text{T}}), \quad (89)$$

where  $l^+ \equiv k^+ - x_{\text{Bj}}P^+ + k_{\text{T}}^2/(2q^-)$ . Changing the integration variables from  $k^+$  to  $l^+$  in Eq. (77) gives

$$W^{\mu\nu}(P, q) = \sum_j \frac{e_j^2}{4\pi} \int \frac{dl^+ dk^- d^2\mathbf{k}_{\text{T}}}{(2\pi)^4} \text{Tr} \left[ H^\mu(Q^2) U(l^+) H^{\dagger\nu}(Q^2) L(\tilde{k}', P) \right] + O\left(\frac{m^2}{Q^2}\right) W^{\mu\nu}. \quad (90)$$

With these approximations, the integrations can be moved to make separate lower and upper subgraph factors:

$$\begin{aligned}
& W^{\mu\nu}(P, q) \\
&= \sum_j \frac{e_j^2}{4\pi} \text{Tr} \left[ H^\mu(Q^2) \left( \int \frac{dl^+}{2\pi} U(l^+) \right) H^{\nu\dagger}(Q^2) \left( \int \frac{dk^- d^2\mathbf{k}_T}{(2\pi)^3} L(\tilde{k}, P) \right) \right] + O\left(\frac{m^2}{Q^2}\right) W^{\mu\nu}.
\end{aligned} \tag{91}$$

To complete the factorization, the upper and lower subgraphs are decomposed in a basis of Dirac matrices,

$$U(l^+) = \gamma_\mu \Delta^\mu(l^+) + \Delta_S(l^+) + \gamma_5 \Delta_P(l^+) + \gamma_5 \gamma_\mu \Delta_A^\mu(l^+) + \sigma_{\mu\nu} \Delta_T^{\mu\nu}(l^+), \tag{92a}$$

$$L(\tilde{k}, P) = \gamma_\mu \Phi^\mu(\tilde{k}, P) + \Phi_S(\tilde{k}, P) + \gamma_5 \Phi_P(\tilde{k}, P) + \gamma_5 \gamma_\mu \Phi_A^\mu(\tilde{k}, P) + \sigma_{\mu\nu} \Phi_T^{\mu\nu}(\tilde{k}, P), \tag{92b}$$

in terms of vector, scalar, pseudoscalar, axial vector and tensor functions. If I focus only on spin- and azimuthally-independent cross sections, only the first term in Eq. (92a) and the first term in Eq. (92b) need be kept. To leading power, only the “−” component of  $\Delta^\mu$  and only the “+” component of  $\Phi^\mu$  contribute, so that the operators can be expanded as

$$\begin{aligned}
U(l^+) &= \gamma^+ \Delta^-(l^+) + O\left(\frac{m^2}{Q^2}\right) U + (\text{spin dep.}) \\
&= \frac{\not{k}'}{4q^-} \text{Tr} [\gamma^- U(l^+)] + O\left(\frac{m^2}{Q^2}\right) U + (\text{spin dep.}),
\end{aligned} \tag{93a}$$

$$\begin{aligned}
L(\tilde{k}, P) &= \gamma^- \Phi^+(\tilde{k}, P) + O\left(\frac{m^2}{Q^2}\right) L + (\text{spin dep.}) \\
&= \frac{\not{k}}{4x_N P^+} \text{Tr} [\gamma^+ L(\tilde{k}, P)] + O\left(\frac{m^2}{Q^2}\right) L + (\text{spin dep.}),
\end{aligned} \tag{93b}$$

where the spin-dependent terms are not written explicitly. Using Eqs. (93), the spin-averaged

hadronic tensor is then

$$\begin{aligned}
W^{\mu\nu}(P, q) &= \sum_j \frac{e_j^2}{4Q^2} \text{Tr} \left[ H^\mu(Q^2) \not{k}' H^{\dagger\nu}(Q^2) \not{k} \right] \left( \int \frac{dl^+}{2\pi} \text{Tr} \left[ \frac{\gamma^-}{2} U(l^+) \right] \right) \\
&\quad \times \left( \int \frac{dk^- d^2\mathbf{k}_T}{(2\pi)^3} \text{Tr} \left[ \frac{\gamma^+}{2} L(\tilde{k}, P) \right] \right) + O\left(\frac{m^2}{Q^2}\right) W^{\mu\nu}. \tag{94}
\end{aligned}$$

Finally, the integration contour for  $l^+$  is deformed away from the  $k'$  pole until  $l^+q^-$  is  $O(Q^2)$ . To lowest order in  $\alpha_s$ ,  $U$  can then be replaced by the massless, on-shell cut diagram, so the hadronic tensor in Eq. (94) becomes

$$\begin{aligned}
W^{\mu\nu}(P, q) &= \sum_j \frac{e_j^2}{4Q^2} \underbrace{\text{Tr} \left[ H^\mu(Q^2) \not{k}' H^{\dagger\nu}(Q^2) \not{k} \right]}_{\mathcal{H}^{\mu\nu}(Q^2)} \underbrace{\left( \int \frac{dk^- d^2\mathbf{k}_T}{(2\pi)^4} \text{Tr} \left[ \frac{\gamma^+}{2} L(\tilde{k}, P) \right] \right)}_{f(x_{Bj})} \\
&\quad + O\left(\frac{m^2}{Q^2}\right) W^{\mu\nu}. \tag{95}
\end{aligned}$$

Thus the hadronic tensor has been factorized into the product of a hard scattering factor  $\mathcal{H}^{\mu\nu}(Q^2)$  containing the short distance [ $O(Q^2)$ ] physics and a parton distribution  $f(x_{Bj})$  containing large distance [ $O(m^2)$ ] physics associated with the target hadron.

The result in Eq. (95) is specific to the diagram in Fig. 7 which is the only contribution when the hard factor is lowest order in  $\alpha_s$ . At higher orders, additional diagrams with more partons entering and/or leaving the hard factors also contribute. In these cases the parton momentum fraction  $\xi$  is not fixed at  $x_{Bj}$ . Instead the factorization results in a convolution. The general expression for the factorized hadronic tensor is

$$\begin{aligned}
W^{\mu\nu}(P, q) &= \sum_{f/f'} \int_{x_{Bj}}^1 \frac{d\xi}{\xi} \widehat{W}_{f/f'}^{\mu\nu}(\hat{k}, q) f_{f'/p}(\xi) + O(m^2/Q^2), \\
&= \sum_{f/f'} \widehat{W}_{f/f'}^{\mu\nu} \otimes f_{f'/p} + O(m^2/Q^2), \tag{96}
\end{aligned}$$

where  $\widehat{W}_{f/f'}^{\mu\nu}$  is a tensor similar to the hadronic tensor but calculated for only the hard part.

The indices  $f$ ,  $f'$ , and  $p$  specify the outgoing parton, incoming parton, and the target hadron respectively. Similar to Eq. (17), this partonic tensor can be expressed in terms of partonic structure functions

$$\begin{aligned} \widehat{W}_{f/f'}^{\mu\nu}(\hat{k}, q) &= \left(-g^{\mu\nu} + \frac{q^\mu q^\nu}{q^2}\right) \widehat{\mathcal{F}}_{1,f/f'}(x_{\text{Bj}}/\xi, Q^2) \\ &+ \left(\hat{k}^\mu - \frac{\hat{k} \cdot q}{q^2} q^\mu\right) \left(\hat{k}^\nu - \frac{\hat{k} \cdot q}{q^2} q^\nu\right) \frac{\widehat{\mathcal{F}}_{2,f/f'}(x_{\text{Bj}}/\xi, Q^2)}{\hat{k} \cdot q}. \end{aligned} \quad (97)$$

The factorized expressions for the structure functions are then

$$\begin{aligned} F_i(x_{\text{Bj}}, Q^2) &= \sum_{f,f'} \int_{x_{\text{Bj}}}^1 \frac{d\xi}{\xi} \widehat{\mathcal{F}}_{i,f/f'}(x_{\text{Bj}}/\xi, Q^2) f_{f'/p}(\xi) + O(m^2/Q^2) \\ &= \sum_{f,f'} \widehat{\mathcal{F}}_{i,f/f'} \otimes f_{f'/p} + O(m^2/Q^2). \end{aligned} \quad (98)$$

## CHAPTER 4

### EXPLORING FACTORIZATION USING A SIMPLE FIELD THEORY

One method for exploring factorization at moderate energies is by using a simple field theory. This is based on the observation that the approximations associated with factorization are not unique to QCD but instead can be applied to any renormalizable quantum field theory. By using a simple field theory where the observables can be calculated without approximations, the relative size of the errors arising from collinear factorization can be explored quantitatively. In this chapter, I demonstrate this using a field theory where a quark couples to a scalar “diquark” to form a “nucleon.” This is used to stress test the standard collinear parton model kinematical approximations.

I will argue, on the basis of the scalar diquark theory, that target masses, quark masses, quark transverse momentum, and quark virtuality are all likely to have similar quantitative importance at momentum scales of order a few GeV. Moreover, the analysis will allow proposal of a factorization-based notion of purely kinematical TMCs. For the lowest  $Q$  and largest  $x_{Bj}$  that typically define the boundary of the DIS region, it is found that corrections to a collinear picture are not negligible, and new factorization theorems, with correlation functions that depend on multiple components of parton momentum, may be necessary. Finally, this chapter will illustrate the general usefulness of the scalar diquark theory (or similar models) as a testing ground for the approximations in a factorization derivation. A factorization derivation deals, in essence, directly with a power series expansion of the cross section in  $m/Q$ ; a factorization theorem is a characterization of the leading power. Factorization is therefore the appropriate context for characterizing the size and general behavior of power corrections.

This chapter is organized as follows. In Sec. 4.1 I define the scalar diquark theory and discuss its analogy with the pertinent features of QCD. the full calculation with exact kinematics is presented in Sec. 4.2. The computation includes all diagrams, to lowest order in the coupling, that are necessary to maintain electromagnetic gauge invariance. I derive non-

factorized expressions for the contributions to the  $F_1$  and  $F_2$  structure functions from the “handbag” topology and  $1/Q$ -suppressed “cat’s ears” diagrams. The approximated calculation using the collinear factorization described in Chapter 3 is given in Sec. 4.3. The results are found to be identical to those of the exact calculation in the  $m/Q \rightarrow \infty$  limit, but as  $Q$  is lowered one is able to study effects from nonvanishing  $m/Q$  directly. In Sec. 4.4 I study these differences numerically, with the goal of analyzing the relative importance of different types of power corrections at moderate  $Q$ , and identifying the regions of kinematics where the collinearly factorized results may provide good approximations to the exact structure functions. Much of the work in this chapter was originally published in [38].

## 4.1 DIS in a simple model

### 4.1.1 Definition

I’ll begin by describing the field theory used as a proxy for QCD to highlight the salient aspects of factorization approximations at moderate values of  $Q$ . The results mainly concern the kinematics of the process, and complications from the non-Abelian nature of the full QCD theory do not directly affect the general conclusions. The simplified theory is still sufficiently nontrivial that the usual hurdles to deriving factorization in a renormalizable quantum field theory are present.

The theory describes the interaction between a spin-1/2 “nucleon” with mass  $M$  represented by the field  $\Psi_N$ , a spin-1/2 “quark” field  $\psi_q$  with mass  $m_q$ , and a scalar “diquark” state  $\phi$  with mass  $m_s$  that does not couple to the photon but remains a spectator to the hard scattering from the quark. The interaction Lagrangian density for this theory is given by a Yukawa-like interaction,

$$\mathcal{L}_{\text{int}} = -\lambda \bar{\Psi}_N \psi_q \phi + \text{H.c.}, \quad (99)$$

where the coupling  $\lambda$  gives the strength of the nucleon–quark–diquark interaction. In this

theory, the electron couples to quarks via electroweak gauge bosons as in the standard model. Furthermore, the theory is renormalizable, and the basic derivation of factorization theorems apply equally well to scattering processes here as to processes in QCD, where non-Abelian gauge invariance leads to complications that make factorization derivations more involved. In practice, factorization means that  $O(Q)$  physics factorizes from effects sensitive to intrinsic mass scales. The simplified theory is ideal for stress-testing factorization techniques generally before applying them to the more challenging environment of a non-Abelian gauge theory such as QCD.

#### 4.1.2 Analogy with QCD

The model described above is useful only to the extent that it highlights important aspects of actual QCD interactions. This is not a trivial point, since the handbag topology, while a useful starting point, does not strictly capture the true nature of QCD in DIS; a more accurate picture is probably closer to Monte Carlo event generators. Namely, partons generate showers of radiation both before and after the collision, and an arrangement of final state partons undergoes nonperturbative interactions to form a complex array of observable hadrons. This is illustrated in Fig. 8(a). This diagram emphasizes the physical picture of DIS: a sea of parton fluctuations involving quarks, antiquarks and gluons populates the rapidity interval between the incoming hadron and struck quark rapidities, with the partons interacting nonperturbatively to produce the final state hadrons. [Final state gluons are not shown explicitly in Fig. 8(a).]

The factorization theorem for inclusive scattering states, in part, that the sum of such diagrams may be approximated by the handbag topology of Fig. 8(b) in the limit of large  $Q$ . The diagram in Fig. 8(b) belongs to the leading region for inclusive DIS. Finally, a factorization formula emerges once approximations are applied to the active parton momentum, above and below the horizontal line in Fig. 8(c) separating the hard and soft parts of the diagram (see Ref. [35] for more details).

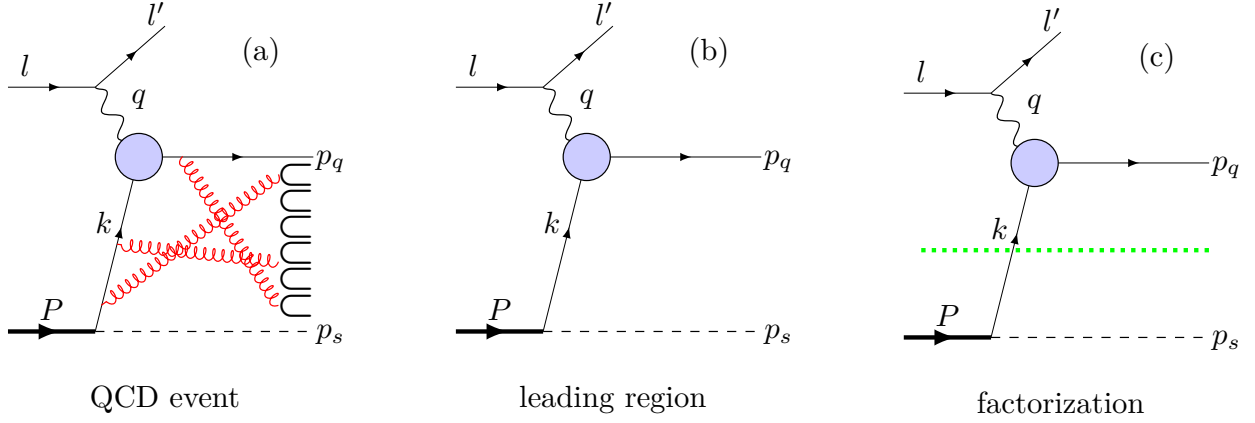


Figure 8: Figure taken from [38]. The sequence of approximations leading to the canonical parton model picture: (a) A physical picture of the complete QCD event. The symbols  $\subset$  represent the final state hadronization process. (b) The leading-power topological region contributing to the inclusive cross section. (c) The kinematical approximation (represented by the green dotted horizontal line) that produces the parton model cross section. The line is an instruction to replace the parton momentum by its approximated values (see Sec. 4.3). The momentum labels are discussed in the text.

The replacements in Fig. 8, from (a) to (b) and then (b) to (c), are only valid after integration over final states that results in a cascade of cancellations of non-factorizing effects. The approximations therefore rely on the cross section being fully inclusive. Any map from exact underlying quark and gluon degrees of freedom to the handbag picture is unavoidably indirect. Nevertheless, for the factorization theorem to hold, it is a *necessary* condition that the approximations on parton momentum represented by the horizontal line in Fig. 8(c) be at least roughly accurate. Thus, the transition from (b) to (c) will be the focus of this chapter. The main effect of that approximation is simply to alter the kinematics of the handbag diagram. I stress that such approximations are at the core of QCD factorization theorems which can also be studied in the context of the quark-diquark field theory. Those approximations were reviewed in Chapter 3.

In the simple toy field theory, the magnitude of the factorization error is fixed by the sizes of  $m_q$  and  $m_s$  relative to  $Q$ . The same will be true in QCD, for the analogous quantities. These parameters determine the size of the small components of parton four-momentum related to  $k^2$  and  $k_T$ . Other aspects of the quark-diquark theory, such as the dominant  $k_T$  power-law of correlation functions at large  $k_T$ , are also the same in QCD. The main difference between QCD and the toy theory is that, while the values of  $m_q$  and  $m_s$  are exactly fixed by the Lagrangian (and by restriction to the lowest-order graph) in the diquark theory, in QCD the effective parton and spectator masses generally have a spectrum of values that depend on  $x_{Bj}$ ,  $k_T$  and  $Q$  and intrinsic properties of the nucleon wave function. The kinematically allowed phase space grows with decreasing  $x_{Bj}$  and increasing  $Q$ , accommodating more of the soft radiation sketched in Fig. 8(a). Thus, the scales analogous to  $m_q$  and  $m_s$  will generally acquire nontrivial  $x_{Bj}$  and  $Q$  dependence in QCD.

In both theories, however,  $|k^2|$  and  $k_T^2$  need to be small relative to  $Q^2$  to give the  $m/Q$  suppression of neglected terms that is necessary for the factorization theorem in Eq. (98) to hold. If  $m_q$  and  $m_s$  are fixed to reasonable values for a given range of kinematics, and if the integration over  $k_T$  is dominated by  $k_T \ll Q$ , then one can verify directly that the parton

model approximations are good for the quark-diquark theory. Showing this directly lends some support to the same approximations in QCD. Conversely, if the approximations fail dramatically in the toy theory, then it is unlikely that they are safe in QCD for the same kinematical region, particularly given the additional complications with non-Abelian gauge invariance, strong coupling, and nonperturbative hadronization.

Carrying this out requires a reasonable set of estimates for  $m_s$  and  $m_q$  for a specified range of kinematics. For  $Q \sim$  several GeV, the requirement that  $m/Q$  is small implies that  $m_q$  should be no larger than several hundred MeV and  $m_s$  should be such that  $|k^2|$  is also no larger than several hundred MeV for small  $k_T$ . Unfortunately, there are, to my knowledge, no systematic methods for precisely estimating values for the small components of parton momentum like  $m_q$  and  $|k^2|$ . On the other hand, phenomenological studies of transverse momentum dependence in semi-inclusive DIS suggest typical ranges for these parameters. Extractions of TMD functions find typical magnitudes for the intrinsic transverse momentum width between  $\approx 500$  MeV and 800 MeV [39–41]. Since  $m_q$  and  $m_s$  determine the widths and shapes of the  $k_T$  distribution, these estimates provide reasonable lower bounds on  $m_q$  and  $m_s$ . Earlier estimates gave smaller values. For example, a value of  $\langle k_T \rangle \sim 300$  MeV is roughly consistent with both the zero point energy of bag models as well as non-relativistic constituent quark models [42], and this is the value quoted in Ref. [43]. It is interesting to ask why phenomenological extractions tend to produce broader nonperturbative distributions than these expectations. (See also the discussion in Ref. [39].) For now this is left to be addressed in future work.

In this analysis I will use a range of values for  $m_q$  and  $m_s$  motivated by the above estimates, and examine the sensitivity to their variation for  $Q \sim 1\text{--}2$  GeV and moderate  $x_{\text{Bj}}$ . Sensitivity to the exact values of these parameters will be interpreted as a sign that extra care may be needed when estimating their effects on power corrections. I will return to the question of exact values for  $m_q$  and  $m_s$  in Sec. 4.4.1.

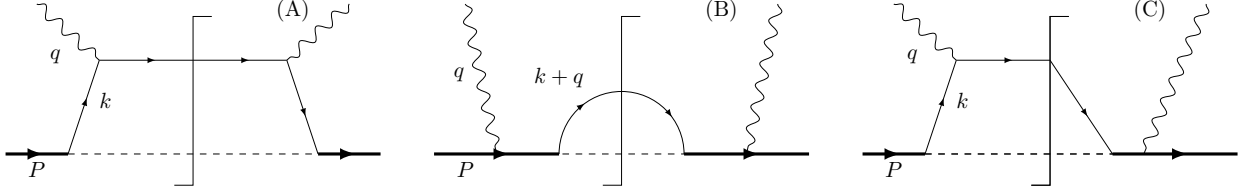


Figure 9: Figure taken from [38]. Contributions to the hadronic tensor from diagrams allowed by the interaction Lagrangian (99) to  $O(\alpha_{\text{em}}\lambda^2)$  in the couplings. Graph (A) is a manifestation of the familiar handbag diagram and represents the topology of the leading region. Graphs (B) and (C) are suppressed by powers of  $1/Q$  when  $k_T$  is small, but are needed for gauge invariance. The Hermitian conjugate for (C) is not shown. The momenta on the various legs are as indicated.

## 4.2 Exact kinematics

In this section I calculate the DIS structure functions from the Lagrangian  $\mathcal{L}_{\text{int}}$  in Eq. (99) at the lowest nontrivial order,  $O(\alpha_{\text{em}}\lambda^2)$ . The corresponding graphs derived from  $\mathcal{L}_{\text{int}}$  are shown in Fig. 9. Graph (A) has the familiar handbag diagram topology, while graphs (B) and (C) are power-suppressed at large  $Q$  but are needed for exact electromagnetic gauge invariance. I exclude the elastic limit of  $x_{\text{Bj}} = 1$  and require strictly  $W > M$ , so that diagrams with an on-shell nucleon in the final state are forbidden.

Graphs (B) and (C) represent the direct coupling of the photon to the nucleon, with production of a far off-shell nucleon in the intermediate state. In the quark-diquark field theory the coupling is point-like, while in QCD it corresponds to a higher-twist interaction internal to the nucleon wave function, with the final state quark interacting with the nucleon remnant to form a highly virtual intermediate state.

I begin by presenting the organization of the calculation of the graphs in Fig. 9, with no approximations whatsoever on kinematics. Of course, the result will not be factorized.

Later, I will compare with the canonical parton model approximations that factorize the graphs into a hard collision and a PDF contribution.

The exact calculation is organized by separating the integrand of the hadronic tensor into factors representing different parts of the squared amplitude,

$$W^{\mu\nu}(P, q) = \sum_{j \in \text{graphs}} \frac{1}{8\pi} \int \frac{dk^+ dk^- d^2\mathbf{k}_T}{(2\pi)^2} [\text{Jac}] \text{T}_j^{\mu\nu} [\text{Prop}]_j \delta(k^- - k_{\text{sol}}^-) \delta(k^+ - k_{\text{sol}}^+), \quad (100)$$

where  $k$  is the four-momentum of the interacting parton, and the sum over  $j$  runs over the graphs labeled by  $j \in \{A, B, C\}$ . The propagator denominators in Eq. (100) have been gathered into the factor  $[\text{Prop}]_j$ , and the traces over the  $\gamma$  matrices are denoted by  $\text{T}_j^{\mu\nu}$ . The resulting Jacobian factor associated with the integration over  $k^\pm$  is denoted as  $[\text{Jac}]$ . To simplify notation, I will fix  $\lambda = \sqrt{2}$  and drop all explicit factors of  $\lambda^2$  throughout the rest of this chapter. The  $\delta$ -functions stem from the on-shell conditions for the final state quark and scalar diquark,

$$(q + k)^2 - m_q^2 = 0, \quad (101a)$$

$$(P - k)^2 - m_s^2 = 0. \quad (101b)$$

Solving this system of equations for  $k^+ \equiv \xi P^+$  and  $k^-$  gives two solutions for  $k^-$ . In the limit of  $Q \rightarrow \infty$  with  $x_N$  and  $k_T$  fixed, the two solutions behave as  $k^- \sim \infty$  and  $k^- \sim 0$ , respectively. Selecting the latter as the physically relevant solution for DIS, I obtain the values of the light-cone parton momenta  $k_{\text{sol}}^\pm$  with on-shell final state quark and diquark,

$$k^- = k_{\text{sol}}^- \equiv \frac{\sqrt{\Delta} - Q^2(1 - x_N) - x_N(m_s^2 - m_q^2 - M^2(1 - x_N))}{2\sqrt{2} Q (1 - x_N)}, \quad (102a)$$

$$k^+ = k_{\text{sol}}^+ \equiv \frac{k_T^2 + m_q^2 + Q(Q + \sqrt{2}k^-)}{\sqrt{2}(Q + \sqrt{2}k^-)}, \quad (102b)$$

where  $k_T^2 = \mathbf{k}_T^2$ , and the discriminant  $\Delta$  is

$$\begin{aligned} \Delta = & [Q^2(1 - x_N) - x_N (M^2(1 - x_N) + m_q^2 - m_s^2)]^2 \\ & - 4x_N(1 - x_N)[k_T^2(Q^2 + x_N M^2) - Q^2 M^2(1 - x_N) + Q^2 m_s^2 + x_N M^2 m_q^2]. \end{aligned} \quad (103)$$

The parton virtuality is obtained by substituting Eqs. (102a)–(102b) into

$$k^2 = 2k^+ k^- - k_T^2. \quad (104)$$

The Jacobian factor in Eq. (100) is

$$[\text{Jac}] = \frac{x_N Q (2k^- + \sqrt{2}Q)}{4(1 - x_N)k^- Q^2 (\sqrt{2}k^- + 2Q) + 2\sqrt{2}[Q^4(1 - x_N) - (k_T^2 + m_q^2)x_N(Q^2 + x_N M^2)]}. \quad (105)$$

For this work, I am interested in the small- $|k^2|$  region where a parton model approximation might be reasonable. The  $k^-$  solution corresponding to large  $|k^2|$  is dealt with in an  $O(\lambda^2)$  treatment of the hard part. The exact propagator factors for each of the contributions in Fig. 9 are

$$[\text{Prop}]_A = \frac{1}{(k^2 - m_q^2)^2}, \quad (106a)$$

$$[\text{Prop}]_B = \frac{1}{((P + q)^2 - M^2)^2} = \frac{x_N^2}{(Q^2(1 - x_N) - M^2 x_N^2)^2}, \quad (106b)$$

$$[\text{Prop}]_C = \frac{1}{(k^2 - m_q^2)} \frac{x_N}{(Q^2(1 - x_N) - M^2 x_N^2)}. \quad (106c)$$

The numerator factors  $\mathbb{T}_j^{\mu\nu} = \mathbb{T}_j^{\mu\nu}(P, k, m_q, m_s)$  are obtained from the Dirac traces in each graph in Fig. 9,

$$\mathbb{T}_A^{\mu\nu} = \text{Tr} \left[ (\not{P} + M)(\not{k} + m_q)\gamma^\mu(\not{k} + \not{q} + m_q)\gamma^\nu(\not{k} + m_q) \right], \quad (107a)$$

$$\mathbf{T}_B^{\mu\nu} = \text{Tr} \left[ (\not{P} + M) \gamma^\mu (\not{P} + \not{q} + M) (\not{k} + \not{q} + m_q) (\not{P} + \not{q} + M) \gamma^\nu \right], \quad (107b)$$

$$\mathbf{T}_C^{\mu\nu} = 2 \text{Tr} \left[ (\not{P} + M) (\not{k} + m_q) \gamma^\mu (\not{k} + \not{q} + m_q) (\not{P} + \not{q} + M) \gamma^\nu \right], \quad (107c)$$

where the factor of 2 in  $\mathbf{T}_C^{\mu\nu}$  accounts for the Hermitian conjugate of Fig. 9(C). In evaluating the traces Eq. (107), it will be convenient to define the projected quantities

$$\mathbf{T}_j^g = \mathbf{P}_g^{\mu\nu} \mathbf{T}_{j\mu\nu}, \quad \mathbf{T}_j^{PP} = \mathbf{P}_{PP}^{\mu\nu} \mathbf{T}_{j\mu\nu}. \quad (108)$$

Evaluating the projections explicitly,

$$\mathbf{T}_A^g = -8 \left[ 2(P \cdot k + m_q M) k \cdot q + (k^2 - 3m_q^2) P \cdot k - 2Mm_q^3 + (m_q^2 - k^2) P \cdot q \right], \quad (109a)$$

$$\begin{aligned} \mathbf{T}_B^g = & 8 \left[ 2M^3 m_q + P \cdot k (2M^2 - Q^2) - 2(M^2 + Mm_q) Q^2 \right. \\ & \left. + 2k \cdot q (M^2 - P \cdot q) + [2(M^2 + Mm_q) + Q^2] P \cdot q \right], \end{aligned} \quad (109b)$$

$$\begin{aligned} \mathbf{T}_C^g = & -16 \left[ -2(P \cdot k)^2 + k^2 M^2 + (M^2 - m_q M) k \cdot q - M^2 m_q^2 + 2Mm_q Q^2 \right. \\ & \left. + (m_q^2 - Mm_q) P \cdot q - 2P \cdot k (k \cdot q + Mm_q - Q^2 + P \cdot q) \right], \end{aligned} \quad (109c)$$

$$\begin{aligned} \mathbf{T}_A^{PP} = & 4 \left[ 4(P \cdot k)^3 + 4(P \cdot k)^2 (Mm_q + P \cdot q) \right. \\ & - M P \cdot k (3k^2 M + 2M k \cdot q - 3Mm_q^2 - 4m_q P \cdot q) \\ & \left. - M^3 m_q (k^2 + 2k \cdot q - m_q^2) - M^2 (k^2 - m_q^2) P \cdot q \right], \end{aligned} \quad (109d)$$

$$\begin{aligned} \mathbf{T}_B^{PP} = & 4M^2 \left[ P \cdot k (4M^2 + Q^2) + 4M^2 (k \cdot q + Mm_q) - Q^2 (4M^2 + Mm_q) \right. \\ & \left. + [2k \cdot q + 4(M^2 + Mm_q) - Q^2] P \cdot q \right], \end{aligned} \quad (109e)$$

$$\begin{aligned} \mathbf{T}_C^{PP} = & 8M \left[ 4M(P \cdot k)^2 + M P \cdot k (2k \cdot q + 4Mm_q - Q^2) \right. \\ & - M^2 [2M(k^2 + k \cdot q - m_q^2) + m_q Q^2] \\ & \left. - [k^2 M - (2M + m_q)(2P \cdot k + Mm_q)] P \cdot q \right]. \end{aligned} \quad (109f)$$

Putting all the components together, the exact nucleon structure functions  $F_{1,2}$  can be written in terms of the  $k_T$ -unintegrated distributions,<sup>1</sup>

$$F_1(x_N, Q^2) = \int \frac{d^2\mathbf{k}_T}{(2\pi)^2} \mathcal{F}_1(x_N, Q^2, k_T^2), \quad (110a)$$

$$F_2(x_N, Q^2) = \int \frac{d^2\mathbf{k}_T}{(2\pi)^2} 2x_N \mathcal{F}_2(x_N, Q^2, k_T^2), \quad (110b)$$

where

$$\mathcal{F}_1(x_N, Q^2, k_T^2) = [\text{Jac}] \sum_j \left( -\frac{1}{2} \text{T}_j^g + \frac{2Q^2 x_N^2}{(M^2 x_N^2 + Q^2)^2} \text{T}_j^{PP} \right) [\text{Prop}]_j, \quad (111a)$$

$$\begin{aligned} 2x_N \mathcal{F}_2(x_N, Q^2, k_T^2) &= \frac{12Q^4 x_N^3 (Q^2 - M^2 x_N^2)}{(Q^2 + M^2 x_N^2)^4} \\ &\times [\text{Jac}] \sum_j \left( \text{T}_j^{PP} - \frac{(M^2 x_N^2 + Q^2)^2}{12Q^2 x_N^2} \text{T}_j^g \right) [\text{Prop}]_j. \end{aligned} \quad (111b)$$

For later convenience, the function  $\mathcal{F}_2$  in Eqs. (110b) and (111b) has been defined with a factor  $2x_N$  pulled out in order to more directly compare the behavior of the  $k_T$  dependence of the  $k_T$ -unintegrated functions (see Sec. 4.4 below).

Note that exact kinematics impose a specific upper bound on  $k_T$ . To determine its value, write  $W$  in the center-of-mass (c.m.) system,

$$W = p_q^0 + p_s^0 \Big|_{\text{c.m.}} = \sqrt{m_q^2 + k_T^2 + k_z^2} + \sqrt{m_s^2 + k_T^2 + k_z^2} \Big|_{\text{c.m.}}. \quad (112)$$

For fixed external kinematics, the maximum  $k_T$  occurs when  $k_z = 0$ . Setting

$$\sqrt{m_q^2 + k_{T\text{max}}^2} + \sqrt{m_s^2 + k_{T\text{max}}^2} = W \quad (113)$$

---

<sup>1</sup>Note that these are not PDFs, which are only defined after factorizing approximations are applied.

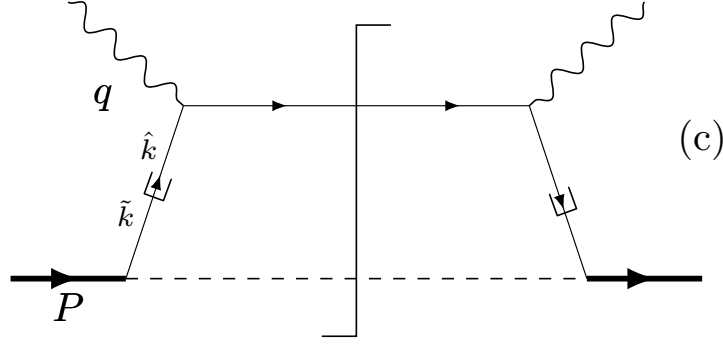


Figure 10: Figure taken from [38]. Application of collinear factorization to the  $O(\lambda^2)$  contribution in the theory from Sec. 4.1. The hooks represent the point of application of kinematic approximations on parton momentum.

and solving for  $k_{\Gamma\max}$  gives

$$k_{\Gamma\max} = \sqrt{\frac{[x_{Bj}(M^2 - (m_q + m_s)^2) + Q^2(1 - x_{Bj})][x_{Bj}(M^2 - (m_q - m_s)^2) + Q^2(1 - x_{Bj})]}{4x_{Bj}[Q^2(1 - x_{Bj}) + M^2x_{Bj}]}} , \quad (114)$$

where Eq. (12) has been used for  $W$ . Results for the exact structure functions will be shown in Sec. 4.4.

### 4.3 Factorization

Applying the steps of factorization discussed in Chapter 3 to Fig. 9(A) yields the factorized diagram shown in Fig. 10. From the hadronic tensor, one recovers the structure functions in the collinear (parton model) approximation,

$$F_i(x_{Bj}, Q^2) = \mathcal{H}_i(Q^2) f(x_{Bj}) + O\left(\frac{m^2}{Q^2}\right), \quad i = 1, 2, \quad (115)$$

where

$$\mathcal{H}_i(Q^2) \equiv P_i^{\mu\nu} \frac{1}{4\pi Q^2} \text{Tr} \left[ H_\mu(Q^2) \not{k}' H_\nu^\dagger(Q^2) \not{k} \right]. \quad (116)$$

At leading order,  $H^\mu(Q^2) = \gamma^\mu$ , so that the projected hard functions in Eq. (116) become

$$\mathcal{H}_1(Q^2) = \frac{1}{2}, \quad (117a)$$

$$\begin{aligned} \mathcal{H}_2(Q^2) &= \frac{Q^2 x_{\text{Bj}} \left( Q^2 - M^2 x_{\text{Bj}}^2 \right)}{\left( Q^2 + M^2 x_{\text{Bj}}^2 \right)^2} \\ &= x_{\text{Bj}} \left( 1 + O \left( \frac{M^2 x_{\text{Bj}}^2}{Q^2} \right) \right). \end{aligned} \quad (117b)$$

Thus, Eq. (115) produces the familiar  $F_1 = f(x_{\text{Bj}})/2$  and  $F_2 = x_{\text{Bj}} f(x_{\text{Bj}})$  result of the parton model.

In the limit of large  $Q$  and at fixed  $x_{\text{Bj}}$ , the graphs in Figs. 9(B)–(C) are suppressed by powers of  $m/Q$ , and the structure function in the factorized approximation comes entirely from the contribution in Fig. 9(A).

The PDF  $f(x_{\text{Bj}})$ , which describes the lower half of Fig. 10 in the factorized approximation, is

$$\begin{aligned} f(x_{\text{Bj}}) &= \int \frac{dk^- d^2 \mathbf{k}_T}{(2\pi)^4} \left( \frac{1}{\tilde{k}^2 - m_q^2} \right)^2 \text{Tr} \left[ \frac{\gamma^+}{2} (\tilde{k} + m_q) (\not{P} + M) (\tilde{k} + m_q) \right] \\ &\quad \times (2\pi) \delta_+ \left( (P - \tilde{k})^2 - m_s^2 \right). \end{aligned} \quad (118)$$

The on-shell  $\delta$ -function eliminates the integration over  $k^-$ , giving

$$k^- = - \frac{x_{\text{Bj}} \left[ k_T^2 + m_s^2 + (x_{\text{Bj}} - 1) M^2 \right]}{\sqrt{2} Q (1 - x_{\text{Bj}})}, \quad (119)$$

and the parton virtuality becomes

$$\tilde{k}^2 = -\frac{k_T^2 + x_{Bj} [m_s^2 + (x_{Bj} - 1)M^2]}{1 - x_{Bj}}. \quad (120)$$

Finally, the  $k_T$ -unintegrated functions  $\mathcal{F}_{1,2}$  defined in Eqs. (110) are given, in the collinear factorization approximation, by

$$\mathcal{F}_1(x_{Bj}, Q^2, k_T^2) = \mathcal{F}_2(x_{Bj}, Q^2, k_T^2) = \frac{(1 - x_{Bj}) [k_T^2 + (m_q + x_{Bj}M)^2]}{[k_T^2 + x_{Bj}m_s^2 + (1 - x_{Bj})m_q^2 + x_{Bj}(x_{Bj} - 1)M^2]^2}. \quad (121)$$

These structure functions only depend on  $x_{Bj}$  and  $k_T^2$  and are independent of  $Q^2$ , as would be anticipated for the parton model approximation. The equality  $\mathcal{F}_1 = \mathcal{F}_2$  is a version of the Callan-Gross relation [44], but for the unintegrated structure functions. Note that the parton virtuality  $\tilde{k}^2$  in Eq. (120) in the PDF is an approximation to the true parton virtuality.

To develop intuition about the approximations just made on the parton momentum, it is useful to Taylor expand the exact  $k^+$ ,  $k^-$  and  $k^2$  from Eqs. (102)–(103) through the first several powers of  $m^2/Q^2$ ,

$$\begin{aligned} \xi = x_{Bj} & \left[ 1 + \frac{k_T^2 + m_q^2 - x_{Bj}^2 M^2}{Q^2} \right. \\ & \left. - \frac{x_{Bj}^3 M^2 (k_T^2 + m_q^2) + x_{Bj} (k_T^2 + m_q^2) (k_T^2 + m_s^2 - M^2) - 2M^4 x_{Bj}^4 (x_{Bj} - 1)}{Q^4 (x_{Bj} - 1)} \right] \\ & + O\left(\frac{m^6}{Q^6}\right), \end{aligned} \quad (122)$$

$$\begin{aligned}
k^- = & -\frac{x_N}{Q\sqrt{2}} \left[ \frac{k_T^2 + m_s^2 + (x_N - 1)M^2}{1 - x_N} - \frac{x_N (k_T^2 + m_q^2) (k_T^2 + m_s^2)}{Q^2(x_N - 1)^2} \right] \\
& + O\left(m \cdot \frac{m^5}{Q^5}\right), \tag{123}
\end{aligned}$$

$$\begin{aligned}
k^2 = & -\frac{k_T^2 + x_N [m_s^2 + (x_N - 1)M^2]}{1 - x_N} \\
& - \frac{x_N (k_T^2 + m_q^2) \left( k_T^2 + [m_s + (x_N - 1)M] [m_s - (x_N - 1)M] \right)}{Q^2(x_N - 1)^2} \\
& + O\left(m^2 \cdot \frac{m^4}{Q^4}\right). \tag{124}
\end{aligned}$$

Here I have expressed  $\xi$  in terms of  $x_{Bj}$  because the leading power contribution to  $\xi$  is conventionally written as  $x_{Bj}$ . The lowest non-vanishing powers in Eqs. (123)–(124) match Eqs. (119)–(120), respectively, confirming that the approximations leading up to Eq. (121) are valid for sufficiently large  $Q$ . For  $k^-$  and  $k^2$ , it is more convenient to maintain expressions in terms of  $x_N$ . Of course,  $x_N$  may be replaced everywhere here by  $x_{Bj}$  without changing the validity of the expressions.

The formula for the  $O(\lambda^2)$  PDF in Eq. (118) could also have been obtained directly from the operator definition of the collinear PDF, calculated in the scalar diquark field theory. The definition of the PDF emerges automatically from the constraints of factorization. This is an important aspect of the steps above, and is a key of factorization derivations.

#### 4.4 Exact and factorized structure functions: A comparison

In this section I compare DIS structure functions in the exact calculation of Sec. 4.2 with the corresponding calculations in the factorization approximation of Sec. 4.3. I restrict consideration to unintegrated structure functions, differential in  $k_T$ . This permits a direct examination of the impact of the approximations from the previous section point-by-point

in transverse momentum. Exact kinematics involve sensitivity to all components of parton momentum, including parton virtuality, so the notion of factorization with a collinear PDF will not apply to the exact case. However, the terms in a direct  $m^2/Q^2$  expansion of the exact result can hint at ways to correct the collinear picture.

The power counting in Eq. (78), with  $m^2 \ll Q^2$ , must be reasonably well satisfied for the steps of the previous section to constitute a good approximation. Namely, the magnitude of the quark virtuality  $|k^2|$  must be small relative to the hard scale  $Q^2$ . While the distribution of  $k^2$  in an isolated proton is an intrinsic property of the bound state, the range of  $k^2$  probed in a DIS collision is sensitive to external kinematical parameters like  $x_{Bj}$  and  $M$ . Therefore, the validity of the  $|k^2| \ll Q^2$  assumption also depends on external kinematics.

To make this clear, one may directly examine the behavior of Eqs. (102)–(103) in various limiting cases. For example, consider fixed  $Q^2$  and the limit of  $x_N \rightarrow 1$ . The  $\pm$  components of  $k$  are then

$$k^+ \rightarrow \frac{Q}{\sqrt{2}} \left( 1 + \frac{m_q^2 - m_s^2}{M^2 + Q^2} \right) + O(|1 - x_N|), \quad (125a)$$

$$k^- \rightarrow -\frac{1}{2\sqrt{2}Q} \left( Q^2 - M^2 + \frac{(M^2 + Q^2)(2k_T^2 + m_s^2 + m_q^2)}{m_s^2 - m_q^2} \right) + O(|1 - x_N|). \quad (125b)$$

Next taking the large- $Q^2$  limit, the quark virtuality becomes

$$\lim_{m/Q \rightarrow 0} \lim_{x_N \rightarrow 1} k^2 = -\frac{Q^2}{2} \left( 1 + \frac{2k_T^2 + m_q^2 + m_s^2}{m_s^2 - m_q^2} \right). \quad (126)$$

The typical value of  $-k^2$  is therefore of order  $Q^2$  in the simultaneous limits of large  $x_N$  and large  $Q$ . [From Eq. (124), this remains true if the order of the limits is reversed.] The increasing size of  $|k^2|$  with increasing  $x_{Bj}$  is a symptom of parton kinematics becoming non-collinear. As  $x_N$  becomes very large, it eventually becomes questionable whether an interpretation in terms of universal collinear parton densities is possible. I will return to this discussion in Sec. 4.4.4.

#### 4.4.1 Values for $m_q$ and $m_s$

To proceed with numerical calculations, I must return to the discussion in Sec. 4.1.2 regarding choices for  $m_q$  and  $m_s$ . In QCD, the mass of the target remnant will tend to grow with energy and  $Q^2$ , so the choice of  $m_s$  requires greater care. Lower bounds on  $m_s$  can be obtained from elementary kinematic considerations. Since the invariant mass of the final state system cannot be less than that of the lowest baryon state, namely the nucleon, then

$$W^2(x_{\text{Bj}}, Q) = (p_s + p_q)^2 > M^2. \quad (127)$$

Working in the rest frame of the quark–diquark system,

$$M - m_q < m_s \leq W(x_{\text{Bj}}, Q) - m_q. \quad (128)$$

This constrains  $m_s$  to lie in a band whose width depends on  $x_{\text{Bj}}$  and  $Q$ , with the range decreasing as  $x_{\text{Bj}} \rightarrow 1$ .

I am interested in the numerical effects of the factorization approximations for some selected fixed values of  $k^2$ . However,  $k^2$  is determined by external kinematics and the field theory parameters  $m_q$  and  $m_s$ . Therefore, I will choose  $m_s$  on a case-by-case basis to ensure specific values of  $k^2$  designed to test power counting assumptions for reasonable  $k^2$ . The relationship between  $k^2$  and  $m_s$  depends on other kinematic parameters, so I will need to choose a new  $m_s$  for each kinematical scenario in order to keep  $k^2$  fixed. To see this, note that for fixed  $x_{\text{Bj}}$  and large  $Q^2$ , the relationship between  $m_s$  and  $k^2$  is

$$m_s^2 \approx (1 - x_{\text{Bj}}) \left( M^2 + \frac{|k^2|}{x_{\text{Bj}}} \right). \quad (129)$$

For different  $x_{\text{Bj}}$ ,  $m_s$  must be modified if  $k^2$  is to remain fixed. In the next section I will use the exact relationship between  $m_q$ ,  $m_s$ ,  $k^2$  and  $k_{\text{T}}$  to choose specific values for  $m_s$  and  $m_q$  so that  $|k^2|$  is no greater than several hundred MeV at small  $k_{\text{T}}$ .

If the actual typical  $k_T$ ,  $k^2$ , and  $m_q$  are clustered around a range of very small values, then collinear factorization might be satisfied with very high accuracy even for relatively small  $Q$ . However, phenomenological studies of transverse momentum dependence in semi-inclusive DIS restrict typical  $k_T$ -widths to  $\approx 500$ – $800$  MeV [39–41], while model-based estimates suggest  $\langle k_T \rangle \approx 300$  MeV [43]. (See also Ref. [45] and references therein.) Thus, the values I choose for  $m_q$  and  $|k^2|$  (or  $m_s$ ) cannot be simultaneously much less than about 300 MeV without creating tension with measurements of transverse momentum dependence in semi-inclusive DIS. Also, Eq. (128) means that  $m_s$  cannot be much less than  $M$  if  $m_q$  is small. Therefore, I will choose combinations of  $m_s$  and  $m_q$  such that  $|k^2|$  is several hundred MeV,  $m_q$  is in the vicinity of  $m_q \approx 300$  MeV, and the peak of the transverse momentum distribution is not greater than 300 MeV. [This peak location is somewhat small relative to the above examples from phenomenology; this will ensure that I underestimate  $O(k_T^2/Q^2)$  kinematical errors to the collinear factorization formula.] The details of the resulting example calculations are discussed in the following.

#### 4.4.2 Which power corrections are most important?

In the canonical factorization approximations of Sec. 4.3, there are four independent types of neglected power-suppressed terms:

$$\sim \frac{m_q^2}{Q^2}; \quad \text{Type – A} \quad (130a)$$

$$\sim \frac{k^2}{Q^2}; \quad \text{Type – B} \quad (130b)$$

$$\sim \frac{k_T^2}{Q^2}; \quad \text{Type – C} \quad (130c)$$

$$\sim \frac{M^2}{Q^2}. \quad \text{Type – D} \quad (130d)$$

For the purposes of power counting, I use  $k^2$  as the independent variable for Type–B corrections in place of  $m_s^2$ . Of course, beyond leading power-law corrections, these suppression

factors come in combinations. For example, the  $\sim O(m^6/Q^6)$  power corrections include terms proportional to

$$\frac{k^2}{Q^2} \times \frac{k_T^2}{Q^2} \times \frac{M^2}{Q^2}. \quad (131)$$

Therefore, it is not generally meaningful to address Type–D suppressed corrections independently of Type–B and Type–C suppressed corrections. Effects from  $M^2/Q^2$  in higher powers are sensitive to the range of  $k^2$ .

Still, it is possible in principle that corrections suppressed by exactly one type of factor in Eqs. (130a)–(130d) alone might be important. For example, it is reasonable to speculate that terms with *only* a Type–D suppression may be large, whereas terms with any of Type–A through Type–C suppressions are negligible. Now that the exact and factorized calculations of the structure functions in the quark–diquark theory are available to me, I can test the feasibility of such an approximation directly by examining the relative importance of Type–A through Type–C corrections as compared with pure Type–D corrections. When corrections from isolated  $M/Q$  terms are useful, the quality of the approximations from Sec. 4.3 should nonetheless be nearly independent of the exact values of  $k_T$ ,  $m_q$  and  $k^2$ , so long as they lie within a reasonable range. If, however, small variations in  $k_T$ ,  $m_q$  or  $k^2$  produce large changes in the quality of the factorization approximation, then target mass corrections from terms like Eq. (131) are too large to ignore, and it is unlikely that isolated  $M/Q$  corrections alone can improve accuracy.

To illustrate the numerical dependence of the structure functions on the mass parameters  $m_q$  and  $m_s$ , I show in Fig. 11 the unintegrated  $\mathcal{F}_1(x_N, Q^2, k_T^2)$  structure function, weighted by  $k_T$ , as a function of  $k_T$ . (The results for the  $\mathcal{F}_2$  structure function are qualitatively similar, and do not alter the conclusions.) I emphasize that these plots correspond to the  $k^-$  solution in Eq. (102b) for which  $|k^2|$  may be small enough to yield parton model kinematics. The other solution is dealt with in the  $O(\lambda^2)$  hard part. The kinematics are chosen to be

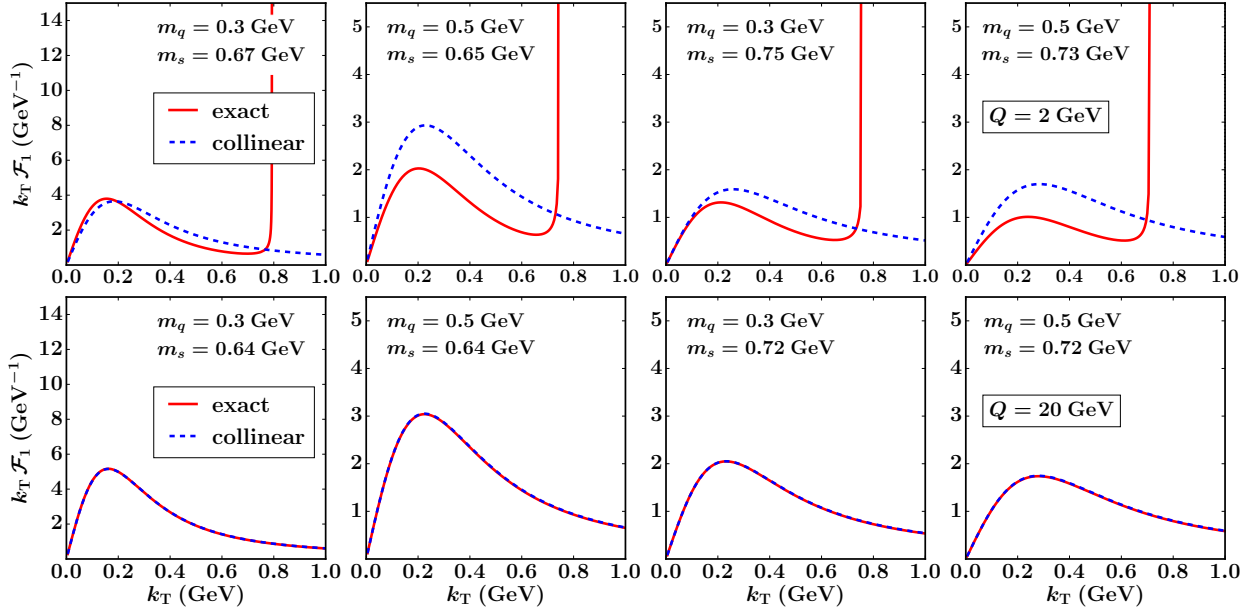


Figure 11: Figure taken from [38]. The unintegrated structure function  $k_T \mathcal{F}_1$  for  $x_{Bj} = 0.6$  and  $Q = 2$  GeV (top row) and  $Q = 20$  GeV (bottom row), for different values of  $m_q$  and  $m_s$  calculated using both the exact expressions (solid red curves) and the canonical collinear factorization approximation (dashed blue curves). The choices of  $m_s$  are to fix  $k^2$  at the values discussed in Sec. 4.4.1. At the higher  $Q$  value the collinear calculation is almost indistinguishable from the exact, while at the lower  $Q$  value the exact calculation diverges as it approaches the kinematical upper limit of  $k_T$ .

representative of typical values relevant to large- $x_{Bj}$  studies at modern accelerator facilities,  $x_{Bj} = 0.6$  for  $Q = 2$  GeV, which corresponds to  $W \approx 2$  GeV, and a higher  $Q$  value,  $Q = 20$  GeV, characteristic of the deep scaling region. For the quark mass I take  $m_q = 0.3$  and  $0.5$  GeV, while the values for the diquark mass  $m_s$  are chosen to ensure that the quark virtuality  $v \equiv \sqrt{-k^2} = 300$  MeV or  $500$  MeV at  $k_T = 0$ . These values are chosen to be consistent with the kinematical constraints discussed in Sec. 4.4.1 and, as seen in Fig. 11, they produce distributions peaked at  $k_T$  slightly less than  $\approx 300$  MeV. For the exact calculation, there is an integrable kinematical square root divergence at  $k_T = k_{T\max}$  that is an artifact of the simplification to a  $2 \rightarrow 2$  process. All graphs from Fig. 9 are included now, as required for an  $O(\lambda^2)$  treatment without kinematical approximations. Note that with exact kinematics it is now only the sum of the graphs in Fig. 9 that is gauge invariant.

At the higher  $Q$  value in Fig. 11 (bottom row), the factorized structure function is almost indistinguishable from the exact result. This validates that the approximate and exact calculations match in the large- $Q$  limit, even for  $k_T \gtrsim 1$  GeV. By contrast, for the lower  $Q$  value in Fig. 11 (top row), the exact calculation shows a clear deviation from the factorization approximation, both in size and shape. It is clear that if corrections of order  $\sim 10\%$  are important, then the roles of Type-A through Type-C corrections need to be considered on the same footing with Type-D corrections. The top row of Fig. 11 shows that the quality of the collinear factorization approximations for  $Q \sim \text{few GeV}$  is indeed sensitive to the exact values of  $k^2$  and  $m_q$ , whereas the applicability of the collinear factorization paradigm assumes independence of these nonperturbative parameters.

Even for the large  $Q$  value in Fig. 11, the shape of the  $k_T$  distribution is sensitive to the precise values of  $m_q$  and  $m_s$ , with the unintegrated structure function diverging for small values of  $k_T$  as  $m_q$  and  $m_s \rightarrow 0$ . This is to be expected because the  $k_T$  dependence near  $k_T \approx 0$  is determined by the nonperturbative physics that regulates the infrared limit in the hadron wave function. More relevant is that the approximation errors are vanishingly small at  $k_T < 1$  GeV and large  $Q$ , independently of  $m_s$  and  $m_q$ , as long as they lie within a

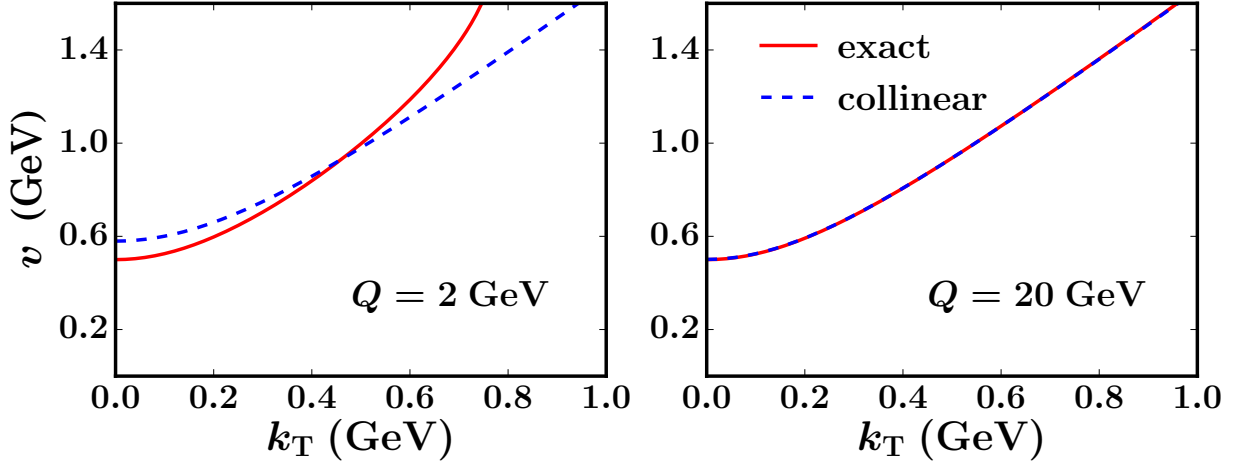


Figure 12: Figure taken from [38]. The dependence of the parton virtuality  $v \equiv \sqrt{-k^2}$  on  $k_T$  evaluated at exact (solid red curves) and approximate collinear (dashed blue curves) kinematics, for  $x_{Bj} = 0.6$  at fixed  $Q = 2$  GeV (left panel) and  $Q = 20$  GeV (right panel), for quark mass  $m_q = 0.3$  GeV and spectator diquark mass  $m_s$  corresponding to  $v(k_T = 0) = 0.5$  GeV (see Table 1).

reasonable range as discussed in Sec. 4.4.1.

Note also that the incoming quark virtuality  $k^2$  is forced by kinematics to decrease to large negative values with increasing  $k_T$ . This is illustrated in Fig. 12, which shows the quark virtuality  $v$  as a function of  $k_T$  for fixed  $x_{Bj} = 0.6$  and  $Q = 2$  and 20 GeV. The exact and approximate results for  $v$  coincide at the high  $Q$  value but differ visibly small  $k_T$  and large  $k_T$  for the lower  $Q$ . At large  $k_T$ , the virtuality becomes linear with  $k_T$ , in accordance with Eq. (124) in the  $m/Q \rightarrow 0$  limit. Even assuming  $v < 1$  GeV for  $k_T < 1$  GeV, the exact value of  $k^2$  (and its dependence on  $k_T$ ) impacts the shape of the  $k_T$  distribution and the quality of the usual factorization approximations.

### 4.4.3 The role of transverse momentum

The factorization approximations discussed in Sec. 4.3 apply to the limit in which  $k_T/Q \sim m/Q \ll 1$ . In QCD, however, there are ultraviolet divergences from the integrals over transverse momentum in the PDF. The standard way to deal with this is to renormalize the PDF.

When  $Q$  is large, vertex corrections involve  $O(Q^2)$  off-shell propagators, so the appropriate renormalization scale is  $\mu \sim Q$ . By comparison, the kinematics of real gluon emission restrict “large” transverse momentum to be  $\lesssim O(Q\sqrt{1-x_{Bj}})$  [see Eq. (114)], so that the corresponding scale is  $\mu \sim Q\sqrt{1-x_{Bj}}$ . (In the model calculation, the spectator plays the role kinematically of a real gluon emission.) If  $x_{Bj}$  is not too large and  $Q \gg m$ , this mismatch between real and virtual emissions is not a serious problem because  $k_{T\max}$  is at least  $O(Q)$  for all graphs. The collinear parton distribution Eq. (118) becomes, schematically,

$$f(x_{Bj}) \propto \int_{M_{\text{cut}}^2}^{k_{T\max}^2 \sim Q^2} \frac{dk_T^2}{k_T^2} \propto \ln \frac{Q^2}{m^2}, \quad (132)$$

where the lower bound  $M_{\text{cut}}$  on the integration is to restrict attention to the large  $k_T \sim Q$  component of the integration [namely, the contribution to  $f(x_{Bj})$  from the large- $k_T$  region varies logarithmically with  $Q^2$ ]. As long as  $x_{Bj}$  is not too large, Eq. (132) is consistent with the corresponding logarithms from virtual loops. The resulting  $\log Q^2$  dependence is the familiar  $Q^2$  dependence that arises in the standard DGLAP-type evolution equations which produce the logarithmic scaling violations of PDFs [46–48].

However, if  $x_{Bj} \approx 1 - m^2/Q^2$ , then  $k_{T\max}$  is no greater than  $O(m)$  and the large logarithms of Eq. (132) are no longer present. The ultraviolet divergences from loop integrals still need to be renormalized at the scale of the virtual photon ( $\mu \sim Q$ ), so  $\ln Q^2$  behavior from loop diagrams remain. This creates a mismatch between the renormalization of real and virtual emissions. In QCD, the mismatch appears in high-order  $\alpha_s(Q)$  contributions in the form of uncontrolled large finite parts, well-known as  $\ln(1-x_{Bj})$  effects that, at a minimum, need

to be resummed to all orders [49–52].

The small- $k_{\text{Tmax}}$  problem is evident in the scalar diquark theory in Fig. 11 for the  $x_{\text{Bj}} = 0.6$  and  $Q = 2$  GeV kinematics. The value of  $k_{\text{T}}$  here approaches its kinematic upper bound at  $k_{\text{T}} \lesssim 1$  GeV, so the  $k_{\text{T}} \ll Q$  approximation begins to fail already for  $k_{\text{T}} \sim$  several hundred MeV. By contrast, for the higher  $Q$  value in Fig. 11, the kinematical upper bound on  $k_{\text{T}}$  lies well above 1 GeV (off the scale of the graphs). In QCD, this large  $k_{\text{T}}$  region is generally describable by perturbative real gluon radiation.

To highlight the trends in  $k_{\text{T}}$  dependence at larger  $x_{\text{Bj}}$  and moderate  $Q$ , it is useful to consider the exact  $k_{\text{Tmax}}$  from Eq. (114) in various limits. For example, in the limit of small  $m/Q$  with fixed  $x_{\text{Bj}}$ ,

$$k_{\text{Tmax}} = \frac{Q}{2} \left[ \sqrt{\frac{1-x_{\text{Bj}}}{x_{\text{Bj}}}} - \sqrt{\frac{x_{\text{Bj}}}{1-x_{\text{Bj}}}} \frac{(2m_q^2 + 2m_s^2 - M^2)}{2Q^2} + O\left(\frac{m^4}{Q^4} \left(\frac{x_{\text{Bj}}}{1-x_{\text{Bj}}}\right)^{3/2}\right) \right]. \quad (133)$$

This is the fixed- $x_{\text{Bj}}$  Bjorken limit applied to  $k_{\text{Tmax}}$ , but a truncation of the series is liable to be a poor approximation to  $k_{\text{Tmax}}$  if  $x_{\text{Bj}}$  is close to one. In that limit, it is more meaningful to Taylor expand first in powers of small  $(1-x_{\text{Bj}})$  with fixed  $Q$ ,

$$k_{\text{Tmax}} = \frac{1}{2M} \sqrt{(m_q^2 - M^2)^2 + (m_s^2 - m_q^2)^2 + (m_s^2 - M^2)^2 - m_s^4 - m_q^4 - M^4} + O\left((1-x_{\text{Bj}}) \frac{Q^3}{m^2}\right). \quad (134)$$

There is thus a finite and generally nonzero upper bound on  $k_{\text{T}}$  as  $x_{\text{Bj}}$  becomes large. Indeed, if the collision is exactly elastic,  $x_{\text{Bj}} \rightarrow 1$ , and Eq. (12) requires  $m_q + m_s = M$ , which from Eq. (134) gives  $k_{\text{Tmax}} = 0$ .

To quantify errors in the integrations over  $k_{\text{T}}$ , I define the integral over the exact structure function  $\mathcal{F}_1$ , for a fixed  $x_{\text{Bj}}$  and  $Q$ , between  $k_{\text{T}} = 0$  and the kinematic maximum,  $k_{\text{Tmax}}$ ,

$$I(x_{\text{Bj}}, Q) \equiv \int_0^{k_{\text{Tmax}}} dk_{\text{T}} k_{\text{T}} \mathcal{F}_1^{\text{exact}}(x_{\text{Bj}}, Q, k_{\text{T}}). \quad (135)$$

Table 1: Ratio of integrals  $I/\widehat{I}$  of exact to collinear  $k_T \mathcal{F}_1$  structure functions, where  $I \equiv I(x_{Bj}, Q)$  [Eq. (135)] and  $\widehat{I} \equiv \widehat{I}(x_{Bj}, Q, k_{\text{cut}})$  [Eq. (136)], for different values of  $m_q$  and  $m_s$  as in Fig. 11, for  $x_{Bj} = 0.6$  and  $Q = 2$  and 20 GeV. The approximate collinear integral is evaluated for  $k_{\text{cut}} = Q$  and  $k_{\text{cut}} = k_{T\text{max}}$ .

	$Q = 2$ GeV				$Q = 20$ GeV			
$m_q$ (GeV)	0.3	0.5	0.3	0.5	0.3	0.5	0.3	0.5
$m_s$ (GeV)	0.67	0.65	0.75	0.73	0.64	0.64	0.72	0.72
$I/\widehat{I}(k_{T\text{max}})$	0.88	0.64	0.76	0.57	1.00	1.00	1.00	1.00
$I/\widehat{I}(Q)$	0.67	0.45	0.49	0.35	0.90	0.88	0.86	0.85

For the analogous calculation in the factorization approximation, on the other hand, there is no obvious upper bound on the  $k_T$  integration. In standard treatments, the upper limit, which I denote by  $k_{\text{cut}}$ , need only be  $O(Q)$ , with the exact value otherwise arbitrary. Reasonable choices for  $k_{\text{cut}}$  could be  $k_{T\text{max}}$  or  $Q$ , for example. I define the integral over the structure function in the collinear approximation as

$$\widehat{I}(x_{Bj}, Q, k_{\text{cut}}) \equiv \int_0^{k_{\text{cut}}} dk_T k_T \mathcal{F}_1^{\text{approx}}(x_{Bj}, Q, k_T). \quad (136)$$

In the limit of large  $Q$ , as long as  $O(m) \ll k_{\text{cut}} < O(Q)$ , the factorization approximation should obey

$$\widehat{I}(x_{Bj}, Q, k_{\text{cut}}) \approx I(x_{Bj}, Q). \quad (137)$$

In QCD, deviations from the equality of  $I$  and  $\widehat{I}$  are attributed to higher orders in  $\alpha_s(Q)$ . If, however, the ratio  $I/\widehat{I}$  deviates significantly from unity for a range of reasonable values for  $k_{\text{cut}}$ , the validity of the collinear factorization approximation begins to become questionable. Also,  $k_{T\text{max}}$  needs to be  $\gtrsim 1$  GeV for gluon radiation effects to be perturbative. This is not the case for the  $Q = 2$  GeV results in Fig. 11.

In Table 1 I display the values for  $I/\widehat{I}$  using  $k_{\text{cut}} = k_{\text{Tmax}}$  and  $k_{\text{cut}} = Q$  for the upper limit on the  $k_{\text{T}}$  integration in  $\widehat{I}$ , for kinematics corresponding to Fig. 11, namely  $x_{\text{Bj}} = 0.6$  with  $Q = 2$  and 20 GeV. The values of  $m_q$  and  $m_s$  are also chosen to be as in Fig. 11, with  $m_q = 0.3$  or 0.5 GeV, and  $m_s$  computed by fixing the virtuality  $v = 0.3$  GeV (smaller  $m_s$  values,  $\sim 0.64 - 0.67$  GeV) or  $v = 0.5$  GeV (larger  $m_s$  values,  $\sim 0.72 - 0.75$  GeV) at  $k_{\text{T}} = 0$ . For the larger  $Q$  value, the results confirm that  $I/\widehat{I}$  is approximately unity for  $k_{\text{cut}}$  between  $k_{\text{Tmax}}$  and  $Q$ , independently of the exact values of  $m_q$  and  $m_s$ , so long as those values give reasonable  $k_{\text{T}}$  distributions that peak at  $\approx$  few hundred MeV. In contrast, for the smaller value of  $Q = 2$  GeV, the ratio  $I/\widehat{I}$  deviates significantly from unity, and has stronger dependence on the exact value of  $k_{\text{cut}}$ . Note that for  $Q = 2$  GeV and  $x_{\text{Bj}} = 0.6$ , the maximum transverse momentum  $k_{\text{Tmax}} < 1$  GeV, so that the dependence on the  $k_{\text{T}}$  cutoff likely has its own nonperturbative contributions.

#### 4.4.4 Purely kinematic target mass corrections

In the context of factorization derivations, the notion of purely kinematic target mass corrections is unambiguous. To see this, first return to the factorization approximations of Sec. 4.3, and assume that for a fixed  $x_{\text{Bj}}$  and  $Q$  the ratio  $m^2/Q^2$  is small enough that a power-law expansion exists and has reasonable convergence. The first few powers of the Taylor expansion of momentum components were displayed in Eqs. (122)–(124). Now assume that, beyond the lowest non-vanishing powers, the only non-negligible correction terms are those with powers of  $M/Q$  alone, while terms suppressed by higher powers of  $k_{\text{T}}/Q$ ,  $m_q/Q$  or  $m_s/Q$  are small. Upon dropping these, Eqs. (122)–(124) become

$$\xi \rightarrow \xi_{\text{TMC}} \equiv x_{\text{Bj}} \left[ 1 - \frac{x_{\text{Bj}}^2 M^2}{Q^2} + \frac{2M^4 x_{\text{Bj}}^4}{Q^4} + \dots \right] = x_{\text{N}}, \quad (138)$$

$$k^- \rightarrow k_{\text{TMC}}^- \equiv - \frac{x_{\text{N}} [k_{\text{T}}^2 + m_s^2 + (x_{\text{N}} - 1)M^2]}{\sqrt{2}Q(1 - x_{\text{N}})}, \quad (139)$$

$$k^2 \rightarrow k_{\text{TMC}}^2 \equiv - \frac{k_{\text{T}}^2 + x_{\text{N}} [m_s^2 + (x_{\text{N}} - 1)M^2]}{1 - x_{\text{N}}}. \quad (140)$$

Comparing with Eqs. (119) and (120) confirms that using Eqs. (138)–(140) is identical to simply replacing  $x_{Bj} \rightarrow x_N$  in the standard collinear parton model approximation, Eq. (121). Indeed, the replacement of  $\xi = x_N$  by  $\xi = x_{Bj}$  in Eq. (80) was unnecessary for deriving the factorization formula; the steps leading to the factorized hadronic tensor in Eq. (95) are equally valid if  $x_{Bj}$  is replaced everywhere by  $x_N$ .

There is, therefore, a natural meaning to purely kinematic TMCs: They are the terms that are kept in the factorization derivation when all components of external, physical momenta, such as Eqs. (7)–(8), are left unapproximated. Specifically, purely kinematical TMCs are those that arise from keeping the minus component of the target momentum  $P$ , which is normally approximated to zero, exact in Eq. (7). This automatically results in  $x_N$ -scaling (often referred to in the literature as “ $\xi$ -scaling”, not to be confused with the  $\xi$  variable used for the “+” component of  $k$  here), as opposed to  $x_{Bj}$ -scaling.

Power corrections beyond those accounted for in Eqs. (138)–(140) are associated with  $k_T$ ,  $m_q$  and  $k^2$  dependence, and hence are unavoidably coupled to bound state dynamics that are both nonperturbative and non-collinear (for  $k_T \sim m$ ). For  $x_{Bj} > 0.5$ , some of the higher power corrections that only involve  $k_T$ ,  $m_q$  and  $m_s$  are enhanced by powers of  $x_{Bj}/(1 - x_{Bj})$  relative to those that only contain  $M$  [see Eqs. (122)–(124) and Eq. (133)]. Moreover, the integration over  $k_T$  in QCD includes the full range of nonperturbative transverse momentum between 0 and  $\sim 1$  GeV, and power corrections that depend on  $k_T$  can become quite large. By contrast, purely kinematical TMCs are suppressed at low  $x_{Bj}$  by powers of  $x_{Bj}^2 M^2/Q^2$ . This suggests that purely kinematical TMCs alone are not likely to be sufficient in most interesting large- $x_{Bj}$  cases, except perhaps for unusually heavy hadrons. In other words, once  $Q$  is small enough (or  $x_{Bj}$  large enough) for there to be sensitivity to purely kinematic TMCs, the effects of other types of power corrections, including non-collinear effects, already come into play.

To numerically compare purely kinematical TMCs with other power correction effects, Fig. 13 shows the unintegrated structure  $\mathcal{F}_1$  structure function for the exact calculation,

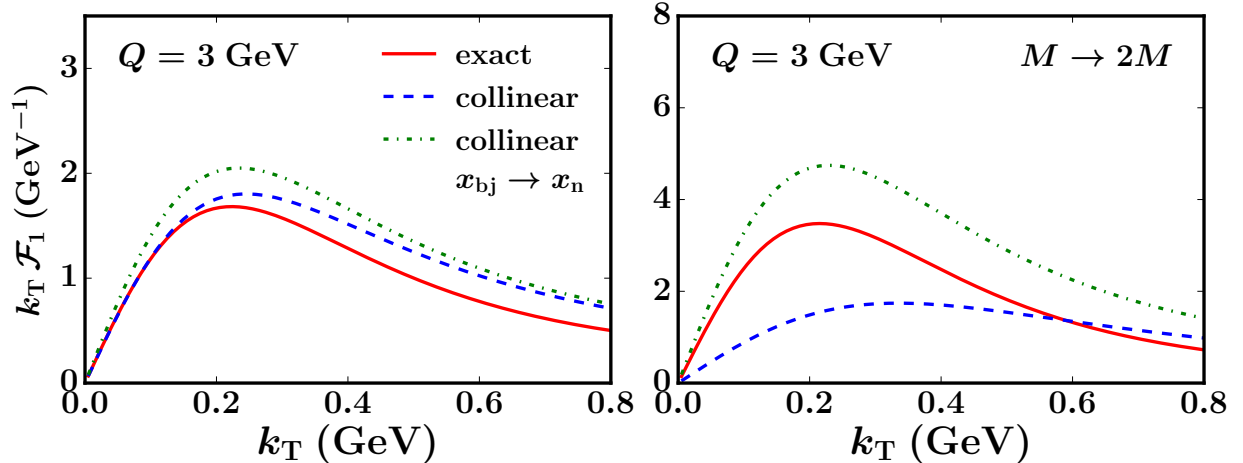


Figure 13: Figure taken from [38]. Unintegrated structure function  $k_T \mathcal{F}_1$  for  $x_{Bj} = 0.6$  and  $Q = 3$  GeV, with quark mass  $m_q = 0.3$  GeV and virtuality  $v = 0.5$  GeV for the exact result (solid red curves), approximate collinear approximation (dashed blue curves), and collinear result with the replacement  $x_{Bj} \rightarrow x_N$  (dot-dashed green curves). The right-hand panel shows the results when the nucleon mass increased by a factor of 2.

with  $x_{Bj} = 0.6$  and  $Q = 3$  GeV, and with the standard collinear approximation and with the collinear result corrected for target mass effects by rescaling  $x_{Bj} \rightarrow x_N$ . Perhaps surprisingly, in this case the target mass corrected form deviates further from the exact result than the uncorrected collinear approximation. The expectation that purely kinematic TMCs dominate if  $M$  is especially large is borne out in Fig. 13, where I compare the various calculations for the case when  $M \rightarrow 2M$ . Here, powers of  $M/Q$  are large and the expansion in powers of  $M/Q$  certainly fails. Thus, the  $x_{Bj} \rightarrow x_N$  replacement indeed improves the approximation, though there are still significant errors from the remaining neglected  $m/Q$  corrections that are not particularly small.

The phrase “purely kinematic TMCs” is sometimes used to characterize the  $O(M^2/Q^2)$  correction terms first derived in the classic OPE analysis of Georgi and Politzer [43]. The

results for the mass corrected structure functions in Ref. [43] [see Eqs. (4.19)–(4.22)] differ from those in Eqs. (138)–(140), in the form of additional corrections involving integrals over parton momentum fractions. These differences arise because [43] imposes the exact constraint  $\tilde{k}^2 = 0$  for quark momentum from the outset. As explained by Ellis *et al.* [53], the additional corrections in Ref. [43] originate from the integration over  $k_T$  when  $\tilde{k}^2$  is held fixed at zero. In particular, Ref. [53] finds that the unintegrated structure function must have the functional form [see Eq. (1.22)]

$$\mathcal{F}_1 \sim \Phi \left( x_{\text{Bj}} + \frac{k_T^2}{x_{\text{Bj}} M^2} \right) \theta \left( x_{\text{Bj}}(1 - x_{\text{Bj}}) M^2 - k_T^2 \right). \quad (141)$$

(A similar analysis is given for polarized PDFs in Ref. [54].) Here, the  $\tilde{k}^2 = 0$  condition constrains the behavior of the PDF to all orders in  $x_{\text{Bj}} m_s^2/Q^2$ ,  $m_q^2/Q^2$  and  $k_T^2/Q^2$ . Furthermore, fixing  $\tilde{k}^2 = 0$  removes the ultraviolet divergences in the integral over  $k_T$  that ultimately gives rise to the logarithmic behavior characteristic of the DGLAP evolution equations [46–48]. By contrast, factorization derivations impose no constraints on typical sizes for  $\tilde{k}^2$  (recall Sec. 4.3) inside a PDF, instead leaving it to be determined by the intrinsic properties of the hadron.

The constraint  $\tilde{k}^2 = 0$  in Eq. (141) is thus an extra dynamical assumption, and a rather restrictive one. This is illustrated, for example, by Fig. 12 and the discussions in Sec. 4.4.1. In field theory calculations of a PDF,  $k^2$  tends to vary smoothly over a broad range between 0 and  $O(-Q^2)$  (see Fig. 12), and indeed in an unregulated integration over  $k_T$ , the virtuality  $\tilde{k}^2$  diverges.

In practice, the  $\tilde{k}^2 = 0$  constraint is rather difficult to achieve in field theories and realistic models, and it precludes order-by-order derivations of factorization. This can be understood by inspecting Eq. (118) and noting the distortions to the  $O(\lambda^2)$  parton distribution that would be necessary to recover a form like Eq. (141).

Figures 11–13 emphasize that the structure functions are sensitive to the exact value of

$k^2$ , including  $k^2 \neq 0$ . At a minimum, the higher twist  $k^2 \neq 0$  contributions in Ref. [53] are needed for consistent power counting. For the above reasons, use of the term “purely kinematical” TMCs will be restricted to what is described in the context of Eqs. (138)–(140), namely, only the replacement  $x_{Bj} \rightarrow x_N$ . This observation motivated the choice of which TMC methodology is examined in Chapter 5. See that chapter for more details.

#### 4.4.5 Help from large $\ln(1 - x_{Bj})$ resummation

Beyond leading power in  $Q^2$ , the integration of the large transverse momentum in Eq. (132) actually takes the form

$$\begin{aligned} \int_{M_{\text{cut}}^2}^{k_{\text{Tmax}}^2} \frac{dk_{\text{T}}^2}{k_{\text{T}}^2} &\propto \ln \left[ \frac{Q^2}{M_{\text{cut}}^2} \left( \frac{1 - x_{Bj}}{x_{Bj}} + \frac{(M^2 - 2m_q^2 - 2m_s^2)}{Q^2} + O\left(\frac{m^4}{Q^4} \frac{x_{Bj}}{1 - x_{Bj}}\right) \right) \right] \\ &= \ln \frac{Q^2}{M_{\text{cut}}^2} + \ln \left( \frac{1 - x_{Bj}}{x_{Bj}} \right) + \frac{x_{Bj} (M^2 - 2m_q^2 - 2m_s^2)}{(1 - x_{Bj})Q^2} + O\left(\frac{m^4}{Q^4} \frac{x_{Bj}^2}{(1 - x_{Bj})^2}\right). \end{aligned} \quad (142)$$

In the region of  $x_{Bj}$  where

$$\frac{x_{Bj} m^2}{Q^2} \ll 1 - x_{Bj} \ll 1, \quad (143)$$

the only non-negligible contributions in Eq. (142) are the terms  $\ln Q^2$  and  $\ln(1 - x_{Bj})$ . The logarithms of  $(1 - x_{Bj})$  appear at all orders in perturbation theory in collinear factorization, and much effort has been devoted to methods for resumming them in collinear perturbative QCD. It is important to remember, however, that the usefulness of such methods relies on the condition in Eq. (143) being fulfilled. If hadron mass corrections are large, for instance when  $m^2/Q^2 \sim \alpha_s$ , the expansion Eq. (142) may no longer be a useful approximation. In the literal limit  $x_{Bj} \rightarrow 1$ , it is impossible to fulfill Eq. (143).

There is of course no obvious sharp boundary between regions where perturbative  $\ln(1 - x_{Bj})$  terms dominate and regions where  $x_{Bj}$  is so large that power corrections dominate or the

power expansion breaks down entirely and Eq. (143) fails. In principle, both the logarithmic and power correction effects are intertwined because they stem from the same underlying physical origin; the available phase space for final states becomes constricted as  $x_{Bj} \rightarrow 1$ , and the distinction between logarithmic effects and subleading power corrections becomes less clear-cut. For example, it is equally valid to express the large logarithmic effects in Eq. (142) as  $\ln(1 - x_{Bj})$  or  $\ln(1 - x_N)$  simply by reorganizing power corrections accordingly. Thus, incorporating power corrections consistently in perturbative QCD may entail new techniques in addition to a merging of old ones.

An ideal formalism would smoothly connect a treatment that includes purely nonperturbative behavior at very large  $x_{Bj}$  with resummation in the limit that the condition in Eq. (143) holds. This would be analogous to what occurs with TMD factorization, where a resummation of  $\ln(q_T^2/Q^2)$  holds when  $m \ll q_T \ll Q$ , but nonperturbative intrinsic transverse momentum dependence contributes when  $q_T$  begins to approach  $m$ . It will be important to explore such effects in future work.

## CHAPTER 5

### TARGET MASS CORRECTIONS

Knowing the exact value of the correction term in the factorized expressions for inclusive DIS derived in Chapter 3 requires a much deeper understanding of complex QCD dynamics than what is treated by the usual factorization. However, there are certain standard approximations (see, *e.g.*, Ref. [55, p. 95]) contributing to the error in Eqs. 96 and 98 that deal only with the external kinematics of  $P$  and  $q$  and have nothing specifically to do with the dynamics of the deeply inelastic collision. These were discussed in Sec. 4.4.4 and are what will be meant by “purely kinematical” approximations. The most common of these is a target mass approximation in inclusive DIS: if the target is moving in light-cone variables with large “+” momentum and zero transverse momentum, then  $P^\mu = (P^+, M^2/2P^+, \mathbf{0}_T) \approx (P^+, 0, \mathbf{0}_T)$ . As will be discussed in detail below, the resulting errors are proportional to powers of  $x_{\text{Bj}}^2 M^2/Q^2$ , where  $M$  is the target nucleon mass.

By contrast, the derivation of factorization uses approximations on internal partonic constituents, whose exact properties depend on complex details of QCD dynamics. The resulting error terms are suppressed by powers of  $m^2/Q^2$ , where  $m$  here represents any of the scales associated with intrinsic dynamical properties of bound state partons, such as their virtualities. Since the factorization theorem is meant to describe the limiting behavior as  $1/Q^2 \rightarrow 0$ , the  $x_{\text{Bj}}^2 M^2/Q^2$  errors from the kinematical expansion are typically lumped with the dynamical  $m^2/Q^2$  errors. I will, however, refrain from identifying the  $O(x_{\text{Bj}}^2 M^2/Q^2)$  terms as a contribution to the  $O(m^2/Q^2)$  corrections in all discussions so as to emphasize the different origins of these two types of errors.

Of course, all mass scales are ultimately fixed by the QCD scale parameter  $\Lambda_{\text{QCD}}^2$ , so the internal scales associated with  $m^2$  should be understood to be proportional to  $M^2$ :  $m^2 = \eta M^2$ , with  $\eta$  being a dimensionless proportionality factor. So another way then to state the above is to consider expansions in powers of  $\eta M^2/Q^2$  separately from powers of  $M^2/Q^2$ . This is explained in more detail in Secs. 5.1 and 5.2.

At moderate  $Q$ , a natural question is whether all of the various types of contributions to the error term in Eqs. 96 and 98 are really so negligible and, if not, whether some improvement is possible. For instance, when  $Q \sim 1$  GeV and  $x_{Bj}$  is not especially small ( $x_{Bj} \sim 1$ ), the  $x_{Bj}^2 M^2/Q^2$  purely kinematical errors may no longer be negligible. Since they arise only from kinematical approximations, it is reasonable to ask if these purely kinematical errors can be removed with minimal or no modification to the basic correctness of the factorization derivation for the first term in Eqs. 96 and 98. In fact, as will be discussed in Sec. 5.2, the standard derivations do not actually require a massless target approximation. Setting the target mass to zero is an ancillary step, while keeping it nonzero leads naturally to Nachtmann scaling [34]. This was actually recognized some time ago by Aivazis, Olness and Tung (AOT) [20] in the context of heavy quark contributions in DIS.

Questions of interpretation remain, however. It must be established, for example, whether it is reasonable to expect that correction for kinematical mass errors will result in phenomenological improvements in applications of QCD factorization. That it should is not obvious since there is no reason *a priori* to assume one type of power correction is more important than another. The mass scales divided by  $Q^2$  that contribute errors to factorization originate from nonperturbative features of the target hadron, so the effectiveness of target mass improvements must be tied to specific features of individual targets. Questions concerning the relevance of target mass kinematics therefore cannot generally be disentangled from questions about hadron structure.

In this chapter I will argue that it is most natural to expect an improvement from the approach of AOT [20] if the structure of the target involves a hierarchy of nonperturbative scales. Keeping certain powers of  $1/Q^2$  while neglecting others makes sense only when there is a reasonably large variation in mass-squared factors in the numerators. Questions about the phenomenological usefulness of kinematical target mass corrections can then be reframed as questions about target structure. This is how I advocate addressing the issue of target mass kinematics more generally, as explained in more detail in Sec. 5.4. In Sec. 5.1

I introduce the massless target approximation, carefully defining projection operators and structure functions in the limit of small  $M^2/Q^2$ . The factorization of the DIS process into a hard scattering subprocess from massless and on-shell partons is outlined in Sec. 5.2, where I write down the explicit formulas for the structure functions in terms of partonic scattering amplitudes and nonperturbative PDFs. Sec. 5.3 discusses the other prescriptions for dealing with the effects of a nonzero target mass on kinematics that have been proposed in the literature. The relation between TMC improvement and nonperturbative scale hierarchy is discussed in Sec. 5.4. The work in this chapter was originally published in [56].

### 5.1 Massless Target Approximation (MTA)

Purely kinematical approximations are those which can be defined in the context of Eqs. (17)–(19); that is, by considering only overall external momentum and with no reference to hadrons’ constituents or other dynamical properties. Note in this discussion  $x_{\text{Bj}}$  will be stated as a function  $x_{\text{Bj}}(x_{\text{N}}, M^2/Q^2, Q^2)$ . While this may appear cumbersome initially, it will help make later approximation steps unambiguous. A kinematical approximation replaces  $P$  and  $q$ , and the *arguments* of the structure functions  $F_i(x_{\text{Bj}}(x_{\text{N}}, M^2/Q^2), Q^2)$ , by different, approximated quantities, *without* changing anything about the functions in Eq. (17) themselves.

Let me define the natural approximate target hadron four-momentum  $\tilde{P}$  in a frame where it is moving at relativistic speeds by setting the target mass to zero,

$$P \rightarrow \tilde{P} \equiv (P^+, 0, \mathbf{0}_T). \quad (144)$$

The massless target approximation (MTA) is the kinematical approximation defined by the replacement

$$P \cdot q \rightarrow \tilde{P} \cdot q,$$

wherever this occurs in Eq. (15). To set up the approximation, it is convenient to first switch

the structure function decomposition to a basis that uses  $\tilde{P}$  instead of  $P$ ,

$$W^{\mu\nu} = \left(-g^{\mu\nu} + \frac{q^\mu q^\nu}{q^2}\right) \tilde{F}_1(x_{\text{Bj}}(x_{\text{N}}, M^2/Q^2), Q^2) + \left(\tilde{P}^\mu - \frac{\tilde{P} \cdot q}{q^2} q^\mu\right) \left(\tilde{P}^\nu - \frac{\tilde{P} \cdot q}{q^2} q^\nu\right) \frac{\tilde{F}_2(x_{\text{Bj}}(x_{\text{N}}, M^2/Q^2), Q^2)}{\tilde{P} \cdot q}. \quad (145)$$

Here I have defined

$$\tilde{F}_i(x_{\text{Bj}}(x_{\text{N}}, M^2/Q^2), Q^2) \equiv \tilde{\text{P}}_i^{\mu\nu} W_{\mu\nu}, \quad [i = 1, 2] \quad (146)$$

with the corresponding tensors to project out the structure functions defined by

$$\tilde{\text{P}}_1^{\mu\nu} \equiv \text{P}_1^{\mu\nu}(x_{\text{N}}, Q, 0) = -\frac{1}{2} \left( g^{\mu\nu} - \frac{4x_{\text{N}}^2}{Q^2} \tilde{P}^\mu \tilde{P}^\nu \right), \quad (147\text{a})$$

$$\tilde{\text{P}}_2^{\mu\nu} \equiv \text{P}_2^{\mu\nu}(x_{\text{N}}, Q, 0) = -x_{\text{N}} \left( g^{\mu\nu} - \frac{12x_{\text{N}}^2}{Q^2} \tilde{P}^\mu \tilde{P}^\nu \right). \quad (147\text{b})$$

This is a more convenient basis for ultimately neglecting the minus component of  $P$ . Note that it is  $x_{\text{N}}$  that appears in the factors on the right side of Eqs. (147), and not  $x_{\text{Bj}}$ . To relate structure functions in the two bases, one can use

$$\left(\tilde{\text{P}}_i^{\mu\nu} W_{\mu\nu}\right)_{\text{Eq. (17)}} = \left(\tilde{\text{P}}_i^{\mu\nu} W_{\mu\nu}\right)_{\text{Eq. (145)}}. \quad (148)$$

Applying the projectors (147) gives

$$\tilde{F}_1(x_{\text{Bj}}(x_{\text{N}}, M^2/Q^2), Q^2) = F_1(x_{\text{Bj}}(x_{\text{N}}, M^2/Q^2), Q^2), \quad (149\text{a})$$

$$\tilde{F}_2(x_{\text{Bj}}(x_{\text{N}}, M^2/Q^2), Q^2) = \frac{(Q^2 + M^2 x_{\text{N}}^2)^2}{Q^2 (Q^2 - M^2 x_{\text{N}}^2)} F_2(x_{\text{Bj}}(x_{\text{N}}, M^2/Q^2), Q^2). \quad (149\text{b})$$

I stress that no approximation has been made in the discussion up to this point. The coefficients in front of the structure functions in Eqs. (149) are, in fact, the same as those in the literature that are referred to as “ $\xi$ -scaling” [20, 57–60]. The first step in the MTA is

the replacement of  $x_{\text{Bj}}(x_{\text{N}}, M^2/Q^2)$  by  $x_{\text{Bj}}(x_{\text{N}}, 0)$  in the structure functions in Eq. (145),

$$\begin{aligned} W^{\mu\nu} \xrightarrow{\text{MTA}} \widetilde{W}^{\mu\nu} &= \left( -g^{\mu\nu} + \frac{q^\mu q^\nu}{q^2} \right) \widetilde{F}_1(x_{\text{Bj}}(x_{\text{N}}, 0), Q^2) \\ &+ \left( \widetilde{P}^\mu - \frac{\widetilde{P} \cdot q}{q^2} q^\mu \right) \left( \widetilde{P}^\nu - \frac{\widetilde{P} \cdot q}{q^2} q^\nu \right) \frac{\widetilde{F}_2(x_{\text{Bj}}(x_{\text{N}}, 0), Q^2)}{\widetilde{P} \cdot q}, \end{aligned} \quad (150)$$

where  $\widetilde{W}^{\mu\nu}$  is the approximate hadronic tensor. In this approximation, Eq. (10) gives

$$x_{\text{Bj}}(x_{\text{N}}, 0) = x_{\text{N}}, \quad (151)$$

so that  $x_{\text{Bj}}$  and  $x_{\text{N}}$  are interchangeable in the MTA.<sup>1</sup>

The above discussion suggests a definition for the target mass approximated structure functions  $\mathcal{F}_i$ ,

$$\mathcal{F}_i(x_{\text{Bj}}, Q^2) \equiv \widetilde{F}_i(x_{\text{Bj}}(x_{\text{N}}, 0), Q^2), \quad (152)$$

where the script notation is a shorthand that means  $x_{\text{Bj}}(x_{\text{N}}, M^2/Q^2)$  is understood to be everywhere replaced by  $x_{\text{Bj}}(x_{\text{N}}, 0)$ , so that kinematical dependence on the ratio  $M^2/Q^2$  is neglected. Part of the MTA is to approximate structure functions defined in the “tilde” [Eq. (145)] and “non-tilde” [Eq. (17)] bases as being the same. From Eqs. (149), this also introduces only an  $O(M^2/Q^2)$  error. Expanding the structure functions in powers of  $M^2/Q^2$  gives a concise expression of the MTA,

$$\begin{aligned} F_i(x_{\text{Bj}}(x_{\text{N}}, M^2/Q^2), Q^2) &= \widetilde{F}_i(x_{\text{Bj}}(x_{\text{N}}, M^2/Q^2), Q^2) + O\left(\frac{x_{\text{Bj}}^2 M^2}{Q^2}\right) \\ &= \widetilde{F}_i(x_{\text{Bj}}(x_{\text{N}}, 0), Q^2) + O\left(\frac{x_{\text{Bj}}^2 M^2}{Q^2}\right) \\ &= \mathcal{F}_i(x_{\text{Bj}}, Q^2) + O\left(\frac{x_{\text{Bj}}^2 M^2}{Q^2}\right), \end{aligned} \quad (153)$$

---

<sup>1</sup>Note that an alternative way to project the  $\widetilde{F}_i$  structure functions in both Eqs. (145) and (150) is to replace the explicit  $q$  vectors by  $q \rightarrow \tilde{q} \equiv (-x_{\text{Bj}}P^+, Q^2/(2x_{\text{Bj}}P^+), \mathbf{0}_T)$  and use  $x_{\text{Bj}}(x_{\text{N}}, 0)$  in Eqs. (147) instead of  $x_{\text{Bj}}(x_{\text{N}}, M^2/Q^2)$ . I do not do this here since I wish to regard the  $q$  vector as exact.

where the approximation is to drop all the  $x_{Bj}^2 M^2/Q^2$  errors. In other words, assuming an exact hadronic tensor in Eq. (15), the MTA [Eqs. (146)–(150)] is equivalent to a set of natural argument replacements that are reasonable when  $Q$  is very large or  $x_{Bj}$  is very small. This approximation is usually made implicitly in discussions of high energy scattering in the literature [55]; here I have made it very explicit so that it will be straightforward to reverse it. Each step in Eq. (153) can be traced back to the unapproximated hadronic tensor and structure functions. Operationally, it is implemented by the replacement in Eq. (150).

This completes the general discussion of the exact and target mass approximated structure functions, based on considerations of external kinematics alone. In the remainder of the chapter I will specialize the discussion to the role of the target mass in collinear factorization.

## 5.2 The MTA and Collinear Factorization

This section discusses how the MTA of the last section, combined with the standard factorization steps discussed in Chapter 3, leads to the well-known collinear factorization theorem of Eqs. 96 and 98. Again, I will present the steps in greater detail than is common in the literature, which will help later to unravel the source of purely kinematical mass sensitivity.

Before any factorization approximations are made, the exact parton momentum  $k$  can in general have both a virtuality and transverse momentum,

$$k = \left( \xi P^+, \frac{k^2 + k_T^2}{2\xi P^+}, \mathbf{k}_T \right). \quad (154)$$

The steps to obtain factorization approximate certain internal lines by exactly light-like ones. In particular, all lines entering and exiting the hard partonic scattering subprocess in Fig. 14 are taken to be massless and on-shell, so that in Eq. (154) both  $|k^2|$  and  $k_T^2$  can be taken to be  $\sim O(m^2) \ll Q^2$  and hence dropped. The approximated parton momentum,  $\hat{k}$ , is then

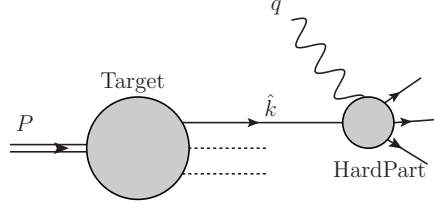


Figure 14: Figure taken from [56]. Illustration of DIS from a composite target ( $P$ ) in collinear factorization, with hard scattering of a virtual photon ( $q$ ) from an on-shell, massless parton ( $\hat{k}$ ).

parallel to the hadron momentum,

$$\hat{k} = (\xi P^+, 0, \mathbf{0}_T) , \quad (155)$$

where  $\xi = \hat{k}^+/P^+$  is the fraction of the target momentum carried by the struck parton. These steps for approximating the partonic momenta are justified in the standard derivations of collinear factorization, as discussed in Chapter 3. The factorization approximations make no reference to the target mass, so none of the approximations of the previous section are necessary to move forward with a factorization derivation.

The structure tensor for the target parton in the factorized subprocess has a form similar to that of Eq. (17), but with  $P^\mu$  replaced by  $\hat{k}^\mu$ ,

$$\begin{aligned} \widehat{W}^{\mu\nu}(\hat{k}, q) = & \left( -g^{\mu\nu} + \frac{q^\mu q^\nu}{q^2} \right) \widehat{F}_1(\hat{x}_{\text{Bj}}(\hat{x}_{\text{N}}, \hat{k}^2/Q^2), Q^2) \\ & + \left( \hat{k}^\mu - \frac{\hat{k} \cdot q}{q^2} q^\mu \right) \left( \hat{k}^\nu - \frac{\hat{k} \cdot q}{q^2} q^\nu \right) \frac{\widehat{F}_2(\hat{x}_{\text{Bj}}(\hat{x}_{\text{N}}, \hat{k}^2/Q^2), Q^2)}{\hat{k} \cdot q} , \end{aligned} \quad (156)$$

where  $\widehat{F}_i$  are the corresponding structure functions for the parton. In analogy with the scaling variables for the hadron, here  $\hat{x}_{\text{N}}$  is the partonic version of the Nachtmann variable

$x_N$ , as the natural generalization of  $x_N = -q^+/P^+$ ,

$$\hat{x}_N = -\frac{q^+}{\hat{k}^+} = \frac{2\hat{x}_{Bj}}{1 + \sqrt{1 + 4\hat{x}_{Bj}^2 \hat{k}^2/Q^2}} = \frac{x_N}{\xi}, \quad (157)$$

and  $\hat{x}_{Bj}$  is the obvious generalization of  $x_{Bj} = Q^2/2P \cdot q$ ,

$$\hat{x}_{Bj} \equiv \frac{Q^2}{2\hat{k} \cdot q} = \frac{Q^2}{2\hat{k}^+ q^-} = \frac{x_N}{\xi}. \quad (158)$$

Since for massless partons  $\hat{k}^2 = 0$ , the MTA is automatic for the partonic structure tensor, and  $\hat{x}_N = \hat{x}_{Bj}$ . Using the notation of Eq. (152), but now for the partonic target, the partonic structure tensor can be written as

$$\begin{aligned} \widehat{W}^{\mu\nu}(\hat{k}, q) &= \left( -g^{\mu\nu} + \frac{q^\mu q^\nu}{q^2} \right) \widehat{\mathcal{F}}_1(\hat{x}_{Bj}, Q^2) \\ &+ \left( \hat{k}^\mu - \frac{\hat{k} \cdot q}{q^2} q^\mu \right) \left( \hat{k}^\nu - \frac{\hat{k} \cdot q}{q^2} q^\nu \right) \frac{\widehat{\mathcal{F}}_2(\hat{x}_{Bj}, Q^2)}{\hat{k} \cdot q}, \end{aligned} \quad (159)$$

where  $\widehat{\mathcal{F}}_i$  are the partonic versions of the massless structure functions of Eq. (152). Applying the projectors in Eqs. (19) to Eq. (96) allows factorization to be written in terms of structure functions, still without the MTA,

$$F_1(x_{Bj}(x_N, M^2/Q^2), Q^2) = \int_{\xi_{\min}}^1 \frac{d\xi}{\xi} \widehat{\mathcal{F}}_1(\hat{x}_{Bj}(\xi), Q^2) f(\xi) + O(m^2/Q^2), \quad (160a)$$

$$F_2(x_{Bj}(x_N, M^2/Q^2), Q^2) = \frac{Q^2(Q^2 - M^2 x_N^2)}{(Q^2 + M^2 x_N^2)^2} \int_{\xi_{\min}}^1 d\xi \widehat{\mathcal{F}}_2(\hat{x}_{Bj}(\xi), Q^2) f(\xi) + O(m^2/Q^2), \quad (160b)$$

where from Eq. (158) one has  $\hat{x}_{Bj}(\xi) = x_N/\xi$ . For the lower limit of the  $\xi$  integration, the minimum  $\xi$  occurs when  $(\hat{k} + q)^2 = 0$ , which gives  $\xi_{\min} = x_N$ . Thus, without kinematical

target mass approximations, the factorized expressions for the structure functions are

$$\begin{aligned} F_1(x_{\text{Bj}}(x_{\text{N}}, M^2/Q^2), Q^2) &= \int_{x_{\text{N}}}^1 \frac{d\xi}{\xi} \widehat{\mathcal{F}}_1(x_{\text{N}}/\xi, Q^2) f(\xi) + O(m^2/Q^2) \\ &\equiv F_1^{\text{AOT}}(x_{\text{Bj}}(x_{\text{N}}, M^2/Q^2), Q^2) + O(m^2/Q^2), \end{aligned} \quad (161a)$$

$$\begin{aligned} F_2(x_{\text{Bj}}(x_{\text{N}}, M^2/Q^2), Q^2) &= \frac{Q^2(Q^2 - M^2x_{\text{N}}^2)}{(Q^2 + M^2x_{\text{N}}^2)^2} \int_{x_{\text{N}}}^1 d\xi \widehat{\mathcal{F}}_2(x_{\text{N}}/\xi, Q^2) f(\xi) + O(m^2/Q^2) \\ &\equiv F_2^{\text{AOT}}(x_{\text{Bj}}(x_{\text{N}}, M^2/Q^2), Q^2) + O(m^2/Q^2). \end{aligned} \quad (161b)$$

The errors here arise entirely from assumptions about the smallness of intrinsic parton scales; there are no  $x_{\text{Bj}}^2 M^2/Q^2$  types of errors since no MTA has been made. The second lines of Eqs. (161a) and (161b) define the ‘‘AOT structure functions’’,  $F_i^{\text{AOT}}$ , as the factorized structure functions with exact external kinematics [20], and this prescription for taking target masses into account will be referred to as the AOT method. (Note that the notation in Eqs. (161) differs from that in Ref. [20], whose focus was more on the treatment of heavy quark effects rather than on kinematical errors.) If, in addition,  $x_{\text{N}}$  is expanded in powers of  $x_{\text{Bj}}^2 M^2/Q^2$ , then Eqs. (161) become

$$\begin{aligned} F_1(x_{\text{Bj}}(x_{\text{N}}, M^2/Q^2), Q^2) &= \mathcal{F}_1(x_{\text{Bj}}, Q^2) + O\left(\frac{x_{\text{Bj}}^2 M^2}{Q^2}\right) \\ &= \int_{x_{\text{Bj}}}^1 \frac{d\xi}{\xi} \widehat{\mathcal{F}}_1(x_{\text{Bj}}/\xi, Q^2) f(\xi) + O\left(\max\left[\frac{m^2}{Q^2}, \frac{x_{\text{Bj}}^2 M^2}{Q^2}\right]\right), \end{aligned} \quad (162a)$$

$$\begin{aligned} F_2(x_{\text{Bj}}(x_{\text{N}}, M^2/Q^2), Q^2) &= \mathcal{F}_2(x_{\text{Bj}}, Q^2) + O\left(\frac{x_{\text{Bj}}^2 M^2}{Q^2}\right) \\ &= \int_{x_{\text{Bj}}}^1 d\xi \widehat{\mathcal{F}}_2(x_{\text{Bj}}/\xi, Q^2) f(\xi) + O\left(\max\left[\frac{m^2}{Q^2}, \frac{x_{\text{Bj}}^2 M^2}{Q^2}\right]\right). \end{aligned} \quad (162b)$$

The expressions in Eqs. (161) are the most immediate results of a factorization derivation of the style of Ref. [35], and the factorized terms on the right-hand-side can be considered

nearly exact if the  $m^2/Q^2$  errors (*i.e.*, quantities like parton virtuality) are negligible. On the other hand, Eqs. (162) are the more usual way of presenting the final factorization result, which arises from applying the MTA of Sec. 5.1 to the factorized expressions in Eqs. (161). The resulting errors are suppressed by  $x_{\text{Bj}}^2 M^2/Q^2$  and are here seen to be of purely kinematical origin. The approximation of dropping all power corrections in Eq. (162) and keeping only the first term on the right will be referred to as the “factorized massless target approximation” (FMTA), since it just combines standard factorization with the MTA. If one wishes to keep kinematical target mass effects, one simply maintains Eqs. (161).

In order to make the various approximations very explicit, the discussion in the last two sections of the basic theoretical set up has been much more detailed than what is usually found in the literature. This has required the introduction of a number of new notations for structure functions, which is useful to briefly summarize here:

- Hadronic structure functions, which are represented by the Roman font  $F_i$ , are functions of the independent variables  $x_{\text{Bj}}$  and  $Q^2$ ; however, since it is ultimately convenient to express them in terms of  $x_{\text{N}}$  and  $Q^2$ ,  $x_{\text{Bj}}$  is written explicitly as a function of  $x_{\text{N}}$  and  $M^2/Q^2$ .
- The hadronic tensor can be re-expressed in a different basis of Lorentz vectors, by using  $\tilde{P}^\mu$  rather than  $P^\mu$  to define the corresponding structure functions  $\tilde{F}_i$  in the massless basis, which is distinguished by the tilde [“ $\sim$ ”] symbol.
- When this is combined with the approximation  $x_{\text{Bj}}(x_{\text{N}}, M^2/Q^2) \rightarrow x_{\text{Bj}}(x_{\text{N}}, 0)$  one obtains the  $\tilde{F}_i(x_{\text{Bj}}(x_{\text{N}}, 0), Q^2)$  structure functions evaluated as in Eq. (150).
- The script notation for the structure functions  $\mathcal{F}_i$  is an abbreviation for the special case when  $M^2/Q^2$  is set to zero in  $x_{\text{Bj}}(x_{\text{N}}, M^2/Q^2)$ , as in Eq. (152).
- A hat [“ $\hat{\phantom{x}}$ ”] on a structure function denotes a massless and on-shell partonic target. Note that structure functions in Roman font with a hat ( $\hat{F}_i$ ) and in script font with

a hat ( $\widehat{\mathcal{F}}_i$ ) are identical, since  $\widehat{k}^2 = 0$ . Also, partonic structure functions are identical with (the partonic analogues of) either the  $W^{\mu\nu}$  [Eq. (17)] or  $\widetilde{W}^{\mu\nu}$  [Eq. (150)] bases, since the target parton in the hard part is always massless and on-shell.

For many subsequent practical applications some of these notations will be redundant; however, since they make the different layers of conventions and approximations very explicit, they will be useful for the present purposes.

To conclude this section, let me also summarize the key observations:

- (1) There are two independent types of approximations. One is the purely kinematical approximation described in Sec. 5.1, with errors suppressed by powers of  $x_{\text{Bj}}^2 M^2/Q^2$ . It is independent of whatever theoretical techniques might be used to actually calculate the structure functions. The second approximation is the factorization theorem in Eq. (96), with errors suppressed by powers of  $m^2/Q^2$ , where  $m^2$  is a typical scale associated with intrinsic dynamical properties of partons, such as their virtualities.
- (2) The MTA is not necessary for deriving collinear factorization. The relation  $\hat{x}_{\text{Bj}} = x_{\text{N}}/\xi$  in Eq. (158) is usually automatically approximated to  $x_{\text{Bj}}/\xi$ , but this is not needed. One may simply stop at Eqs. (161) and view the MTA application that leads to Eqs. (162) as ancillary.
- (3) The standard factorization derivation, as embodied in the AOT method, automatically gives  $x_{\text{N}}$  instead of  $x_{\text{Bj}}$  as the natural scaling variable for the structure functions (neglecting logarithmic  $Q$  dependence from higher orders in  $\alpha_s$ ).

### 5.3 Contrast with other TMC methods

Throughout this chapter I have adopted what could be viewed as the most natural meaning of a “purely kinematical correction”; namely, a correction that is totally independent of any assumptions pertaining to the dynamics within the target. The MTA from Sec. 5.1 accounts for all such approximations that one encounters in the context of standard collinear

factorization in DIS. The purely kinematical target mass correction is therefore uniquely of the form derived by AOT [20] (see Sec. 5.2), since this is merely the combination of the MTA and standard factorization, which is independent of target mass kinematics. Any other corrections must involve at least some set of additional assumptions about parton dynamics.

In the literature there exist a number of other prescriptions that are sometimes described as “purely kinematical” target mass corrections, but which in various ways differ from the AOT approach. Probably the best known of these is the treatment by Georgi and Politzer [43] based on the operator product expansion (OPE). (For extensions to the polarized case see Refs. [61–64].) Here the expressions for target mass corrected structure functions contain extra terms involving integrals of structure functions, which arise from additional constraints or assumptions that are beyond the purely kinematical corrections implicit in the AOT approach. As discussed by Ellis, Furmanski and Petronzio [53], and more recently by D’Alesio, Leader and Murgia [54], the origin of the additional integral factors is the constraint that the struck partons inside the target correlation function should be *exactly* massless and on-shell, for all longitudinal momenta and for all transverse momenta. Absent some exotic dynamical mechanisms within the target, this appears to be a relatively strong assumption, which in itself is not a necessary one for the standard derivation of collinear factorization.

Another way to understand the difference between the AOT approach and the OPE-based prescription is to note that in the latter the kinematical TMCs that are kept are only those that are relevant for a leading twist treatment, while kinematical corrections associated with higher twists are neglected. This type of assessment of  $O(m^2/Q^2)$ -type errors runs the risk of entangling the  $O(x_{Bj}^2 M^2/Q^2)$  target mass corrections with those from other sources. By refraining from introducing  $O(x_{Bj}^2 M^2/Q^2)$ -type errors from the outset, the direct method used by AOT has the advantage of including all kinematical target mass effects regardless of twist. It is worth emphasizing here that modern derivations of factorization *do not* need to use the OPE, but rather can be formulated as direct, arbitrary-order expansions in powers

of  $1/Q^2$  [35]. An added benefit of the direct method, which can be argued to be the more rigorous one, is that it does not *a priori* need to entail an MTA.

Still other TMC formalisms have been proposed that also differ from, or go beyond, AOT [53, 59]. For example, the Accardi-Qiu prescription [59] uses collinear factorization together with the dynamical assumptions that well-defined target and jet directions exist at rather low  $Q^2$  [65, 66] and that the initial state baryon number flows only along one such direction [67]. This relies on a very literal matching between virtual partonic states and a particular final state distribution of hadrons, which goes beyond the standard factorization paradigm [35, 68] but regulates the behavior near the kinematical threshold at  $x_{Bj} = 1$ .

The direct factorization approach can also help to contextualize the so-called “threshold problem” [43], which is the observation that the structure function for nonzero target mass in the OPE derivation has support at  $x_{Bj} = 1$  (where kinematically only elastic scattering should contribute) and can be nonzero in the unphysical region  $x_{Bj} > 1$  (up to  $x_N = 1$ ) [69]. This has led to various proposals for modifying the target mass corrected structure functions such that they have support only in the physical region [54, 69–73]. The solution to the “threshold problem” from the factorization perspective is simply that the conditions for which QCD factorization itself is valid break down as  $x_{Bj} \rightarrow 1$ . While the structure functions are defined through Eq. (18) for all  $x_{Bj} \leq 1$ , and the parton distribution  $f(\xi)$  exists for all parton momentum fractions  $\xi \in [0, 1]$ , the factorization formulas in Eqs. (96) and (161) relating the two receive increasingly large corrections at large  $x_{Bj}$  that render the perturbative expansion in powers of both  $\alpha_s$  and  $1/Q^2$  no longer a useful one. Improvements beyond this require more sophisticated methods for treating the large- $x_{Bj}$  region than what is available in the standard factorization treatment.

#### 5.4 When are Target Mass Kinematics Relevant?

The most straightforward and correct approach to computing the inclusive DIS structure functions is to simply avoid introducing unnecessary kinematical errors by choosing to keep

target momentum exact and applying the AOT expressions for factorization in Eqs. (161). A question of interpretation remains, however; without special knowledge of the target structure there is no reason *a priori* to expect the powers of  $x_{\text{Bj}}^2 M^2/Q^2$  from purely kinematical approximations to be any more important than other power-suppressed corrections.

#### 5.4.1 Scattering from subsystems

To interpret an observed phenomenological improvement obtained by using the AOT method instead of the FMTA, consider several generic scenarios for scattering from an extended target that could reveal a nontrivial relation between target mass effects and general properties of hadron structure. Consider, for instance, that if the target is a composite object (the precise nature of which need not be specified at this stage), then the sum of scattering amplitudes may be described as occurring off subsystems of the target, as depicted in Fig. 15. I leave the nature of the dynamics completely unspecified at this stage and only assume that diagrammatic arguments apply generally. To be completely general, I also allow for the possibility that the lower (nonperturbative) blob is empty so that scattering can occur off the entire target as a whole.

To be quantitative, I define the generic subsystem to have a momentum before the collision parametrized by the four-vector

$$p = \left( XP^+, \frac{m_{\text{T}}^2}{2XP^+}, \mathbf{p}_{\text{T}} \right), \quad (163)$$

where the squared transverse mass  $m_{\text{T}}^2 \equiv p^2 + p_{\text{T}}^2$  denotes the sum of the virtuality  $p^2$  (which could in principle be negative) and transverse momentum  $p_{\text{T}}^2$  of the subsystem, and  $X = p^+/P^+$  is the light-cone fraction of the target carried by the subsystem. The collision with the exchanged virtual photon produces another system of particles with invariant mass-squared

$$v^2 \equiv (p + q)^2. \quad (164)$$

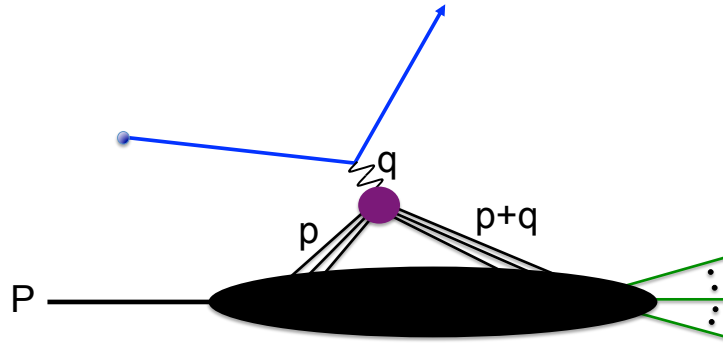


Figure 15: Figure taken from [56]. DIS from a subsystem ( $p$ ) of a composite target ( $P$ ). The solid lines connecting to the virtual photon ( $q$ ) through the upper blob can be any constituents of the target.

Such a system need not be physical and could be off-shell; for example, it could be a part of a hadronizing string. Without loss of generality, I may describe the total lepton scattering amplitude for the whole target  $\mathcal{A}^{\text{tot}}(P, q, l')$ , which in general depends on three variables (chosen here to be  $P$ ,  $q$  and  $l'$ ), in terms of the amplitude for scattering off the subsystem,

$$\mathcal{A}^p(p, q, l').$$

To connect to the total amplitude  $\mathcal{A}^{\text{tot}}$ , the subsystem amplitude needs to be integrated over all components of  $p$ , weighted by a function that characterizes the four-momentum distribution of the subsystem in the overall target.

To avoid confusion in what follows below, it is important not to view the diagram in Fig. 15 as the sort of “region” diagram common in factorization derivations [35], but rather as a topological representation in which the blobs are not necessarily characterized by any particular (small or large) momentum. The blobs simply denote an arbitrary subgraph assignment for some graphical contribution to the amplitude; some lines are routed through the (upper) photon–subsystem part of the graph, while others are diverted through the

(lower) part of the graph connected to the target.

Such organization does not achieve much of interest until I pose questions about possible relationships between the total target and subsystem momenta,  $P$  and  $p$ . If there is an assignment in Fig. 15 such that  $p_{\text{T}}^2, m_{\text{T}}^2 \ll Q^2$  for typical values of  $p_{\text{T}}^2$  and  $m_{\text{T}}^2$ , then up to power-suppressed errors the amplitude for scattering from the subsystem becomes a function of  $X$  only,

$$\mathcal{A}^p(p, q, l') = \mathcal{A}^p(X, q, l') + O\left(\max\left[\frac{p_{\text{T}}^2}{Q^2}, \frac{m_{\text{T}}^2}{Q^2}\right]\right). \quad (165)$$

The entire factorization derivation can then be performed for the sub-amplitude  $\mathcal{A}^p(X, q, l')$  rather than for the total amplitude  $\mathcal{A}^{\text{tot}}(P, q, l')$ .

In general the invariant mass  $v^2$  varies between small values ( $\approx 0$ ) and large values (of order  $Q^2$  or larger). In the standard QCD factorization paradigm, large- $v^2$  behavior is describable by perturbative calculations. One can therefore define an approximate invariant mass squared  $\tilde{v}^2$  of the final state subsystem which is calculated by approximate methods that deal with values of  $v^2/Q^2 = O(1)$ ,

$$v^2 \equiv \tilde{v}^2 + \delta v^2, \quad (166)$$

where  $\delta v^2$  is the correction needed to recover the exact  $v^2$  value. The approximate invariant mass squared  $\tilde{v}^2$  may vary from zero to  $O(Q^2)$ , while  $\delta v^2$  is of the order of a typical small scale comparable to  $p_{\text{T}}^2$  and  $m_{\text{T}}^2$ . Expanding  $X$  in terms of these variables, one can write

$$X = x_{\text{N}} \left\{ 1 + \frac{\tilde{v}^2}{Q^2} + \frac{p_{\text{T}}^2 + \delta v^2}{Q^2} - \frac{m_{\text{T}}^2(p_{\text{T}}^2 + \tilde{v}^2 + \delta v^2)}{Q^4} + \dots \right\}, \quad (167a)$$

and, further expanding the Nachtmann variable  $x_{\text{N}}$ , the light-cone fraction becomes

$$X = x_{\text{Bj}} \left\{ 1 + \frac{\tilde{v}^2}{Q^2} + \frac{p_{\text{T}}^2 + \delta v^2 - x_{\text{Bj}}^2 M^2}{Q^2} - \frac{(m_{\text{T}}^2 + x_{\text{Bj}}^2 M^2)(p_{\text{T}}^2 + \tilde{v}^2 + \delta v^2) - 2x_{\text{Bj}}^4 M^4}{Q^4} + \dots \right\}. \quad (167b)$$

If the typical values of small mass scales associated with the interactions between subsystems ( $p_{\text{T}}^2$ ,  $m_{\text{T}}^2$  and  $\delta v^2$ ) are totally negligible, but  $x_{\text{Bj}}^2 M^2$  is comparatively large, then the expansion in Eq. (167a) is an improvement over the expansion in Eq. (167b). In other words, in the limit of large  $Q$ ,

$$X \approx x_{\text{N}} \left( 1 + \frac{\tilde{v}^2}{Q^2} \right) \quad (168a)$$

provides a better approximation than

$$X \approx x_{\text{Bj}} \left( 1 + \frac{\tilde{v}^2}{Q^2} \right). \quad (168b)$$

In both of these cases, the connection between  $X$  and external observables has lost any sensitivity to the details of interactions between subsystems. The only dependence on dynamics is through  $\tilde{v}^2$ , which is calculable in factorization and perturbation theory. Suggestively defining

$$\left( 1 + \frac{\tilde{v}^2}{Q^2} \right) \equiv \frac{1}{\xi}, \quad (169)$$

the subsystem amplitude in Eq. (165) can be written

$$\mathcal{A}^p(p, q, l') = \mathcal{A}^p(x_{\text{N}}/\xi, q, l') + O \left( \max \left[ \frac{p_{\text{T}}^2}{Q^2}, \frac{m_{\text{T}}^2}{Q^2} \right] \right) \quad (170a)$$

$$= \mathcal{A}^p(x_{\text{Bj}}/\xi, q, l') + O \left( \max \left[ \frac{p_{\text{T}}^2}{Q^2}, \frac{m_{\text{T}}^2}{Q^2}, \frac{x_{\text{Bj}}^2 M^2}{Q^2} \right] \right). \quad (170b)$$

If  $x_{\text{Bj}}^2 M^2 \sim Q^2$  but  $p_{\text{T}}^2, m_{\text{T}}^2, \delta v^2 \ll Q^2$ , then truncating the expansion in (170a) is valid while in (170b) it is not. If, however,  $x_{\text{Bj}}^2 M^2 \sim p_{\text{T}}^2, m_{\text{T}}^2, \delta v^2$ , then there is no reason to expect either expansion to be any better or worse than the other. The same statements apply to the overall cross section, since it is related to  $\mathcal{A}^p$  by taking the square modulus, summing over hadronic final states, and integrating over  $\mathbf{p}_{\text{T}}$  and  $m_{\text{T}}$  (whose typical values are restricted by the  $p_{\text{T}}^2, m_{\text{T}}^2 \ll Q^2$  assumption to be small and are thus decoupled from  $\mathcal{A}^p$ ).

The above discussion naturally leads me to the conclusion that, if  $x_{\text{Bj}}^2 M^2$  is large but subsystem scales are small, then the cross section reduces to a function of  $x_{\text{N}}/\xi$ , with the momentum fraction  $\xi$  calculable from methods that account for large  $\tilde{v}^2$  — all of which can be performed within standard factorization. The AOT set of expressions [Eqs. (161)] is just a specific realization of this within collinear factorization. Namely, the hard scattering subprocess is always a function of  $x_{\text{N}}$ , while large final state invariant masses in the hard part of the scattering amplitude are accounted for by using  $x_{\text{N}}/\xi$  in the subprocess, with  $\xi$  obtained as in Eqs. (168). In other words, if the typical  $|p^2|$  is small and  $p$  is collinear to  $P$ , then the steps for deriving factorization can be applied directly to  $|\mathcal{A}^p(p, q, l')|^2$  with  $p^2 = 0$  rather than to  $|\mathcal{A}^{\text{tot}}(P, q, l')|^2$ . The result is automatically the AOT factorization in Eqs. (161). Furthermore, since it accounts for large  $\tilde{v}^2$ , the AOT improvement applies to all orders in perturbation theory.

#### 5.4.2 TMC improvement and hierarchy of scales

Now one may ask what general characteristics of a composite target can give rise to a scenario where  $p_{\text{T}}^2, m_{\text{T}}^2 \ll x_{\text{Bj}}^2 M^2$ , which would justify the result in Eq. (170a) being an improvement over that in Eq. (170b). At one extreme, it cannot be the case of scattering from a single, isolated perturbative quark or gluon, as these can emit large amounts of collinear and soft radiation. Moreover, a perturbative quark has virtuality that ranges up to  $O(Q^2)$ .

A system of collinearly propagating quarks and gluons that are nearly massless and on-shell cannot be described purely in terms of short-distance, perturbative propagators. At the other extreme, the  $p_{\text{T}}^2, m_{\text{T}}^2 \ll x_{\text{Bj}}^2 M^2$  condition also cannot arise when all or most of the lines in Fig. 15 are routed through the upper part of the diagram, leaving the blob in the lower part of the diagram completely empty, which would correspond to  $m_{\text{T}} \sim M$ .

The only way, therefore, to consistently arrive at a scenario whereby  $p_{\text{T}}^2, m_{\text{T}}^2 \ll x_{\text{Bj}}^2 M^2$ , and thus Eq. (170a) (in terms of  $x_{\text{N}}$ ) be an improvement over Eq. (170b) (in terms of  $x_{\text{Bj}}$ ), is if the target consists of more than one separate, low-invariant mass (relative to  $x_{\text{Bj}}^2 M^2$ )

subsystem that can play the role of the lines entering the upper blob in Fig. 15. To avoid pushing  $|p^2|$  too high, the interactions between subsystems need to be reasonably weak. While the individual subsystems necessarily need to have a small typical invariant mass  $|p^2|$  relative to  $x_{\text{Bj}}^2 M^2$ , each subsystem can involve internal interactions that involve scales much larger than  $p_{\text{T}}^2, m_{\text{T}}^2, \delta v^2$ , but still much smaller than  $Q^2$ . Therefore, it is only the scales involved in the interactions *between* subsystems that need to be very small in order for the above argument for the usefulness of the AOT method to be valid.

The general conclusion is that any observed improvement in the theoretical description of scattering that comes from using Eq. (170a) instead of Eq. (170b) is suggestive of a hierarchy of “clustered” structures within the target, representing correlated subsystems of strongly interacting particles. I stress that I am totally agnostic about what those clusters might be; the observation is simply that, kinematically, some sort of clustering is preferred. Thus, an improvement in the phenomenological description using the AOT method can be interpreted as evidence that scattering occurs off a collection of weakly interacting subsystems (since  $p_{\text{T}}^2$ ,  $m_{\text{T}}^2$  and  $\delta v^2$  must be small relative to  $x_{\text{Bj}}^2 M^2$ ), while a failure to observe any improvement suggests a more complicated type of scattering. (Some of this also echoes earlier discussions of TMCs in DIS at low energies, such as in Ref. [74], see pg. 325, where the scale  $M_0$  there is analogous to the mass  $m$  used in the present work.) A subsystem can in general be any nonperturbative system, consisting of one or more interacting particles, whose internal interactions are stronger than interactions with other subsystems in the target. The subsystem could, for example, be colored or colorless; for the latter, notice that for a nucleon target the region of kinematics where the  $x_{\text{Bj}}^2 M^2 / Q^2$  corrections are important corresponds to the nucleon resonance region, and the subsystems might be a collection of hadrons, such as nucleons and pions. However, the exact nature of the target or its subsystems and their interactions is not relevant to this discussion.

The above argument is very general, since it only relies on the kinematics of scattering off subsystems in a target, and the assumption that scattering from the composite object can

be described in generally diagrammatic terms. In particular, it applies to arbitrary orders in perturbation theory. In fact, arriving at Eqs. (170) does not even require factorization or partonic degrees of freedom specifically. It only states that, if scattering occurs off weakly interacting light and nearly on-shell subsystems in a heavier target, then the cross section at a particular  $v^2$  becomes a function of  $x_N/\xi$ , where  $\xi$  is either 1 or is obtainable from large- $\tilde{v}^2$  methods.

An example of such a scale hierarchy could be nuclear targets, where the subsystems correspond to nucleons; the hierarchy arises because interactions between nucleons are much weaker than the typical interactions binding quarks and gluons inside the nucleons [75, 76]. Other examples may be nucleons coupled to soft pseudoscalar mesons through chiral dynamics, which can give rise to unique nonperturbative features in sea quarks in the proton [77–81]. A possible hierarchy with explicit color degrees of freedom could involve partons clustered into constituent quark-like subsystems [82, 83]. Conversely, an example of a target where one would *not* expect an improvement would be the case of a hadron target whose mass comes almost entirely from a single point-like quark, such as a heavy quark hadron. I stress again, however, that these arguments here do not rely on any assumptions about dynamics of the composite object or the nature of its subsystems, but only on the kinematical considerations associated with target mass improvement.

## CHAPTER 6

### TRANSVERSE MOMENTUM DEPENDENCE IN $e^+/e^-$ ANNIHILATION

The annihilation of lepton pairs into hadrons is one of a class of processes notable for being especially clean electromagnetic probes of elementary quark and gluon correlation functions like parton density and fragmentation functions (pdfs and ffs) [84]. Other such processes include inclusive and semi-inclusive deep inelastic scattering (DIS and SIDIS), and the Drell-Yan (DY) process. In combination they provide some of the strongest tests of QCD factorization. However, the exact type of correlation functions involved (e.g., transverse momentum dependent, collinear, etc) depends on the details of the process under consideration and the particular kinematical regime being accessed. It is important to confirm the applicability of each expected factorization for each region, not only at the largest accessible energies, but also in more moderate energy regimes, since the latter are especially useful for probing the non-perturbative details of partonic correlation functions like pdfs and ffs, and for probing the intrinsic partonic structure of hadrons generally [85, 86].

In the case of the inclusive lepton-antilepton annihilation into a dihadron pair, the type of partonic correlation functions accessed depends on the pair's specific kinematical configuration. In the back-to-back configuration, there is sensitivity to the intrinsic non-perturbative transverse momentum of each observed hadron relative to its parent parton. This is the regime of transverse momentum dependent (TMD) factorization, in which TMD ffs are the relevant correlation functions [35, 84, 87–89]. The TMD region has attracted especially strong interest in phenomenological work in recent decades for its potential to probe the intrinsic non-perturbative motion of partons [40, 41, 90–101] and, more recently, its potential to impact also high-energy measurements [94, 102–106]. See also Refs. [107–109] for additional discussions of motivations to study  $e^+e^-$  annihilation into back-to-back hadrons generally, and especially including studies of spin and polarization effects. If instead the hadrons are nearly collinear, they can be thought of as resulting from a single hadronizing parent parton. In that case, the correct formalism uses dihadron ffs [110–113], which are useful for extract-

ing the transversity pdf without the need for TMD factorization [114–116]. Finally, if the hadrons are neither aligned, nor back-to-back, but instead have a large invariant mass, then the relevant factorization is standard collinear factorization with collinear ffs [28, 117–121] which has played a significant role in recent years to explore flavor separation in collinear pdfs using SIDIS data [28, 117, 118].

Having a fully complete picture of partonic correlation functions and the roles they play in transversely differential cross sections generally requires an understanding of the boundaries between the kinematical regions where different types of factorization apply and the extent to which those regions overlap [122–125]. This chapter focuses on the last of the lepton-antilepton annihilation regions mentioned in the previous paragraph, wherein pure collinear factorization is expected to be adequate for describing the large deviations from the back-to-back orientation of the hadron pair. This is a natural starting point for mapping out the regions of the process generally, since it involves only well-established collinear factorization theorems and starts with tree-level perturbation theory calculations. It is also motivated by tension between measurements and collinear factorization that has already been seen in transversely differential SIDIS [21–24, 126–128] and DY [25]. That all these cases involve  $Q \lesssim 14$  GeV hints that the origin of the tension lies with the smaller hard scales. The lack of smooth transition in the intermediate transverse momentum region suggests a more complicated than expected role for non-perturbative transverse momentum in the description of the large transverse momentum tail when  $Q$  is not extremely large. I will elaborate on these issues further in the main text and comment on potential resolutions in the conclusion.

Of course, much work has been done calculating distributions for this and similar processes, especially in the construction and development of Monte Carlo event generators [26, 27, 129–134]. My specific interest, however, is in the extent to which the most direct applications of QCD factorization theorems, with ffs extracted from other processes, give reasonable behavior in the far from back-to-back region. Despite the simplicity of the leading order (LO) cross section, it has not, to my knowledge, been explicitly presented elsewhere or used in

a detailed examination of the transverse momentum dependence of inclusive hadron pairs at wide angle in ordinary collinear pQCD calculations and using standard fragmentation functions. One challenge to performing such a study is a dearth of unpolarized dihadron data with transverse momentum dependence for the exact process under consideration here. In the absence of data, an alternative way to assess the reasonableness of large transverse momentum calculations, and to estimate the point of transition to small transverse momentum, is to examine how accurately they match to small or medium transverse momentum calculations performed using TMD-based methods, for which many phenomenological results already exist (see e.g. Refs. [135–142] and references therein).

I follow this latter approach in the present chapter. Namely, using the lowest order (LO) calculation of the far from back-to-back cross section along with standard ff fits [121], and comparing with Gaussian-based (or similar) fits from, for example, Ref. [99], I am able to confirm that the two methods of calculation approach one another at intermediate transverse momentum in the very large  $Q$  limit, albeit rather slowly. At both smaller and larger  $Q$ , the comparison between TMD and collinear based calculations suggests a transition point of between about  $q_T/q_T^{\text{Max}} \approx .3$  and  $.2$ , where  $q_T^{\text{Max}}$  is the kinematical maximum of transverse momentum. However, at moderate  $Q$  of around 12 GeV, the shape of the TMD-based calculation deviates significantly from the collinear at intermediate transverse momentum, and numerically the disagreement at intermediate transverse momentum rises to a factor of several in most places, with the fixed order collinear calculation undershooting the TMD-based calculation. This is noteworthy given the similar mismatch with actual data that has been seen in Drell-Yan and SIDIS, already remarked upon above. Whether the solution to the difficulties at moderate transverse momentum lies with the collinear treatment or with the phenomenology of TMD functions remains to be seen. But all of these observations, I argue, provide enhanced motivation for experimental studies of dihadron pair production that probe the intermediate transition region of the transverse momentum dependence.

I have validated the very large  $Q$  and moderate transverse momentum calculation by

comparing with transverse momentum distributions generated with the default settings of PYTHIA 8 [26, 27]. I find reasonable agreement with the PYTHIA generated distributions when the center-of-mass energy  $Q$  is large ( $\sim 50$  GeV). This is perhaps not surprising given that fits of collinear fragmentation functions are also generally constrained by large  $Q$  measurements. Nevertheless, the specificity of the process makes it a non-trivial consistency validation. At lower  $Q$  ( $\lesssim 10$  GeV) there is much larger disagreement with the event generator data, and I comment briefly on the interpretation of this in the text.

The organization of sections is as follows. Section 6.1.1 explains the steps of the LO collinear calculation at large transverse momentum, in Section 6.1.2 I discuss its asymptotically small transverse momentum behavior, and in Section 6.1.3 I review the basics of the (non-)perturbative TMD calculation for small transverse momentum. I elaborate on the expectations for the validity of the collinear factorization calculation in Sec. 6.2, and in Sec. 6.3 I compare and contrast the results at moderate transverse momentum. The work in this chapter was originally published in [36].

## 6.1 Factorization at Large, Moderate and Small Transverse Momentum

See Section 2.2.2 for a review of the kinematics of hadron pair production in SIA. For the polarization independent case considered in this chapter, contracting the leptonic and hadronic tensors in Eq. (64) and integrating over  $\theta$  and  $\phi$  gives

$$\frac{d\sigma_{AB}}{dz_A dz_B dq_T} = \frac{\alpha_{\text{em}}^2 z_A z_B (Q^2 + q_T^2)^2 q_T}{12\pi Q^6} [2W_T + W_L]. \quad (171)$$

To calculate in perturbative QCD, the differential cross section in Eq. (171) needs to be factorized into a hard part and ffs, and different types of factorization are appropriate depending on the particular kinematical regime. Assuming  $z_{A,B}$  are large enough to ensure that hadrons originate from separately fragmenting quarks, the three kinematical regions of interest for semi-inclusive scattering are determined by the transverse momentum  $q_T$ . There

are three major regions: i.)  $q_T \sim Q$  so that  $q_T$  and  $Q$  are equally viable hard scales, ii.)  $m \ll q_T \ll Q$  so that small  $q_T$  approximations are useful but  $q_T$  is large enough that intrinsic non-perturbative effects are negligible and logarithmic enhancements are only a small correction, iii.)  $q_T \lesssim m$  and all aspects of a TMD-based treatment are needed, including non-perturbative intrinsic transverse momentum (see also Sec. 6.2). I will briefly summarize the calculation of each of these below.

### 6.1.1 The fixed $O(\alpha_s)$ cross section at large transverse momentum

The scenario under consideration is one in which the two observed hadrons are produced at wide angle (so that  $(p_A + p_B)^2 \sim Q^2$ ), but are far from back-to-back (so that  $q_T \sim Q$ ). This requires at least one extra gluon emission in the hard part. See Fig. 16 (A) for the general structure of Feynman graphs contributing at large  $q_T$  and for the momentum labeling conventions.

The basic statement of collinear factorization for the differential cross section is

$$E_A E_B \frac{d\sigma_{AB}}{d^3\mathbf{p}_A d^3\mathbf{p}_B} = \sum_{i,j} \int_{z_A}^1 d\zeta_A \int_{z_B}^1 d\zeta_B \left( E_A E_B \frac{d\hat{\sigma}_{ij}(\hat{z}_A, \hat{z}_B)}{d^3\mathbf{p}_A d^3\mathbf{p}_B} \right) d_{H_A/i}(\zeta_A) d_{H_B/j}(\zeta_B) \quad (172)$$

where the hat on the cross section in the integrand indicates that it is for the partonic subprocess  $l_1 + l_2 \rightarrow k_A + k_B + X$ .  $k_A$  and  $k_B$  will label the momenta of the partons that hadronize. The integrals are over the momentum fraction variables  $\zeta_A$  and  $\zeta_B$  that relate the hadron and parton momenta in Fig. 16:

$$k_A \equiv p_A / \zeta_A, \quad k_B \equiv p_B / \zeta_B. \quad (173)$$

The  $i, j$  sum is over the different possible flavors of parton that can hadronize,  $i, j \in \{u, d, g, \bar{u}, \dots\}$ . The number of active flavors depends on the scale. The  $d_{H_A/i}(\zeta_A)$  and  $d_{H_B/j}(\zeta_B)$  are the fragmentation functions for flavor  $i(j)$  partons to hadronize into hadrons

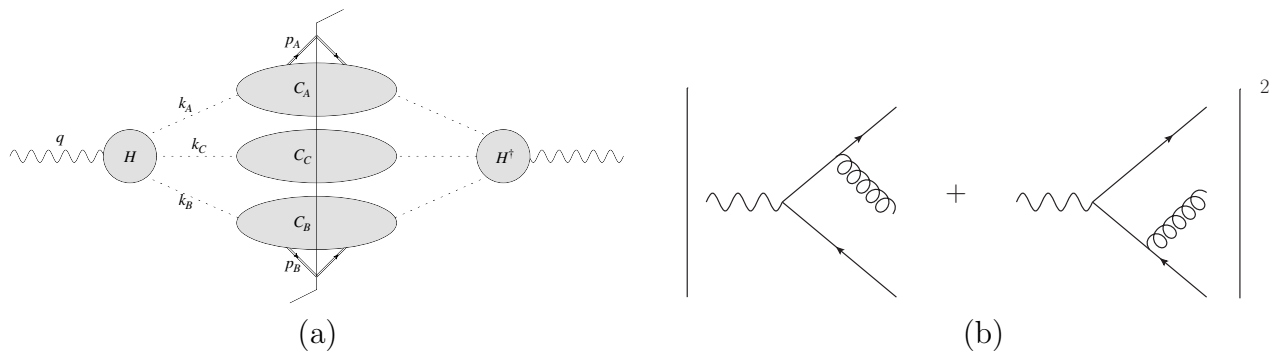


Figure 16: Figure taken from [36]. (a) The general diagrammatic structure contributing to Eq. (43) at large  $q_T$  and at LO in  $\alpha_s$ . The outgoing partonic lines are dotted to indicate that generally they can be of any type. In the region of interest for this chapter, their momenta deviate by wide angles from the back-to-back orientation for the dihadron pair.  $H$  represents the hard part of the interaction and the  $C_{A,B,C}$  are the collinear subgraphs [35]. (b) The  $O(\alpha_s)$  partonic contribution to the square-modulus amplitude in the factorization of (a).

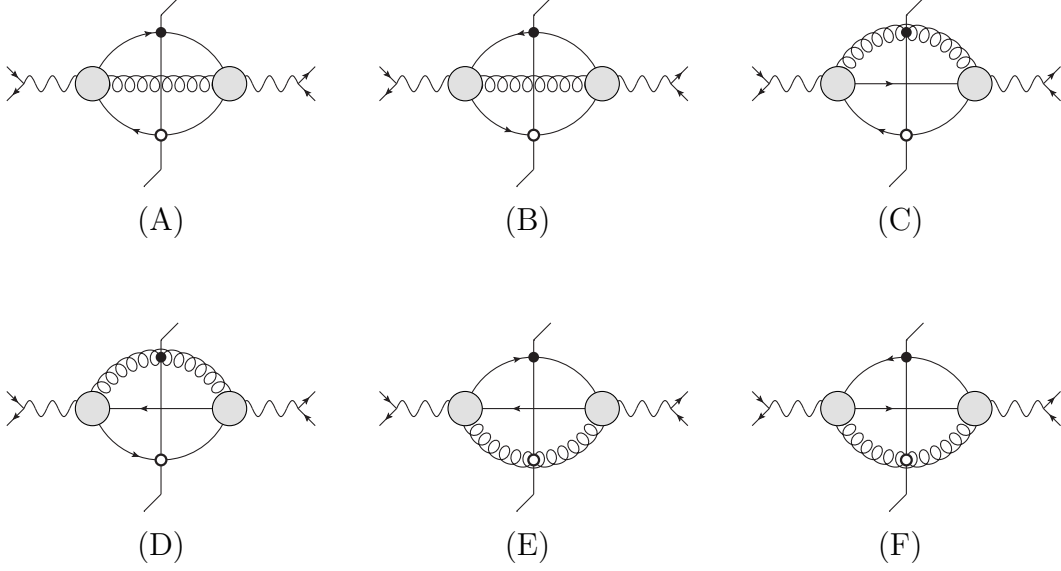


Figure 17: Figure taken from [36]. Partonic channels that contribute at order  $\alpha_s$ . Detailed explanation in Sec. 6.1.1.

of flavor  $A$  ( $B$ ). I use the standard abbreviations

$$\hat{z}_A = z_A/\zeta_A, \quad \hat{z}_B = z_B/\zeta_B, \quad (174)$$

which follow from Eq. (173) and the partonic analogue of the definitions in Eq. (47). The momentum of the parton whose hadronization is unobserved is  $k_C$  [59, 143, 144]. After factorization, the hard part involves the square-modulus of the  $H$  subgraph with massless, on-shell external partons. The graphs that contribute to this at lowest order are shown in Fig. 16(b).

It is useful to define a partonic version of the hadronic tensor,

$$\widehat{W}_{ij}^{\mu\nu} \equiv 4\pi^3 \sum_X \langle 0 | j_{ij}^\mu(0) | k_A, k_B, X \rangle \langle k_A, k_B, X | j_{ij}^\nu(0) | 0 \rangle \delta^{(4)}(q - k_A - k_B - p_X), \quad (175)$$

in which case

$$W^{\mu\nu} = \sum_{i,j} \int_{z_A}^1 \frac{d\zeta_A}{\zeta_A^2} \int_{z_B}^1 \frac{d\zeta_B}{\zeta_B^2} \widehat{W}_{ij}^{\mu\nu}(\hat{z}_A, \hat{z}_B) d_{H_A/i}(\zeta_A) d_{H_B/j}(\zeta_B). \quad (176)$$

Working with the hadronic tensor and with the extraction tensors like Eq. (59) conveniently automates the steps to obtain any arbitrary structure function. The differential cross section is

$$\frac{d\sigma_{AB}}{dz_A dz_B dq_T} = \sum_{i,j} \int_{z_A}^1 \frac{d\zeta_A}{\zeta_A} \int_{z_B}^1 \frac{d\zeta_B}{\zeta_B} \left( \frac{d\hat{\sigma}_{ij}(\hat{z}_A, \hat{z}_B)}{d\hat{z}_A d\hat{z}_B dq_T} \right) d_{H_A/i}(\zeta_A) d_{H_B/j}(\zeta_B), \quad (177)$$

and the partonic cross section can be expressed analogously to Eq. (171),

$$\frac{d\hat{\sigma}_{ij}}{d\hat{z}_A d\hat{z}_B dq_T} = \frac{\alpha_{\text{em}}^2 \hat{z}_A \hat{z}_B (Q^2 + q_T^2)^2 q_T}{12\pi Q^6} \left[ 2\widehat{W}_{T,ij} + \widehat{W}_{L,ij} \right], \quad (178)$$

where  $\widehat{W}_{T,ij}$  and  $\widehat{W}_{L,ij}$  are partonic structure functions calculated from the graphs in Fig. 16(b).

Given the expressions for the squared amplitudes in Fig. 16(b), the evaluation of the differential cross section becomes straightforward. Each possible combination of final state parton pairs in Fig. 16(b) can hadronize into  $H_A$  and  $H_B$  with fragmentation functions that depend on both the fragmenting parton and final state hadron. Six such channels contribute at leading order in  $\alpha_s$ , and these are organized diagrammatically in Fig. 17, with  $k_A$ ,  $k_B$  and  $k_C$  assigned to the quark, antiquark or gluon according to whether it hadronizes to  $H_A$ ,  $H_B$ , or is unobserved. A solid dot marks the parton that hadronizes into  $H_A$  (always  $k_A$  parton momentum) and the open dot marks the parton that hadronizes into  $H_B$  (always  $k_B$  momentum). There is an integral over all momentum of the remaining line ( $k_C$ ). Quark lines include all active quark flavors, and are shown separately from the anti-quark lines since they correspond to separate ffs. Notice that, unlike in the case of the  $q_T$ -integrated cross section for single hadron production, there is already sensitivity to the gluon fragmentation function at the lowest non-vanishing order.

The partonic structure functions  $\widehat{W}_{T,ij}$  and  $\widehat{W}_{L,ij}$  can be obtained by contracting the extraction tensors (Eq. (59)) with the partonic tensor  $\widehat{W}^{\mu\nu}$ . The relation between the partonic tensor and the squared amplitude of the hard part is:

$$\widehat{W}_{ij}^{\mu\nu} = 4\pi^3 \int \frac{d^3 \mathbf{k}_C}{2k_C^0 (2\pi)^3} \delta^{(4)}(q - k_A - k_B - k_C) |\widehat{\mathcal{M}}_{ij}^{2,\mu\nu}|^2 = \frac{1}{2} \delta_+(k_C^2) |\widehat{\mathcal{M}}_{ij}^{2,\mu\nu}|^2. \quad (179)$$

The resulting partonic cross sections are

$$\begin{aligned} \frac{d\hat{\sigma}_{q\bar{q}}}{d\hat{z}_A d\hat{z}_B dq_T} &= \frac{d\hat{\sigma}_{\bar{q}q}}{d\hat{z}_A d\hat{z}_B dq_T} \\ &= \frac{8\alpha_{\text{em}}^2 \alpha_s e_q^2 \hat{z}_A \hat{z}_B \delta(k_C^2) q_T (Q^2 + q_T^2)^3 (6Q^2 + 5q_T^2) (\hat{z}_A^2 + \hat{z}_B^2)}{9Q^6 (Q^2(\hat{z}_A - 1) + q_T^2 \hat{z}_A) (Q^2(\hat{z}_B - 1) + q_T^2 \hat{z}_B)} \end{aligned} \quad (180a)$$

$$\begin{aligned} \frac{d\hat{\sigma}_{qg}}{d\hat{z}_A d\hat{z}_B dq_T} &= \frac{d\hat{\sigma}_{\bar{q}g}}{d\hat{z}_A d\hat{z}_B dq_T} \\ &= -8\alpha_{\text{em}}^2 \alpha_s e_q^2 \hat{z}_A \hat{z}_B \delta(k_C^2) q_T (Q^2 + q_T^2)^2 \\ &\quad \times \left[ 2Q^4 (14 + 3\hat{z}_B^2 - 14\hat{z}_B + 2\hat{z}_A (3\hat{z}_A + 4\hat{z}_B - 7)) \right. \\ &\quad \left. + 5q_T^4 (\hat{z}_B^2 + 2\hat{z}_B \hat{z}_A + 2\hat{z}_A^2) + Q^2 q_T^2 (11\hat{z}_B^2 - 28\hat{z}_B + 2\hat{z}_A (11\hat{z}_A + 13\hat{z}_B - 14)) \right] \\ &\quad / \left( 9Q^6 (Q^2(\hat{z}_A - 1) + q_T^2 \hat{z}_A) (Q^2(\hat{z}_B + \hat{z}_A - 1) + q_T^2(\hat{z}_B + \hat{z}_A)) \right) \end{aligned} \quad (180b)$$

$$\begin{aligned} \frac{d\hat{\sigma}_{gq}}{d\hat{z}_A d\hat{z}_B dq_T} &= \frac{d\hat{\sigma}_{g\bar{q}}}{d\hat{z}_A d\hat{z}_B dq_T} \\ &= -8\alpha_{\text{em}}^2 \alpha_s e_q^2 \hat{z}_A \hat{z}_B \delta(k_C^2) q_T (Q^2 + q_T^2)^2 \\ &\quad \times \left[ 2Q^4 (14 + 3\hat{z}_A^2 - 14\hat{z}_A + 2\hat{z}_B (3\hat{z}_B + 4\hat{z}_A - 7)) \right. \\ &\quad \left. + 5q_T^4 (\hat{z}_A^2 + 2\hat{z}_A \hat{z}_B + 2\hat{z}_B^2) + Q^2 q_T^2 (11\hat{z}_A^2 - 28\hat{z}_A + 2\hat{z}_B (11\hat{z}_B + 13\hat{z}_A - 14)) \right] \\ &\quad / \left( 9Q^6 (Q^2(\hat{z}_B - 1) + q_T^2 \hat{z}_B) (Q^2(\hat{z}_A + \hat{z}_B - 1) + q_T^2(\hat{z}_A + \hat{z}_B)) \right) \end{aligned} \quad (180c)$$

### 6.1.2 The asymptotic $\frac{q_T^2}{Q^2} \rightarrow 0$ limit

The small  $q_T^2/Q^2$  limit of Eq. (177) involves considerable simplifications analogous to those obtained in TMD factorization, but applied to fixed order massless partonic graphs. It is

potentially a useful simplification, therefore, in situations where  $q_T^2$  is small enough that a  $q_T^2/Q^2$  expansion applies, but still large enough that fixed order perturbative calculations are reasonable approximations. As will be shown in later sections, it is also useful for estimating the borders of the regions where small  $q_T^2/Q^2$  approximations are appropriate.

The asymptotic term is obtainable by directly expanding the fixed order calculation in powers of small  $q_T/Q$ , with a careful treatment of the soft gluon region in the integrals over  $\zeta_A$  and  $\zeta_B$ . The steps are similar to those in SIDIS, and I refer to Ref. [145] for a useful discussion of them. When performed for the  $e^+e^-$  annihilation case under consideration here, the result is

$$\begin{aligned}
\frac{d\sigma_{AB}^{ASY}}{dz_A dz_B dq_T} &= \frac{4\alpha_{em}^2 \alpha_s}{Q^2 q_T} \sum_q e_q^2 \\
&\times \left\{ 2C_F \left[ \ln \left( \frac{Q^2}{q_T^2} \right) - \frac{3}{2} \right] (d_{H_A/q}(z_A) d_{H_B/\bar{q}}(z_B) + d_{H_A/\bar{q}}(z_A) d_{H_B/q}(z_B)) \right. \\
&+ d_{H_A/q}(z_A) [(P_{\bar{q}\bar{q}} \otimes d_{H_B/\bar{q}})(z_B) + (P_{g\bar{q}} \otimes d_{H_B/g})(z_B)] \\
&+ d_{H_A/\bar{q}}(z_A) [(P_{qq} \otimes d_{H_B/q})(z_B) + (P_{gq} \otimes d_{H_B/g})(z_B)] \\
&+ d_{H_B/q}(z_B) [(P_{\bar{q}\bar{q}} \otimes d_{H_A/\bar{q}})(z_A) + (P_{g\bar{q}} \otimes d_{H_A/g})(z_A)] \\
&\left. + d_{H_B/\bar{q}}(z_B) [(P_{qq} \otimes d_{H_A/q})(z_A) + (P_{gq} \otimes d_{H_A/g})(z_A)] \right\}, \tag{181}
\end{aligned}$$

where  $P_{ij}$  are the leading order unpolarized splitting functions

$$P_{qq}(z) = P_{\bar{q}\bar{q}}(z) = C_F \left[ \frac{1+z^2}{(1-z)_+} + \frac{3}{2} \delta(1-z) \right], \quad P_{gq}(z) = P_{g\bar{q}}(z) = C_F \left[ \frac{1+(1-z)^2}{z} \right], \tag{182}$$

and  $\otimes$  represents the convolution integral

$$(f \otimes g)(z) = \int_z^1 \frac{d\zeta}{\zeta} f(z/\zeta) g(\zeta). \tag{183}$$

The “ $()_+$ ” in Eq. (182) denotes the usual plus-distribution. The “ASY” superscript on Eq. (181) symbolizes the asymptotically small  $q_T^2/Q^2$  limit for the cross section. The sum over  $q$  is a sum over all active quark flavors.

### 6.1.3 TMD FFs and the small $q_T$ region

In the small transverse momentum limit of the cross section, the  $W_L$  structure function becomes power suppressed. The cross section in Eq. (171) is simply

$$\frac{d\sigma_{AB}}{dz_A dz_B dq_T} = \frac{\alpha_{\text{em}}^2 z_A z_B q_T}{6\pi Q^2} W_T, \quad (184)$$

and the structure function  $W_T$  (or hadronic tensor) factorizes in a well known way into TMD fragmentation functions

$$W_T = \frac{8\pi^3 z_A z_B}{Q^2} \sum_q \widehat{W}_{T,q} \int \frac{d^2 \mathbf{b}_T}{(2\pi)^2} e^{-i\mathbf{b}_T \cdot \mathbf{q}_T} \left[ \tilde{D}_{H_A/q} \tilde{D}_{H_B/\bar{q}} + \tilde{D}_{A/\bar{q}} \tilde{D}_{B/q} \right], \quad (185)$$

where

$$\widehat{W}_{T,q} = 6Q^2 e_q^2. \quad (186)$$

The  $\tilde{D}_{H/q}$  are the TMD fragmentation functions in transverse coordinate  $\mathbf{b}_T$  space. After evolution, the TMD ff for a hadron  $H$  from quark  $q$  is

$$\begin{aligned} \tilde{D}_{H/q}(z, \mathbf{b}_T; \mu, \zeta_D) &= \sum_j \int_z^1 \frac{d\hat{z}}{\hat{z}^3} \tilde{C}_{j/q}(z/\hat{z}, b_*, \zeta_D, \mu) d_{H/j}(\hat{z}, \mu_b) \\ &\times \exp \left\{ \ln \frac{\sqrt{\zeta_D}}{\mu_b} \tilde{K}(b_*; \mu_b) + \int_{\mu_b}^{\mu} \frac{d\mu'}{\mu} \left[ \gamma(\mu'; 1) - \ln \frac{\sqrt{\zeta_D}}{\mu'} \gamma_K(\mu') \right] \right. \\ &\left. + g_{H/j}(z, b_T) + \frac{1}{2} g_K(b_T) \ln \frac{\zeta_D}{\zeta_{D,0}} \right\} \end{aligned} \quad (187)$$

The  $j$  index runs over all quark flavors and includes gluons, and the functions  $d_{H/j}(z, \mu_b)$  are ordinary collinear ffs which are convoluted with coefficient functions  $C_{j/q}$  derived from

the the small  $b_T$  limit of the TMDs. All perturbative contributions,  $C_{j/q}$ ,  $\tilde{K}$ ,  $\gamma$ , and  $\gamma_K$  are known by now to several orders in  $\alpha_s$  [140, 146].

However, non-perturbative functions also enter to parametrize the truly non-perturbative and intrinsic parts of the TMD functions. These are  $g_{H/j}$ , which is hadron and flavor dependent, and  $g_K$ , which is independent of the nature of hadrons and parton flavors and controls the non-perturbative contribution to the evolution. When combined in a cross section  $\zeta_{DA} \times \zeta_{DB} = Q^4$ . Some common parametrizations used for phenomenological fits are

$$g_{H/j}(z, b_T) = -\frac{1}{4z^2} \langle K_{H/j,T}^2 \rangle b_T^2, \quad (188)$$

$$g_K(b_T) = -\frac{1}{2} g_2 b_T^2. \quad (189)$$

Perturbative parts of calculations are usually regulated in the large  $b_T$  region by using, for example, the  $b_*$  prescription with:

$$b_*(b_T) = \frac{b_T}{\sqrt{1 + (b_T/b_{\max})^2}}, \quad \mu_b(b_*) \propto \frac{1}{b_*}. \quad (190)$$

While there are many ways to regulate large  $b_T$ , and many alternative proposals for parametrizing the non-perturbative TMD inputs  $\langle K_{H/j,T}^2 \rangle$  and  $g_2$ , the above will be sufficient for the purpose of capturing general trends in the comparison of large and small transverse momentum calculations in Sec. 6.3.

## 6.2 Transverse Momentum Hardness

The question of what constitutes large or small transverse momentum warrants special attention, so I now consider how the kinematical configuration of the third parton in graphs of the form of Fig. 16(a), not associated with a fragmentation function, affects the sequence of approximations needed to obtain various types of factorization.<sup>1</sup> Generally, the propagator

---

<sup>1</sup>For this section I allow for the possibility of arbitrarily many hard loops inside  $H$ .

denominators in the hard blob  $H$  can be classified into two types depending on whether  $k_C$  attaches inside a far off-shell virtual loop or to an external leg. If it attaches inside a virtual loop, the power counting is

$$\frac{1}{2 k_C \cdot k_{A,B} + O(Q^2)}, \quad (191)$$

and for an external leg attachment (the off-shell propagators in Fig. 16(b), for example)

$$\frac{1}{2 k_C \cdot k_{A,B} + O(m^2)}. \quad (192)$$

The coefficients of the  $O(Q^2)$  and  $O(m^2)$  are numerical factors roughly of size 1. Here the  $m^2$  is a small mass scale comparable to  $\Lambda_{\text{QCD}}^2$  or a small hadron mass-squared. Possible  $O(m^2)$  terms in the Eq. (191) denominator can always be neglected relative to  $O(Q^2)$  and so have not been written explicitly.

The question that needs to be answered to justify collinear versus TMD factorization is whether the  $2 k_C \cdot k_{A,B}$  terms are also small enough to be dropped, or if they are large enough that they can be treated as hard scales comparable to  $Q^2$ , or if the true situation is somewhere in between. The fixed order calculations like those of the previous section is justified if

$$\left| \frac{2 k_C \cdot k_{A,B}}{Q^2} \right| \quad (193)$$

is not much smaller than 1. A quick estimate of the relationship between this ratio and  $q_{\text{T}}^2/Q^2$  is obtained as follows:

$$\left| \frac{2 k_C \cdot k_{A,B}}{Q^2} \right| \approx \left| \frac{(q - k_{B,A})^2}{Q^2} \right| \approx \left| \frac{(q - \frac{p_{B,A}}{z_{B,A}})^2}{Q^2} \right| = \frac{q_{\text{T}}^2}{Q^2}, \quad (194)$$

where the first “ $\approx$ ” means momentum conservation is used with  $k_{A,B,C}^2 \approx 0$ , and the second “ $\approx$ ” means the standard small  $q_{\text{T}}^2$  approximation for the photon vertex,  $\zeta_A \approx z_A$ , is being used. For the denominator in Eq. (192), the relevant ratio is  $m^2/(2 k_C \cdot k_{A,B})$ , and arguments

similar to the above give

$$\left| \frac{m^2}{2 k_C \cdot k_{A,B}} \right| \approx \frac{m^2}{q_T^2}. \quad (195)$$

If Eq. (194) is  $O(1)$  while Eq. (195) is much less than one, then the approximations on which collinear factorization at large  $q_T^2$  is based are justified.

The situation is reversed if Eq. (195) is  $O(1)$  or larger but Eq. (194) is small. In that case, the neglect of the  $O(m^2)$  effects (including intrinsic transverse momentum) in the Eq. (192) denominators is unjustified. However, the smallness of Eq. (194) means neglecting the  $2k_C \cdot k_{A,B}$  terms in the hard vertex is now valid, and this leads to its own set of extra simplifications. Ultimately, such approximations are analogous to those used in the derivation of TMD factorization.

An additional way to estimate the hardness of  $q_T^2$  is to compare with the kinematical maximum in Eq. (49). For  $z_{A,B} \gtrsim .4$ , it can produce a significantly smaller ratio than Eq. (194). For example, for  $z_{A,B} = .5$ ,  $q_T^{\text{Max}}/Q^2 = 1/3$ . Certainly, small  $q_T^2/Q^2$  approximations fail near such thresholds.

The range of possible transverse momentum regions can be summarized with three categories:

- Intrinsic transverse momentum: Eq. (195) is of size 1 or larger, but Eq. (194) is a small suppression factor. TMD factorization, or a similar approach that accounts for small transverse momentum effects, is needed. Such a kinematical regime is ideal to studying intrinsic transverse momentum properties of fragmentation functions.
- Hard transverse momentum: Eq. (195) is much less than 1, and Eq. (194) is comparable to 1. Therefore, fixed order calculations like those of the previous section are justified.
- Intermediate transverse momentum: Eq. (195) is much less than 1, but Eq. (194) is also much less than one. In this case, the previous two types of approximations are simultaneously justifiable. Transverse momentum dependence is mostly perturbative, but large logarithms of  $q_T^2/Q^2$  imply that transverse momentum resummation and/or

TMD evolution are nevertheless important.

The large transverse momentum fixed order calculations are the most basic of these, since they involve only collinear factorization starting with tree level graphs, so it is worthwhile to confirm that there is a region where they are phenomenologically accurate, as is the aim of the present chapter. Direct comparisons between fixed order calculations and measurements can help to confirm or challenge the above expectations. For example, consider a case where  $Q \sim 10$  GeV while the largest measurable transverse momenta about  $\sim 7$  GeV. Then logarithms of  $q_T^2/Q^2$ , i.e.,  $|\ln .7^2| \sim .7$ , are not large while Eq. (194) is a non-negligible  $\sim 0.5$ . These are ideal kinematics, therefore, for testing the regime where fixed order calculations are expected to apply.

### 6.3 Large and Small Transverse Momentum Comparison

I begin this comparison by computing the fixed order collinear factorization based cross section for the  $q_T^2 \sim Q^2$  region using the DSS14 ff parametrizations [121], and I compare with the calculation of the asymptotic term in Eq. (181). The results are shown for both moderate  $Q \sim 12$  GeV and for large  $Q \sim 50$  GeV in Fig. 18 (left panel), with  $z_{A,B} = 0.3$  in both cases. The horizontal axis is the ratio  $q_T/q_T^{\text{Max}}$ , using Eq. (49) to make the proximity to the kinematical large- $q_T^2$  threshold clearly visible.

The exact kinematical relation (for  $1 \rightarrow 3$  scattering) between  $\zeta_B$  and  $\zeta_A$  is

$$\zeta_B = z_B \frac{(Q^2 + q_T^2)(z_A - \zeta_A)}{q_T^2 z_A + Q^2(z_A - \zeta_A)}, \quad (196)$$

while the cross section in the asymptotically small  $q_T^2/Q^2$  limit has either  $\zeta_A = z_A$  with  $\zeta_B \geq z_B$  or  $\zeta_B = z_B$  with  $\zeta_A \geq z_A$ . The asymptotic phase space in the  $\zeta_B$ - $\zeta_A$  plane approaches a rectangular wedge shape in the small  $q_T^2$  limit, shown as the solid black lines in Fig. 18 (right panel) for fixed values of  $z_A = z_B$ . For comparison, the differently colored dashed, dot-dashed, and dotted lines show the  $\zeta_B$ - $\zeta_A$  curves from Eq. (196) for various nonzero  $q_T^2$ .

The deviation between the colored and black curves gives one indication of the degree of error introduced by taking the small  $q_T^2$  limit. Fig. 18(right panel) shows how these grow at large  $z_{A,B}$ . A non-trivial kinematical correlation forms between momentum fractions  $\zeta_A$  and  $\zeta_B$  in the large  $z_A, z_B$  and large  $q_T^2$  regions. Notice also that the contours are scale independent, since  $q_T^{\text{Max}}$  is proportional to  $Q^2$ , so kinematical errors from small  $q_T$  approximations are likewise scale independent.

The point along the horizontal axis where the asymptotic term turns negative is another approximate indication of the region above which small  $q_T^2/Q^2$  approximations begin to fail and the fixed order collinear factorization treatment should become more reliable, provided  $z_{A,B}$  are at fixed moderate values and  $q_T$  is not too close to the overall kinematical thresholds. That point is shown in Fig. 18(left) for two representative values of small ( $Q = 12$  GeV) and large  $Q = 50$  GeV. The transition is at rather small transverse momentum, roughly  $q_T/q_T^{\text{Max}} \sim 0.2$ , though the exact position depends on a number of details, including the shapes of the collinear fragmentation functions. If the asymptotic term is used as the indicator, then the transition is also roughly independent of  $Q$ .

I am ultimately interested in asking how the fixed order collinear calculation compares with existing TMD ff parametrizations near the small-to-large transverse momentum transition point. A reasonable range of non-perturbative parameters like  $\langle K_{H/j,T}^2 \rangle$  and  $g_2$  in Eqs. (188)–(189), can be estimated from a survey of existing phenomenological fits. I will make the approximation that all light flavors have equal  $\langle K_{H/j,T}^2 \rangle = \langle K_T^2 \rangle$  for pion production. Then values for  $\langle K_{H/j,T}^2 \rangle$  lie in the range from about  $.11 \text{ GeV}^{-2}$  to  $.23 \text{ GeV}^{-2}$  [99], which straddles the value  $0.16 \text{ GeV}^{-2}$  in Ref. [147]. For  $g_2$ , I use a minimum value of 0 to estimate the effect of having no non-perturbative evolution at all, and I use a maximum value of  $.184 \text{ GeV}^{-2}$ , from Ref. [148], which is at the larger range of values that have been extracted. This range also straddles the  $g_2 = .13 \text{ GeV}^{-2}$  found in Ref. [99]. In all cases, I use the lowest order perturbative anomalous dimensions since these were used in most of the Gaussian-based fits above. Collectively, the numbers above produce the blue bands in Fig. 19

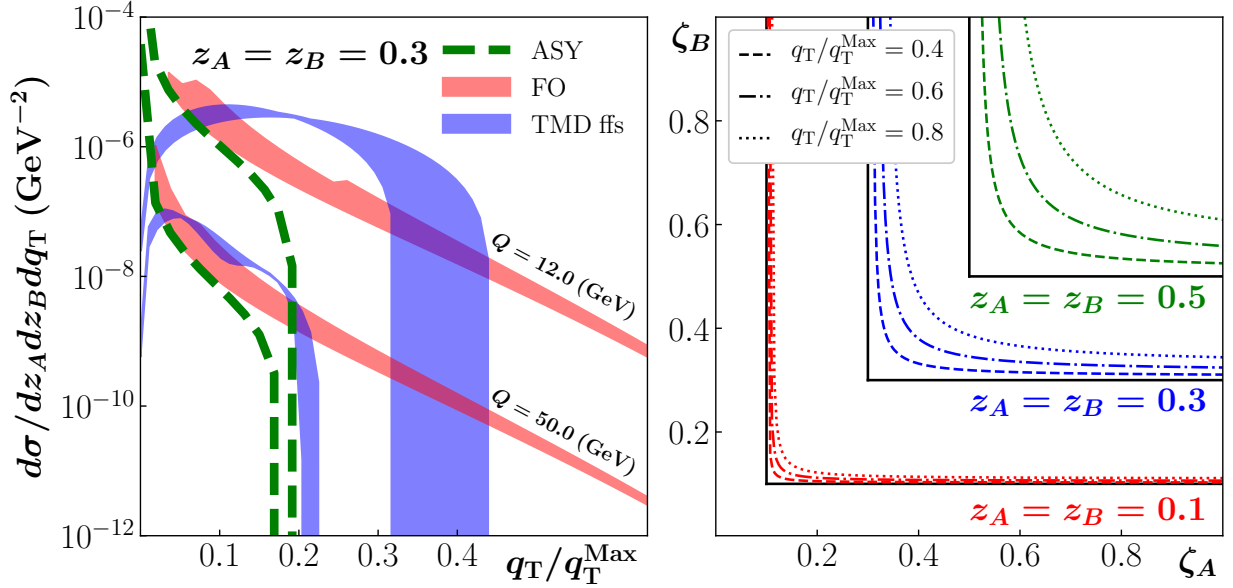


Figure 18: Figure taken from [36]. (left): LO collinear factorization predictions for the inclusive  $e^+e^-$  to dihadron cross section (Sec. 6.1), for  $Q = 12, 50$  GeV. The red band shows the range covered by switching the renormalization group scale between  $\mu = Q$  (lower edge) and  $q_T$  (upper edge). The blue band is the calculation performed using TMD ffs, and the band shows the range covered by the values of the non-perturbative parameters discussed in Sec. 6.3. (right): correlation between partonic momentum fractions  $\zeta_{A,B}$  for various values of  $q_T/q_T^{\text{Max}}$ .

(left). The references quoted above generally include uncertainties for their parametrizations of  $\langle K_{j,T}^2 \rangle$  and  $g_2$ , but these are much smaller than the uncertainty represented by the blue band in Fig. 19 (left). I use a representative estimate of  $b_{\text{max}} = 1.0$   $\text{GeV}^{-1}$ ; Refs. [99] and [148] use slightly larger values (1.123  $\text{GeV}^{-1}$  and 1.5  $\text{GeV}^{-1}$  respectively), but larger  $b_{\text{max}} \gtrsim 1.0$   $\text{GeV}^{-1}$  also has a small effect and only increases the general disagreement with the collinear fixed order calculation.

Observe in Fig. 18 (left) that, despite the somewhat overly liberal band sizes for the TMD ff calculation, large tension in the intermediate transverse momentum region between the TMD ff-based cross section and the fixed order collinear calculation nevertheless remains. For the  $z_{A,B} \approx .3$  shown,  $q_T^{\text{Max}} \approx Q$ . The  $Q = 50$  GeV curves show that as  $Q$  is raised, this tension diminishes, though at a perhaps surprisingly slow rate. For  $Q = 12$  GeV, the asymptotic and fixed order terms approach one another, but only at very small  $q_T$ . The curves contained within the blue band deviate qualitatively from the asymptotic and fixed order terms across all transverse momentum, and the blue band badly overshoots both in the intermediate region of  $q_T \approx 2 - 3$  GeVs. The result is reminiscent of the situation with other processes – see, for example, Fig. 6 of [126] for SIDIS.

Interestingly, data for the observable of Eq. (43) for  $\pi^+/\pi^-$  production simulated with PYTHIA 8 [26, 27] using default settings, shows quite reasonable agreement with the collinear factorization calculation in the expected range of intermediate transverse momentum and  $z_{A,B}$  and very large  $Q$ , validating the analytic fixed order collinear calculation in regions where it is most expected that the collinear calculations and the simulation should overlap. I illustrate this in Fig. 19, where for  $z_{A,B}$  between 0.2 and 0.6 the fixed order analytic calculation

agrees within roughly a factor of 2 with the PYTHIA-generated spectrum for  $Q \gtrsim 20$  GeV and for  $q_T/q_T^{\text{Max}} \sim 0.5$ . At smaller  $Q \lesssim 20$  GeV, the agreement between the fixed order calculation and the simulation is much worse, though because  $Q$  is relatively small and the event generator includes only the leading order hard scattering (with parton showering), it is unclear how the disagreement in that region should be interpreted. Nevertheless, it is interesting to observe that the trend wherein the collinear factorization calculation overshoots data, seen in SIDIS [23] and Drell-Yan [25] calculations, seems to persist even here. In the future, it would be interesting to perform a more detailed Monte Carlo study that incorporates treatments of higher order hard scattering.

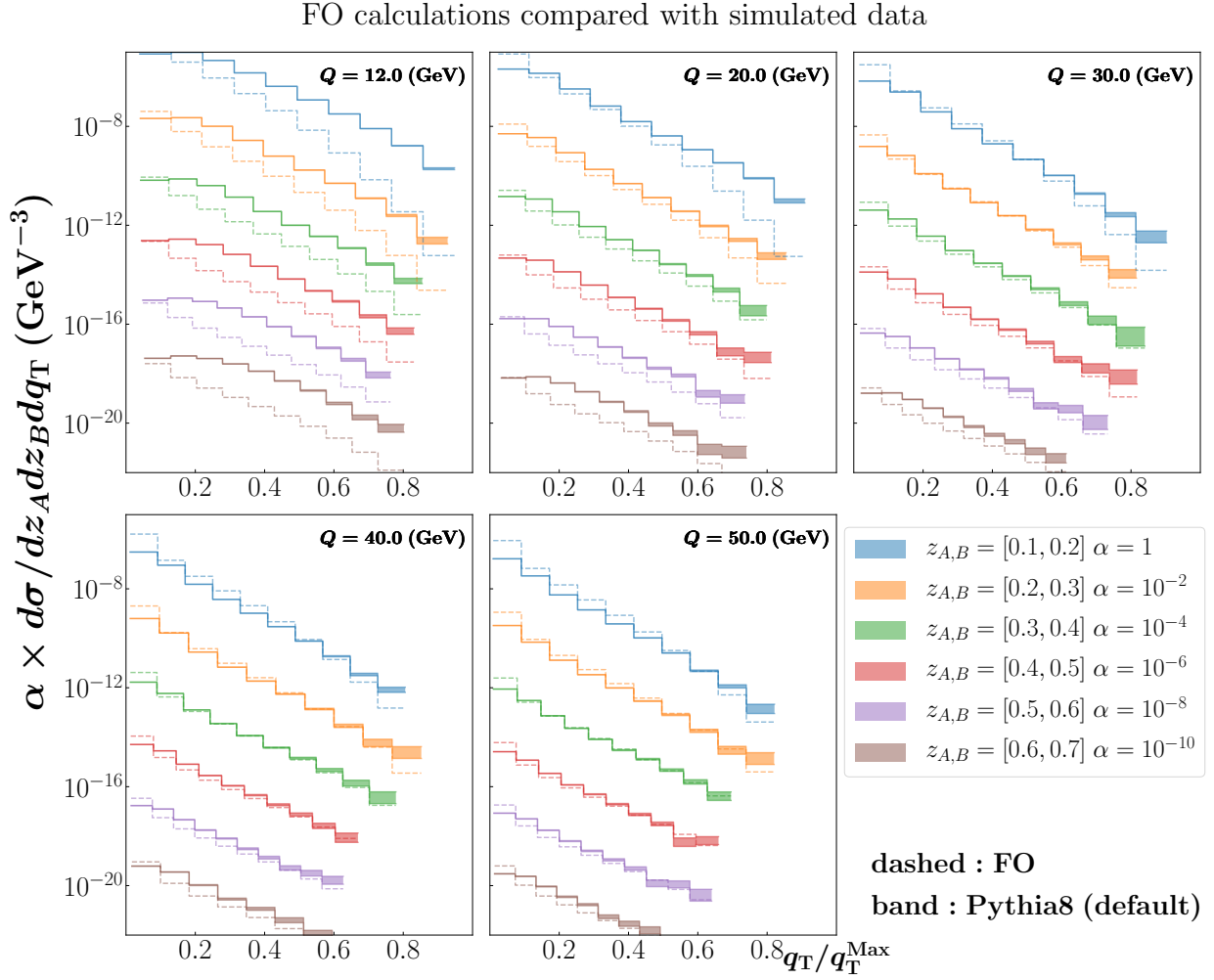


Figure 19: Figure taken from [36]. The lowest order collinear factorization calculation from Sec. 6.1 compared with  $\pi^+/\pi^-$  pair production simulated by PYTHIA-8 with default settings for different ranges of  $z_{A,B}$  and for increasing values of  $Q$ , starting with  $Q = 12$  GeV. Both the fixed-order calculation and the simulation are averaged in the  $z_{A,B}$  bins. The uncertainty on the bands is purely statistical.

## CHAPTER 7

### EXPLORING TRANSVERSE MOMENTUM DEPENDENCE IN SIDIS USING A NEW PDF AND FF FIT

The standard parton correlation functions of QCD, such as collinear parton distribution functions (PDFs) and fragmentation functions (FFs), are being utilized in an increasingly diverse range of phenomenological applications. Beyond their traditional role in predicting new high energy phenomena, they also enter frequently into the study of more complex and extended objects like transverse momentum dependent (TMD) PDFs and FFs and generalized parton distributions (GPDs), where they are needed to understand the transition between different factorization regions. Both TMDs and GPDs are central to the study of the nonperturbative parton structure of hadrons, and understanding how they encapsulate their longitudinal and transverse features will be critical to current experimental programs at Jefferson Lab and elsewhere, as well as to the future Electron-Ion Collider. These considerations provide one of the main motivations for the study of collinear PDFs and FFs in this chapter.

The great value of PDFs and FFs extracted from global QCD data analysis lies with their predictive power, or “universality”. However, the translation from experimental data to quark and gluon operator structures is a challenging inverse problem. It is not possible to exactly constrain parton correlations from data alone since this connection involves nontrivial convolution integrals in a factorization formalism (whose accuracy itself is difficult to quantify in any given instance), and because of the limited quantity of available data. The complexity of the inverse problem is also magnified by the number of flavor degrees of freedom involved.

Nevertheless, assessing and maximizing the universality of collinear PDFs and FFs is crucial given the increasingly broad scenarios where they are used. A major focus in the current effort by the Jefferson Lab Angular Momentum (JAM) Collaboration is therefore to both test and broaden the predictive power of parton correlation functions. This is achieved through a Bayesian inference procedure in which PDFs and FFs are extracted simultaneously, and the uncertainty quantification associated with particular parametrizations of parton correlation

functions is given in terms of a Bayesian posterior distribution. To test universality, the system of equations relating observables to parton correlation functions must of course exceed the total number of correlation functions involved — a minimum requirement is that the parton correlation functions be overconstrained by the data in the fit. Of course, realizing this in practical analyses requires that all parton correlation functions be truly fitted simultaneously. This is a major numerical and technological challenge, and traditionally PDFs and FFs have thus been extracted in separate procedures. However, simultaneous fits can be achieved with the Bayesian Monte Carlo approach, and have been implemented recently in the JAM17 [117] analysis of helicity PDFs, and in the JAM19 [28] analysis of unpolarized PDFs and FFs. The same basic methodology was also applied in the three-dimensional JAM3D20 [149] study, in the first combined analysis of TMD observables that satisfies the overconstraining criterion.

In this chapter, the previous work is extended by performing the first simultaneous and overconstrained fit of unpolarized PDFs and FFs that utilizes both charged hadron production in semi-inclusive deep-inelastic scattering (SIDIS) and single-inclusive  $e^+e^-$  annihilation (SIA). This is partly motivated by a number of recent observations associated with the study of TMD PDFs. For example, significant tension has recently been found between fits performed with standard sets of PDFs and FFs and fixed order perturbative QCD calculations in processes including SIDIS [23, 24], Drell-Yan (DY) [25], and SIA into wide-angle hadron pairs (Chapter 6). A number of suggested solutions and explanations have been proposed to account for this, including a possible need for power suppressed corrections [150] at the moderate scales of most SIDIS experiments. However, more tests of the limits of applicability of standard collinear factorization are needed before it is possible to draw firm conclusions. Given that the majority of data used to constrain collinear correlation functions (both PDFs and FFs) are either highly inclusive or exist are at very high scales, or both, it is perhaps not surprising that tension arises when these are evolved downward and used to make predictions at lower scales and for highly differential observables. Indeed, there have been few tests that

$Q^2$ -scaling, a hallmark of the collinear perturbative regime, actually holds to a reasonable approximation in SIDIS measurements at moderate  $Q^2$ . My hope is that the new combined fit, which I refer to as “JAM20-SIDIS”, will help to shed light on this and similar issues in the future.

In Sec. 7.1 the discussion begins by summarizing the methodology used in this simultaneous Monte Carlo analysis, including the parametrizations used for the distributions and the multi-step Bayesian inference algorithm. Details of the data sets included in the fit are summarized in Sec. 7.2, while in Sec. 7.3 I discuss the criteria for universality and how these are met in this analysis. A detailed discussion of the numerical results is given in Sec. 7.4, where I present the fitted PDFs and FFs, as well as detailed comparisons of data to theory. In Sec. 7.5, I compare predictions using the results of this fit to transverse momentum dependent SIDIS multiplicity data. Much of this work originally appeared in [151].

## 7.1 Theoretical framework

In this section I give an overview of the theoretical framework on which this analysis is based, including the observables to be fitted, the parametrizations used for the PDFs and FFs, details of the perturbative QCD setup, and Bayesian inference strategy employed.

### 7.1.1 Observables and factorization

In this analysis I work in standard collinear factorization [35, 55, 152], in which QCD cross sections are separated into perturbatively calculable partonic hard factors convoluted with nonperturbative PDFs and/or FFs. Calculations of all observables are performed consistently to order  $\alpha_s$  in the QCD coupling. Details of the basic theoretical setups for the inclusive DIS, SIDIS, inclusive Drell-Yan lepton-pair production and SIA reactions are provided in the literature [55, 153–157], and will not be repeated here.

The processes considered in the present analysis can be summarized as follows:

$$\begin{aligned}
\ell + N &\rightarrow \ell + X, && \text{inclusive DIS} \\
\ell + N &\rightarrow \ell + h^\pm + X, && \text{semi-inclusive DIS} \\
N_1 + N_2 &\rightarrow \ell^+ + \ell^- + X, && \text{Drell-Yan lepton-pair production} \\
\ell^+ + \ell^- &\rightarrow h^\pm + X, && \text{single-inclusive annihilation}
\end{aligned}$$

where  $h^\pm$  represent charged pions, kaons, or unidentified hadrons, and the nucleon  $N$  (or  $N_{1,2}$ ) in the initial state can be either a proton or a neutron (in practice, deuteron). Within the framework of collinear factorization, the cross sections for each of these processes can be written schematically as convolutions of hard functions and the nonperturbative parton distribution and fragmentation functions,

$$\frac{d\sigma_{\text{DIS}}}{dQ^2 dx_{\text{Bj}}} = \sum_{i \in \text{flavors}} \mathcal{H}_i^{\text{DIS}} \otimes f_i, \quad \text{inclusive DIS} \quad (197)$$

$$\frac{d\sigma_{\text{SIDIS}}}{dQ^2 dx_{\text{Bj}} dz_h} = \sum_{ij \in \text{flavors}} \mathcal{H}_{ij}^{\text{SIDIS}} \otimes f_i \otimes D_j^h, \quad \text{semi-inclusive DIS} \quad (198)$$

$$\frac{d\sigma_{\text{DY}}}{dQ^2 dx_{\text{F}}} = \sum_{ij \in \text{flavors}} \mathcal{H}_{ij}^{\text{DY}} \otimes f_i \otimes f_j, \quad \text{Drell-Yan lepton-pair production} \quad (199)$$

$$\frac{d\sigma_{\text{SIA}}}{dQ^2 dz_h} = \sum_{j \in \text{flavors}} \mathcal{H}_j^{\text{SIA}} \otimes D_j^h, \quad \text{semi-inclusive annihilation} \quad (200)$$

where the symbols  $\otimes$  represent the convolution integrals in longitudinal momentum fractions of the hard scattering functions  $\mathcal{H}_{ij}$  and the PDFs  $f_i$  and FFs  $D_j^h$  for parton flavors  $i, j$ . In each process,  $Q$  represents the hard scale given by the photon virtuality,  $Q \gg$  hadron masses, which allows the observables to be factorized into the short-distance perturbative and long-distance nonperturbative parts.

For the inclusive DIS and SIDIS processes,

$$x_{\text{Bj}} = \frac{Q^2}{2p \cdot q} \quad (201)$$

is the usual Bjorken scaling variable, while for the DY process the analogous scaling variables are defined as

$$x_1 = \frac{Q^2}{2p_1 \cdot q}, \quad x_2 = \frac{Q^2}{2p_2 \cdot q}, \quad (202)$$

where  $p_1$  and  $p_2$  denote the incoming hadron momenta, with the Feynman scaling variable given by

$$x_F = x_1 - x_2. \quad (203)$$

In the DY center of mass frame, and in the limit of negligible hadron masses ( $\ll Q$ ), the virtual photon rapidity can be written in terms of  $x_1$  and  $x_2$  as

$$y = \frac{1}{2} \ln \frac{x_1}{x_2}. \quad (204)$$

For the processes involving fragmentation to a hadron  $h$  in the final state, one has

$$z_h = \frac{p_h \cdot p}{q \cdot p} \quad [\text{SIDIS}] \quad (205)$$

for SIDIS in Eq. (198), while

$$z_h = \frac{2p_h \cdot q}{Q^2} \quad [\text{SIA}] \quad (206)$$

for SIA in Eq. (200).

### 7.1.2 Perturbative QCD and numerical setups

For the numerical analysis I make use of Mellin space techniques to enable fast evaluations of observables needed for the Bayesian analysis. In particular, the DGLAP evolution equations are solved analytically in Mellin space [158], which allows one to effectively render high-dimensional momentum space convolutions from process-specific factorization theorems, along with the integrals in the DGLAP equations, in the form of lower-dimensional

inverse Mellin transforms. For example, for the inclusive DIS observables one can write schematically

$$\frac{d\sigma_{\text{DIS}}}{dQ^2 dx_{\text{Bj}}} = \sum_{i \in \text{flavors}} \frac{1}{2\pi i} \int dN x_{\text{Bj}}^{-N} \tilde{\mathcal{H}}_i^{\text{DIS}}(N, \mu) U_{ij}^{\text{S}}(N, \mu, \mu_0) \tilde{f}_j(N, \mu_0), \quad (207)$$

where  $N$  here is the conjugate variable to  $x_{\text{Bj}}$ ,  $\tilde{f}_j(N, \mu_0)$  is the Mellin moment of the PDF  $f_j(x, \mu_0)$ , defined by

$$\tilde{f}_j(N, \mu_0) = \int_0^1 dx x^{N-1} f_j(x, \mu_0), \quad (208)$$

and  $\tilde{\mathcal{H}}_i^{\text{DIS}}(N, \mu)$  is the corresponding moment of the partonic DIS cross section. The analytic solution for the DGLAP evolution is entirely encoded in the evolution matrix  $U_{ij}^{\text{S}}$  that evolves the moments  $\tilde{f}_j(N, \mu_0)$  of the PDFs from a given input scale  $\mu_0$  to the relevant DIS hard scale  $\mu = Q$ . A similar expression can be written for the SIA cross section,

$$\frac{d\sigma_{\text{SIA}}}{dQ^2 dz_h} = \sum_{ij \in \text{flavors}} \frac{1}{2\pi i} \int dM z_h^{-M} \tilde{\mathcal{H}}_i^{\text{SIA}}(M, \mu) U_{ij}^{\text{T}}(M, \mu, \mu_0) \tilde{D}_j^h(M, \mu_0) \quad (209)$$

where  $M$  is the Mellin conjugate variable for  $z_h$ ,  $\tilde{D}_j^h(M, \mu_0)$  is the moment of the FF, and  $\tilde{\mathcal{H}}_i^{\text{SIA}}$  is the moment of the partonic SIA cross section. The superscripts S and T in the evolution matrix distinguish between the spacelike and timelike evolution for the PDFs and FFs, respectively, which are encoded in the corresponding DGLAP splitting kernels.

The same procedure can be extended for the case of SIDIS, which gives

$$\begin{aligned} \frac{d\sigma_{\text{SIDIS}}}{dQ^2 dx_{\text{Bj}} dz_h} &= \sum_{ijkl \in \text{flavors}} \frac{1}{(2\pi i)^2} \int dN x_{\text{Bj}}^{-N} \int dM z_h^{-M} \tilde{\mathcal{H}}_{ik}^{\text{SIDIS}}(N, M, \mu) \\ &\times U_{ij}^{\text{S}}(N, \mu, \mu_0) \tilde{f}_j(\mu_0) U_{kl}^{\text{T}}(M, \mu, \mu_0) \tilde{D}_j^h(M, \mu_0). \end{aligned} \quad (210)$$

For the case of the Drell-Yan process, a special treatment is required since the Mellin moments for the partonic cross sections are not known. For this the strategy developed by Stratmann and Vogelsang [159] is employed, where by the Mellin moments are numerically pre-calculated

and used as lookup tables during the analysis. The resulting expression can be written schematically as

$$\begin{aligned} \frac{d\sigma_{\text{DY}}}{dQ^2 dx_{\text{F}}} &= \sum_{ijkl \in \text{flavors}} \frac{1}{(2\pi i)^2} \int dN x_1^{-N} \int dM x_2^{-M} \tilde{\mathcal{H}}_{ik}^{\text{DY}}(N, M, \mu) \\ &\times U_{ij}^{\text{S}}(N, \mu, \mu_0) \tilde{f}_j(\mu_0) U_{kl}^{\text{S}}(M, \mu, \mu_0) \tilde{f}_l(\mu_0), \end{aligned} \quad (211)$$

where  $x_1$  and  $x_2$  are the scaling variables for the incident nucleons. Note that in the Stratmann and Vogelsang strategy [159] the inverse Mellin factors  $x_1^{-N}$  and  $x_2^{-M}$  are integrated numerically with the hard factor  $\tilde{\mathcal{H}}_{ik}^{\text{DY}}(N, M, \mu)$ .

The analytic solutions for the evolution matrices are computed at next-to-leading logarithmic accuracy using splitting kernels up to  $\mathcal{O}(\alpha_s^2)$  and the truncated solution for the single evolution operators (see Ref. [158] for details). The zero-mass variable flavor scheme for solving the DGLAP evolution equations is employed, setting the input scale for the PDFs and FFs at  $\mu_0 = m_c$ . The numerical values for the mass thresholds are taken from the PDG values in the  $\overline{\text{MS}}$  scheme [160]:  $m_c = 1.28$  GeV and  $m_b = 4.18$  GeV. The strong coupling is evolved numerically using the QCD beta function up to  $\mathcal{O}(\alpha_s^2)$ , using the boundary condition  $\alpha_s(M_Z) = 0.118$  at the  $Z$  boson mass,  $M_Z = 91.18$  GeV. Finally, all the process specific hard coefficients are computed at fixed next-to-leading order in pQCD, which are available in the literature [159, 161–163].

### 7.1.3 Parametrization of nonperturbative functions

For the nonperturbative parton distribution and fragmentation functions, standard parametrizations that have been utilized in the literature are used. Namely, for the dependence on the parton momentum fraction  $x$  of the PDF  $f(x)$  the following template function is used

$$f(x, \mu_0) \rightarrow T(x; \mathbf{a}) = \mathcal{M} \frac{x^\alpha (1-x)^\beta (1 + \gamma\sqrt{x} + \delta x)}{\int_0^1 dx x^{\alpha+1} (1-x)^\beta (1 + \gamma\sqrt{x} + \delta x)}, \quad (212)$$

where  $\mathbf{a} = \{\mathcal{M}, \alpha, \beta, \gamma, \delta\}$  is a vector containing the shape parameters ( $\alpha$ ,  $\beta$ ,  $\gamma$ , and  $\delta$ ) and a normalization coefficient ( $\mathcal{M}$ ) to be fitted. The integral in the denominator ensures that the value of the normalization coefficient  $\mathcal{M}$  is equal to the second moment ( $x$ -weighted integral) of the function  $T(x; \mathbf{a})$ . For fitting the PDFs, one can assume isospin symmetry to relate the PDFs in the neutron,  $f_{i/n}(x)$ , to those in the proton,  $f_{i/p}(x) \equiv f_i(x)$ , switching the  $u \leftrightarrow d$  and  $p \leftrightarrow n$  labels for the light quark flavors, and taking the PDFs for other flavors equal for the proton and neutron.

In practice, the valence  $u$  and  $d$  quark distributions are parametrized,  $u_v \equiv f_u - f_{\bar{u}}$  and  $d_v \equiv f_d - f_{\bar{d}}$ , directly using the template function (Eq. (212)). The gluon distribution,  $g \equiv f_g$ , is also directly parametrized per Eq. (212). For the sea quark and antiquark distributions, there are five functions parametrized per Eq. (212). These are a flavor symmetric sea function ( $S$ ) that dominates at very low  $x$  and flavor specific functions ( $q_0(\bar{q}_0)$ ) for the  $s$ ,  $\bar{u}$ ,  $\bar{d}$ , and  $\bar{s}$  that take into account the possible nonperturbative origin of the sea. The distributions for  $s$ ,  $\bar{u}$ ,  $\bar{d}$ , and  $\bar{s}$  are constructed from these per:  $q(\bar{q}) \equiv f_{q(\bar{q})} = S + q_0(\bar{q}_0)$ . Note  $s$  and  $\bar{s}$  are parametrized separately because their contributions to  $K^+$  and  $K^-$  SIDIS data sets differ. The charm and bottom PDFs are not fit. Their contributions are generated purely from the DGLAP evolution. In total there are 8 parametrized PDF functions being fitted. For the valence quark PDFs  $u_v$  and  $d_v$  and the nonperturbative sea components  $\bar{u}_0$  and  $\bar{d}_0$ , there are four shape parameters as in Eq. (212); for all other distributions the  $\gamma$  and  $\delta$  parameters are set to zero. This gives 24 free shape parameters and 8 free normalization parameters. The number of free parameters is further reduced by valence number sum rules, which constrain the normalization parameters  $\mathcal{M}$  for the  $u_v$ ,  $d_v$ , and  $s - \bar{s}$  distributions, whose lowest moments are required to be 2, 1, and zero, respectively. The normalization for the gluon PDF is determined using the momentum sum rule. With these constraints, there is a total of 28 free parameters for the PDFs.

For the  $z$  dependence of FFs, the functional form follows a similar template,

$$D(z, \mu_0) \rightarrow T(z; \mathbf{a}) = \mathcal{M} \frac{z^\alpha (1-z)^\beta (1 + \gamma\sqrt{z} + \delta z)}{\int_0^1 dz z^{\alpha+1} (1-z)^\beta (1 + \gamma\sqrt{z} + \delta z)}, \quad (213)$$

where again the integral in the denominator ensures that the coefficient  $\mathcal{M}$  corresponds to the second moment ( $z$ -weighted integral) of the function. In addition to the fragmentation to pions and kaons studied in earlier JAM analyses of SIA and SIDIS data [28, 164], here the inclusive production of unidentified charged hadrons,  $h^\pm$  are also considered. Accounting for unidentified hadrons can be implemented in two ways. First, the hadron FFs can be fit independently from those for pions and kaons, as preferred by the NNPDF Collaboration [120]. Alternatively, one can take advantage of existing knowledge of specified hadron FFs and add a fitted residual correction to their sum. Such an approach was adopted by de Florian, Sassot, and Stratmann (DSS) [165], for example, in which a residual correction was fitted to the sum of previously obtained pion, kaon, and proton fragmentation functions.

In this analysis I follow the latter approach, but include only the pion and kaon FFs, so that the residual term  $D_i^{\text{res}+}$  parametrizes the difference between the total hadron FF  $D_i^{h+}$  and the  $D_i^{\pi+}$  and  $D_i^{K+}$  functions,

$$D_i^{h+} = D_i^{\pi+} + D_i^{K+} + D_i^{\text{res}+}. \quad (214)$$

To reduce the total number of residual FFs being fit, SU(3) flavor symmetry is assumed for light quarks and antiquarks,

$$D_q^{\text{res}+} = D_u^{\text{res}+} = D_d^{\text{res}+} = D_s^{\text{res}+}, \quad (215a)$$

$$D_{\bar{q}}^{\text{res}+} = D_{\bar{u}}^{\text{res}+} = D_{\bar{d}}^{\text{res}+} = D_{\bar{s}}^{\text{res}+}, \quad (215b)$$

where  $D_q^{\text{res}+}$  and  $D_{\bar{q}}^{\text{res}+}$  are parametrized per the template (Eq. (213)). To allow for differentiation between the residual FFs for light quarks and antiquarks,  $\mathcal{M}$  and  $\beta$  for  $D_{\bar{q}}^{\text{res}+}$  are free

parameters, but  $\alpha$ ,  $\gamma$ , and  $\delta$  are fixed to be the same as for  $D_q^{\text{res}+}$ . This achieves a similar constraint on the parameters as the condition used by DSS [165],  $2D_{\bar{q}}^{\text{res}+} = (1 - z)^{\beta'} D_{q+\bar{q}}^{\text{res}+}$ .

For the pion FFs,  $D_i^{\pi+}$ , the number of fitted functions is reduced by grouping the light quarks into “favored” (valence) and “unfavored” (non-valence) flavors,

$$D_{\text{fav}}^{\pi+} = D_u^{\pi+} = D_d^{\pi+}, \quad (216a)$$

$$D_{\text{unf}}^{\pi+} = D_d^{\pi+} = D_s^{\pi+} = D_{\bar{u}}^{\pi+} = D_{\bar{s}}^{\pi+}, \quad (216b)$$

where  $D_{\text{fav}}^{\pi+}$  and  $D_{\text{unf}}^{\pi+}$  are parametrized per Eq. (213). For the parameters of the kaon FFs,  $D_i^{K+}$ , “unfavored” flavors assumed equal,

$$D_{\text{unf}}^{K+} = D_d^{K+} = D_s^{K+} = D_{\bar{u}}^{K+} = D_{\bar{d}}^{K+}, \quad (217)$$

but leave the favored FFs  $D_u^{K+}$  and  $D_{\bar{s}}^{K+}$  independent. Here  $D_{\text{unf}}^{K+}$ ,  $D_u^{K+}$ , and  $D_{\bar{s}}^{K+}$  are parametrized per Eq. (213). For the heavier flavors, the charm and bottom quark and antiquark FFs are assumed to be equivalent,  $D_c^{h+} = D_{\bar{c}}^{h+}$  and  $D_b^{h+} = D_{\bar{b}}^{h+}$  for  $h = \pi, K, \text{res}$  with  $D_c^{h+}$  and  $D_b^{h+}$  parametrized per Eq. (213). Finally, the gluon FFs  $D_g^{h+}$  for  $h = \pi, K, \text{res}$  are also parametrized per Eq. (213). Charge conjugation symmetry is used to relate FFs for opposite charges by

$$D_q^{h+} = D_{\bar{q}}^{h-}, \quad (218)$$

where  $h = \pi, K, \text{res}$ . This results in 5 fitted functions for pions and residual hadrons, and 6 for kaons.

At this point, there are 17 shape parameters and 5 normalization parameters for residual hadrons, 20 shape parameters, and 5 normalization parameters for pions, and 24 shape parameters and 6 normalization parameters for kaons. The number of shape parameters is reduced further because throughout the fitting procedure, the parameters  $\gamma$  and  $\delta$  for the gluon, charm, and bottom FFs are fixed at zero. In the end there are 16 free parameters to be

fitted for residual charged hadron FFs, 19 free FF pion parameters, and 24 free parameters for the kaon FFs. Together with the 28 PDF parameters, there is a total of 87 free parameters for the fitted functions. In addition, there are also 42 free parameters associated with normalization of various data sets, making for a total of 129 free parameters to be fitted in the analysis.

#### 7.1.4 Bayesian inference

The methodology for extracting nonperturbative PDFs and FFs is based on the general premise of Bayesian inference. Namely, one uses Bayes' theorem to define a multivariate probability distribution  $\mathcal{P}$  for the shape parameters characterizing the PDFs and FFs (the posterior) at a given input scale  $\mu_0$ ,

$$\mathcal{P}(\mathbf{a}|\text{data}) \sim \mathcal{L}(\mathbf{a}, \text{data}) \pi(\mathbf{a}), \quad (219)$$

where  $\mathcal{L}$  is a standard Gaussian likelihood function,

$$\mathcal{L}(\mathbf{a}, \text{data}) = \exp\left(-\frac{1}{2}\chi^2(\mathbf{a}, \text{data})\right), \quad (220)$$

with the  $\chi^2$  function defined by

$$\chi^2(\mathbf{a}) = \sum_{i,e} \left( \frac{d_{i,e} - \sum_k r_e^k \beta_{i,e}^k - T_{i,e}(\mathbf{a})/N_e}{\alpha_{i,e}} \right)^2 + \sum_k (r_e^k)^2 + \left( \frac{1 - N_e}{\delta N_e} \right)^2. \quad (221)$$

Here,  $d_{i,e}$  is the value of the  $i$ -th data point for the experimental dataset  $e$ , with  $T_{i,e}$  the theoretical prediction for the data point;  $\alpha_{i,e}$  is the uncorrelated systematic and statistical uncertainty for each data point added in quadrature;  $\beta_{i,e}^k$  is the  $k$ -th source of point-to-point correlated systematic uncertainties for the  $i$ -th bin of dataset  $e$ , with  $r_e^k$  the related weight; and  $N_e$  and  $\delta N_e$  are the normalization and normalization uncertainty for each data set, respectively. In Eq. (219),  $\pi(\mathbf{a})$  is the prior distribution for the set of parameters  $\mathbf{a}$ , which

is used as input for a given fit to the data.

In principle, given the Bayesian posterior distribution, one can estimate confidence regions for a generic observable  $\mathcal{O}$  (such as a PDF or a function of PDFs or FFs) by integrating over an  $d$ -dimensional parameter space,

$$\mathrm{E}[\mathcal{O}] = \int d^d \mathbf{a} \mathcal{P}(\mathbf{a}|\text{data}) \mathcal{O}(\mathbf{a}), \quad (222\text{a})$$

$$\mathrm{V}[\mathcal{O}] = \int d^d \mathbf{a} \mathcal{P}(\mathbf{a}|\text{data}) (\mathcal{O}(\mathbf{a}) - \mathrm{E}[\mathcal{O}])^2, \quad (222\text{b})$$

where  $\mathrm{E}$  and  $\mathrm{V}$  are the expectation value and variance of the observable  $\mathcal{O}$ . Due to the significant numerical expense of evaluating the likelihood function, the explicit usage of Eqs. (222) is often not practical. Instead, a more efficient option is to build Monte Carlo parameter samples  $\{\mathbf{a}_k; k = 1, \dots, n\}$ , which contain all parameters, including the  $N_e$  from Eq. (221), that are faithfully distributed according to the posterior distribution. These can in turn be used to evaluate the integrals in Eqs. (222) as Monte Carlo sums,

$$\mathrm{E}[\mathcal{O}] = \frac{1}{n} \sum_{k=1}^n \mathcal{O}(\mathbf{a}_k), \quad (223\text{a})$$

$$\mathrm{V}[\mathcal{O}] = \frac{1}{n} \sum_{k=1}^n (\mathcal{O}(\mathbf{a}_k) - \mathrm{E}[\mathcal{O}])^2. \quad (223\text{b})$$

The Monte Carlo sampling strategy is based on data resampling methodology, whereby multiple maximum likelihood optimizations are carried out. Each optimization consists of taking a random point in parameter space and fitting the parameters to data that have been distorted away from the central values by Gaussian shifts within the quoted uncertainties. To build the Monte Carlo samples, the multi-step strategy developed in Ref. [28] is used, where the PDF and FF parameters are pre-optimized to minimize evaluating the likelihood in parameter regions that are strongly disfavored. To that end, The fitting starts by first considering PDF and FF parameters separately using flat priors, with the resulting samples from each type of hadron structure combined at a later stage to build new prior samples

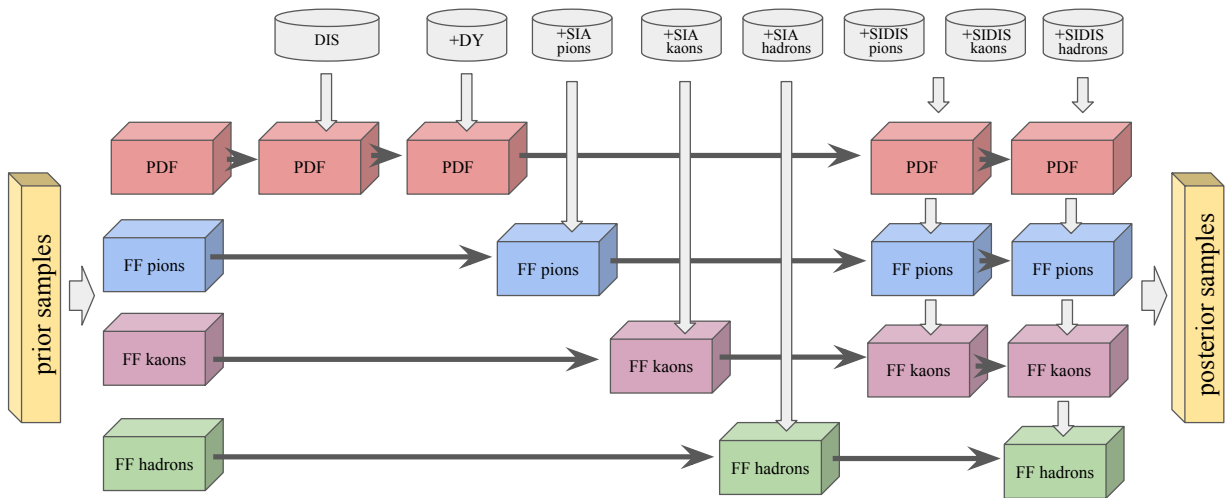


Figure 20: Figure taken from [151]. Schematic illustration of the multi-step workflow employed in this simultaneous Monte Carlo analysis. Each box represents a collection of Monte Carlo samples associated with a specific nonperturbative hadronic structure (PDFs, FFs). The vertical arrows indicate the inclusion of additional datasets from which new optimized Monte Carlo samples (posteriors) are generated as input (priors) for the next step.

for the final runs. The workflow is illustrated in Fig. 20, where each step is represented as vertical arrows that accumulate additional experimental data from the previous step, with the posterior samples at each step becoming the priors for the subsequent step. This strategy allows the samples to become more optimized and avoids unnecessary likelihood evaluations in regions of parameters space by disfavoring those regions in earlier stages of the multi-step chain.

## 7.2 Data Sets

The data sets used in the present analysis include the primary electromagnetic processes that traditionally have been used in global QCD analyses, namely, inclusive DIS, Drell-Yan lepton-

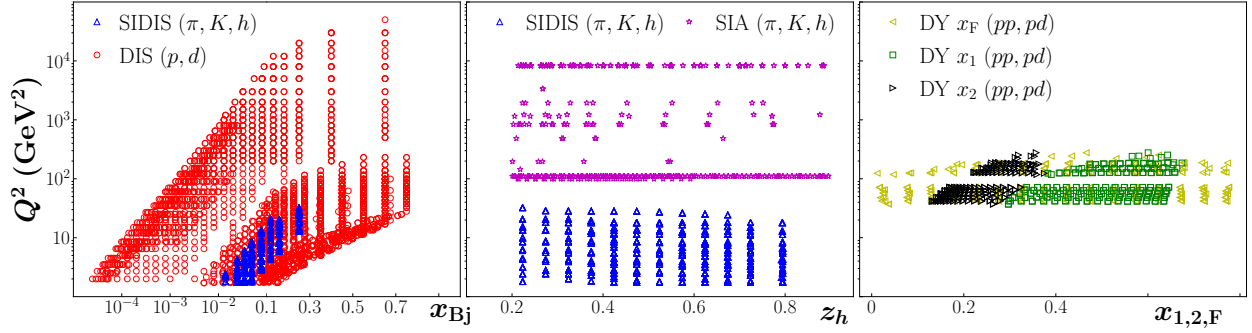


Figure 21: Figure taken from [151]. Kinematic coverage of data used in this analysis, with  $Q^2$  versus the Bjorken scaling variable  $x_{Bj}$  for inclusive DIS [166–171] and SIDIS data [29, 30] (left panel), fragmentation variable  $z$  for SIDIS and SIA data [172–188] (central panel), and momentum fractions  $x_1, x_2, x_F$  for Drell-Yan data [189–191] (right panel).

pair production (which constrain PDFs), SIA (which constrains FFs), and SIDIS (which constrains both PDFs and FFs). The inclusive DIS data are measurements of the  $F_2(x_{Bj}, Q^2)$  structure function performed by the BCDMS [166, 167] and New Muon Collaborations [169, 170] at CERN, and from experiments at SLAC [168], as well as from reduced electron and positron cross sections from the H1 and ZEUS Collaborations [171] at DESY. These include both proton [166, 168, 169] and deuteron [167, 168, 170] targets, and with both neutral and charged current probes [171]. For the kinematics, cuts of  $W^2 > 10 \text{ GeV}^2$  and  $Q^2 > m_c^2$  are used, where  $W^2 = M^2 + Q^2(1 - x_{Bj})/x_{Bj}$ , in order to select DIS data that can be fitted within leading power factorization.

For Drell-Yan lepton-pair production data, differential cross section measurements  $d^2\sigma_{DY}/dQdx_F$  by the E866/NuSea Collaboration [189–191] at Fermilab are used, which include proton scattering from proton and deuteron targets. In [192], the included data is in the range  $Q^2 > 36 \text{ GeV}^2$ . Excluding lower  $Q^2$  data is recommended by [192] which demonstrated that inclusion of the lower  $Q^2$  data results in deteriorated prediction quality with no reduction in

uncertainty when compared with fits to DIS alone.

All SIA measurements are of the normalized differential cross sections  $(d\sigma_{\text{SIA}}/dz_h)/\sigma_{\text{tot}}$  for the reaction  $e^+e^- \rightarrow (\pi^\pm, K^\pm, h^\pm)X$ . The data are from experiments performed by the TASSO [172–174] and ARGUS [185] Collaborations at DESY, by the TPC [175–178], HRS [179], SLD [181] and BaBar [188] Collaborations at SLAC, by the OPAL [183, 193], ALEPH [182] and DELPHI [184] Collaborations at CERN, and by the TOPAZ [180] and Belle [186, 187] Collaborations at KEK. As shown in Fig. 21, the SIA data cover the large- $Q^2$  region where a leading power description in terms of FFs should be accurate. Approximately half of the SIA data points have  $Q \approx M_Z$ , while the Belle and BaBar  $B$  factories have lower  $Q \approx 10.5$  GeV. To ensure applicability of the leading power formalism, the SIA data in these fits are restricted to the range  $0.2 < z_h < 0.9$ .

Identification of heavy quark flavors for some of the SIA datasets is achieved through measurement of the total energy and momentum in secondary vertices. The flavor tagged cross sections for a specific flavor  $q = c$  or  $b$  are particularly sensitive to the  $D_q^h$ ,  $D_{\bar{q}}^h$  and  $D_g^h$  fragmentation functions into the observed hadron  $h$ . In general, however, care needs to be taken with the precise method for separating primary quark flavors, and there are ongoing discussions regarding the optimal approach to this. For more in-depth discussion see, for example, Ref. [164].

Finally, the critical addition in this work compared with the previous JAM19 analysis [28] is the inclusion of unidentified charged hadron data, along with charged pions and kaons, in the SIDIS off deuterium targets from the COMPASS Collaboration [29, 30] at CERN. Since the SIDIS data  $d\sigma_{\text{SIDIS}}^{h^\pm}/dQ^2 dx_{\text{Bj}} dz_h$  are differential in  $x_{\text{Bj}}$  and  $z_h$ , they combine information on both PDFs and FFs, which appear in the description of SIA, Drell-Yan, and DIS data. Furthermore, as illustrated in Fig. 21, the SIDIS data have significant overlap in  $x_{\text{Bj}}$  and  $z_h$  with the  $x_{\text{Bj}}$  and  $x_{\text{F}}$  range of inclusive DIS and Drell-Yan data, respectively, and the  $z_h$  range of SIA data, so that the combined analysis constitutes a genuine test of their universality. For the COMPASS SIDIS data the same kinematic cuts on  $W^2$  and  $Q^2$  as for inclusive DIS

are used, and restrict the fragmentation variable to  $0.2 < z_h < 0.8$  in order to exclude data from the target fragmentation region and avoid large- $z$  threshold corrections.

### 7.3 Assessing universality

Before proceeding to the results of the numerical analysis, I briefly discuss the criteria for universality of the PDFs and FFs and how these are implemented in this analysis. Extracting parton correlation functions, and using the extractions to test models of parton structure, is a nontrivial inverse problem, the detailed examination of which is beyond the scope of the present chapter. However, a claim that the success of a fit is a measure of the predictive power of the PDFs and FFs requires a number of basic minimal conditions to be met:

1. The system of unknown correlation functions must be over-constrained, by which I mean that the constraints on unknown correlations imposed by data (or other theoretical constraints such as sum rules) must be greater than the total number of functions involved.
2. Each unknown correlation function must appear at least twice within the set of factorization formulas relating the correlation functions to physical observables.
3. There must be reasonable kinematical overlap between the observables so that correlation functions can be compared within similar ranges of parton momentum fractions.

Using isospin invariance to relate the PDFs in the proton to those in the neutron, there are seven independent PDFs:  $f_u, f_d, f_s, f_{\bar{u}}, f_{\bar{d}}, f_{\bar{s}}$  and  $f_g$ , with PDFs for heavy flavors generated perturbatively. For the FFs, there are five functions for  $\pi^+$  production:  $D_u^{\pi^+}, D_{\bar{u}}^{\pi^+}, D_c^{\pi^+}, D_b^{\pi^+}$  and  $D_g^{\pi^+}$ , assuming that for equal  $u$  and  $d$  quark masses one can equate  $D_d^{\pi^+} = D_u^{\pi^+}$ . Charge symmetry allows all the FFs for  $\pi^-$  production to be related to those for  $\pi^+$  production. For  $K^+$  production, there are six independent FFs:  $D_u^{K^+}, D_{\bar{s}}^{K^+}, D_{\bar{u}}^{K^+}, D_c^{K^+}, D_b^{K^+}$  and  $D_g^{K^+}$ , where I differentiate between the  $u$  and  $\bar{s}$  functions. Again, using charge symmetry the FFs for  $K^-$  can be obtained from these six  $K^+$  FFs. Finally, for the unidentified charged hadrons

$h^\pm$  or residual FFs, one can identify five independent functions:  $D_u^{\text{res}+}$ ,  $D_{\bar{u}}^{\text{res}+}$ ,  $D_c^{\text{res}+}$ ,  $D_b^{\text{res}+}$  and  $D_g^{\text{res}+}$ . This makes then a total of 23 functions to be determined.

The quark and gluon PDFs are constrained by their appearance in several sum rules. In particular, the number sum rules,

$$\int_0^1 dx (f_q(x) - f_{\bar{q}}(x)) = n_q, \quad (224)$$

where  $n_u = 2$ ,  $n_d = 1$  and  $n_s = 0$ , and the momentum sum rule,

$$\sum_{i=q,\bar{q},g} \int_0^1 dx x f_i(x) = 1. \quad (225)$$

Note that in Section 7.1.3 these constraints were specifically used to fix the values of the normalization parameters for several fitted functions. However, for the purpose of assessing universality, they are simply counted as additional independent equations which include and thus constrain the PDFs.

The data sets discussed in Sec. 7.2 constrain the light quark and gluon PDFs since they appear in expressions for multiple expressions for independent observables. Counting these and also the four sum rules (224) and (225),

$$f_i(x) \xrightarrow{i \neq c,b} \left\{ \begin{array}{ll} 6 & \text{DIS} \\ 2 & \text{Drell-Yan} \\ 6 & \text{SIDIS} \\ 4 & \text{sum rules} \end{array} \right. \quad (226)$$

there is a total of 18 relations between the light quark PDFs. The heavy quarks appear in an even greater number of observables. The light quark fragmentation functions appear in at least one SIA observable and, because of charge conjugation invariance, in 2 SIDIS

observables,

$$D_i^{\pi^+}(z) \xrightarrow{i \neq c, b, g} \begin{cases} 1 & \text{SIA} \\ 2 & \text{SIDIS} \end{cases} \quad (227)$$

and similarly for the kaon and charged hadron fragmentation functions.

For a robust stress-test of universality, there should be reasonable overlap of the ranges in parton momentum fraction for both the PDFs and the FFs. An indication for how well this is achieved in the current fit can be gleaned from the kinematical coverage plots shown in Fig. 21. To lowest order in  $\alpha_s$ , the kinematical variables  $x_{Bj}$ ,  $x_1$ ,  $x_2$  and  $z_h$  approximate the parton momentum fractions  $x$  and  $z$ , respectively, while QCD evolution relates all values of  $Q^2$ . Figure 21 confirms that PDFs and FFs are both constrained by multiple processes in overlapping regions of momentum fractions.

In summary, the analysis does indeed fulfill the basic criterion for qualifying as a test of universality, and retaining predictive power for the PDFs and FFs more generally. Note, however, that the momentum sum rule for FFs has not been imposed in the analysis. Instead, this will be used as a consistency check for the final fit in Sec. 7.4.

## 7.4 Numerical analysis

In this section I present the results of the simultaneous Monte Carlo analysis of PDFs and FFs. I begin with a survey of the fitted cross sections for the various global datasets used in this study, focusing especially on the quality of agreement with the SIDIS and SIA data on  $\pi^\pm$  and  $K^\pm$ , as well as unidentified  $h^\pm$  production. I then present the final fitted PDFs and FFs, and discuss the vital role played by the SIDIS and SIA datasets in particular in constraining the strange quark distribution in the proton.

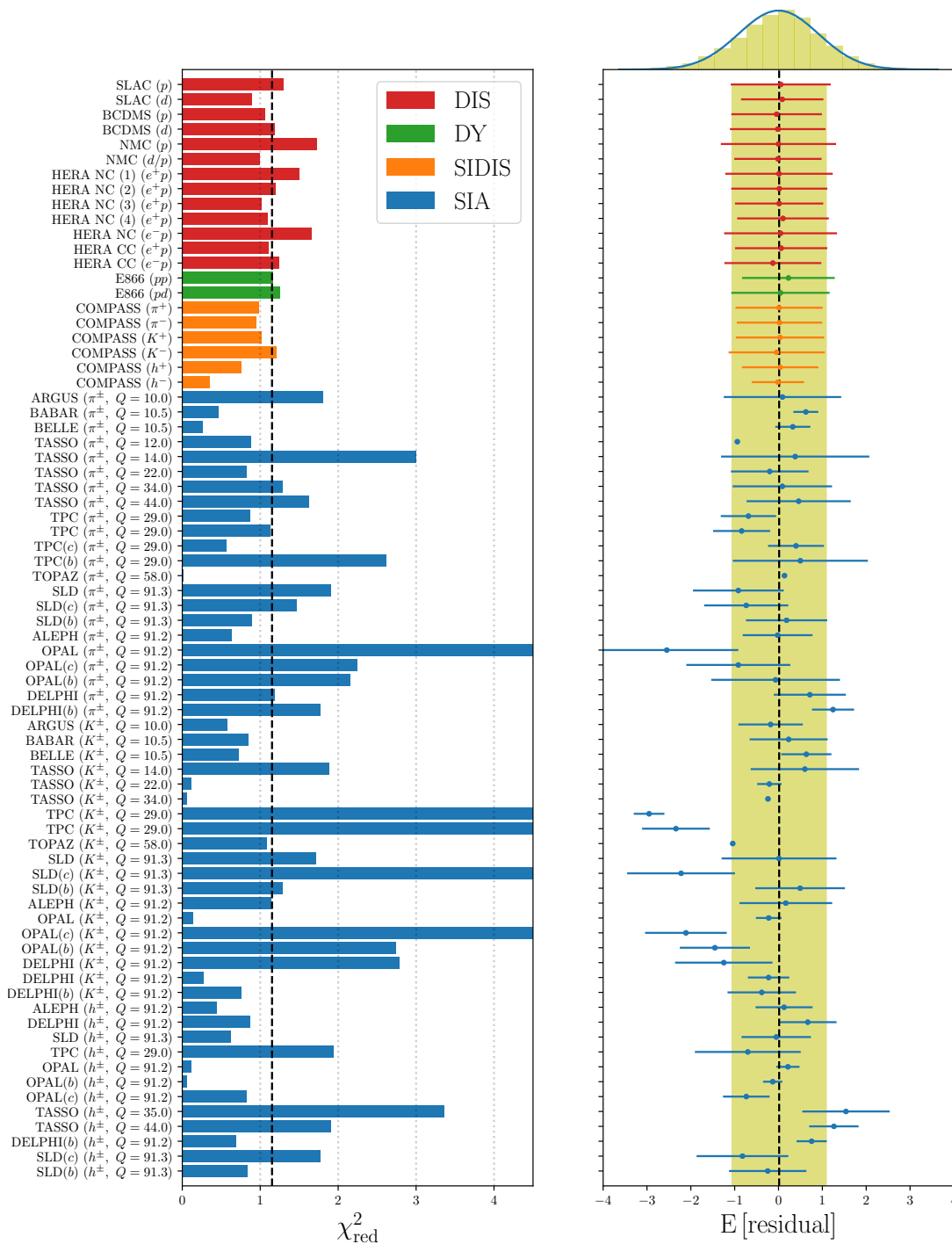


Figure 22: Figure taken from [151].  $\chi_{\text{red}}^2$  values for each DIS (red), DY (green), SIDIS (orange) and SIA (blue) experiment considered in this analysis (left column), along with the corresponding mean and standard deviation of the residuals for each experiment, E [residual] (right column).

### 7.4.1 Data and theory agreement

To assess the agreement of the fitted results with the various datasets, in Fig. 22 I show the reduced  $\chi^2$  for each individual experiment, which is defined by

$$\chi_{\text{red}}^2 = \frac{1}{N} \sum_{i,e} \frac{1}{\alpha_{i,e}^2} \left( d_{i,e} - \text{E} \left[ \sum_k r_e^k \beta_{i,e}^k + T_{i,e}/N_e \right] \right)^2. \quad (228)$$

Here, the expectation value  $\text{E}[\dots]$ , as defined in Eq. (223a), represents the mean theory, including optimized multiplicative and additive corrections to match the data, with  $N$  the total number of data points. In Fig. 22 I show the mean and standard deviation of the Monte Carlo residuals for each experiment  $e$ , where the residual per data point is defined as

$$\text{residual}(e, i) = \frac{1}{\alpha_{i,e}} \left( d_{i,e} - \text{E} \left[ \sum_k r_e^k \beta_{i,e}^k + T_{i,e}/N_e \right] \right). \quad (229)$$

For the inclusive DIS, Drell-Yan and SIDIS datasets there is excellent overall agreement between data and theory, with  $\chi_{\text{red}}^2$  values close to 1. The  $\chi_{\text{red}}^2$  for the SIA datasets are slightly higher, but nonetheless the overall fit is very good, giving a total reduced  $\chi_{\text{red}}^2 = 1.15$  for almost 5000 data points. The values of  $\chi_{\text{red}}^2$  for each type of dataset and for each specific hadron in the final state are summarized in Table 2, along with the number of data points for each dataset.

The residuals profile for the DIS, Drell-Yan and SIDIS datasets is well centered around zero, with variances  $\sim 1$ , indicating an average Gaussian behavior of their associated likelihood function. The variance for the SIDIS  $h^-$  data from COMPASS, however, is found to be up to  $\approx 50\%$  below unity, suggesting a deviation from a Gaussian likelihood. This may be due to the fact that these data are dominated by systematic uncertainties, which is also reflected by the relatively small reduced  $\chi_{\text{red}}^2$  values, especially for the COMPASS  $h^-$  data relative to the rest of DIS and SIDIS data sets.

A more detailed comparison with the COMPASS SIDIS is made in Figs. 23, 24 and 25,

Table 2:  $\chi_{\text{red}}^2$  values for each type of dataset (DIS, Drell-Yan, SIDIS, SIA) considered in this analysis, together with the number of data points  $N_{\text{dat}}$  for each dataset.

reaction	$\chi_{\text{red}}^2$	$N_{\text{dat}}$
DIS	1.25	2680
DY	1.21	250
SIDIS $\pi^\pm$	0.97	498
$K^\pm$	1.11	494
$h^\pm$	0.56	498
SIA $\pi^\pm$	1.21	231
$K^\pm$	1.69	213
$h^\pm$	1.13	120
<b>total</b>	1.15	4984

where I show the  $z_h$  dependence of the  $\pi^\pm$ ,  $K^\pm$  and  $h^\pm$  multiplicities, respectively, which are defined as ratios of SIDIS to inclusive DIS cross sections at the same  $x_{\text{Bj}}$  and  $Q^2$ ,

$$\frac{dM^h}{dz_h} = \frac{d\sigma_{\text{SIDIS}}^h/dQ^2 dx_{\text{Bj}} dz_h}{d\sigma_{\text{DIS}}/dQ^2 dx_{\text{Bj}}}. \quad (230)$$

The agreement between theory and the experimental  $z_h$  spectrum is quite remarkable, given that it spans some 2 orders of magnitude, which suggests that at these kinematics a leading power perturbative QCD factorization at next-to-leading order provides sufficient accuracy to describe the data. Interestingly, the differences between the multiplicities for positively and negatively charged hadron species increase with  $x_{\text{Bj}}$ , especially for kaons, and in the valence region these can differ by an order of magnitude for low values of  $Q^2$ . Such differences can enhance the ability to extract flavor dependent effects in nonperturbative PDFs and parton to kaon FFs from the data. The new data set included for the first time in the present JAM analysis, namely the unidentified charged hadron data shown in Fig. 25, are also well described by the nonperturbative ansatz for the corresponding FFs. In contrast to the excellent agreement with the  $z_h$  dependence of the data in Figs. 23–25, note that

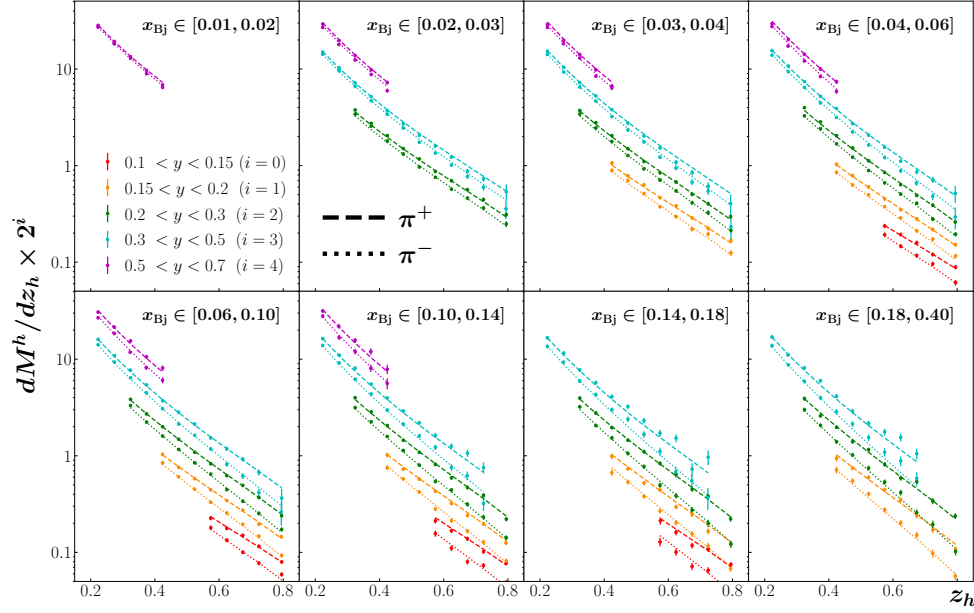


Figure 23: Figure taken from [151]. Comparison of the multiplicities  $dM^h/dz_h$  for  $h = \pi^+$  (dashed lines) and  $\pi^-$  (dotted lines) production with the COMPASS data [29, 30] in various bins of  $x_{Bj}$  and  $y$  (offset by a factor  $2^i$ ).

analysis of the same data differential in the hadron transverse momentum using existing PDFs and FFs within TMD factorization results in poor agreement between predictions and data [23, 24], indicating that further work is needed to understand the SIDIS transverse momentum spectra.

For the SIA data sets, there is a somewhat wider spread in the data versus theory comparisons, as seen in Figs. 26, 27 and 28 for the  $\pi^\pm$ ,  $K^\pm$  and unidentified charged hadron  $h^\pm$  final states, respectively. Generally, the  $h^\pm$  data have the best agreement among the SIA datasets, with a reduced  $\chi_{\text{red}}^2 = 1.13$ , followed by the pion data with  $\chi_{\text{red}}^2 = 1.21$ , and lastly the kaon data, which have an overall reduced  $\chi_{\text{red}}^2 = 1.69$ . For about 3/4 of the  $\approx 40$  SIA datasets, there is very good agreement with the global fit, with  $\chi_{\text{red}}^2 \approx 1$  or below. For the remaining datasets that have larger  $\chi_{\text{red}}^2$  values, to better understand the reasons for some of the tensions between data and theory I discuss in the following some individual cases ranked

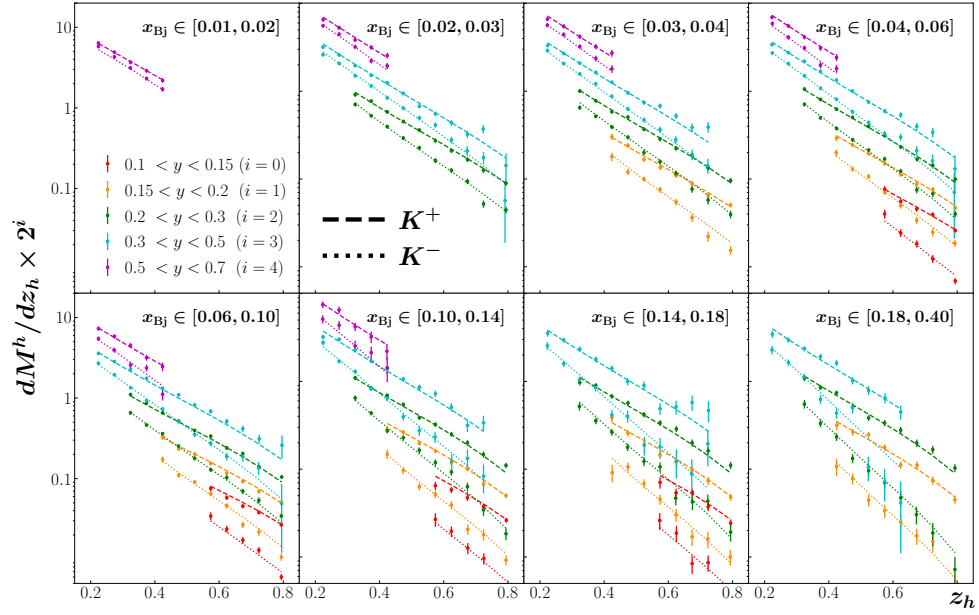


Figure 24: Figure taken from [151]. As in Fig. 23, but for  $K^\pm$  COMPASS SIDIS data [29, 30].

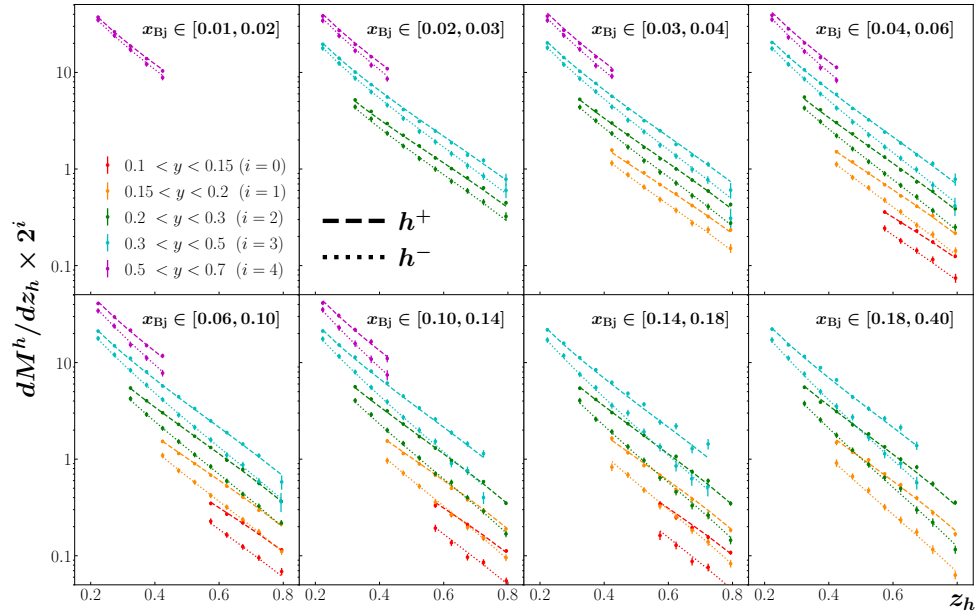


Figure 25: Figure taken from [151]. As in Fig. 23, but for unidentified hadron  $h^\pm$  COMPASS SIDIS data [29, 30].

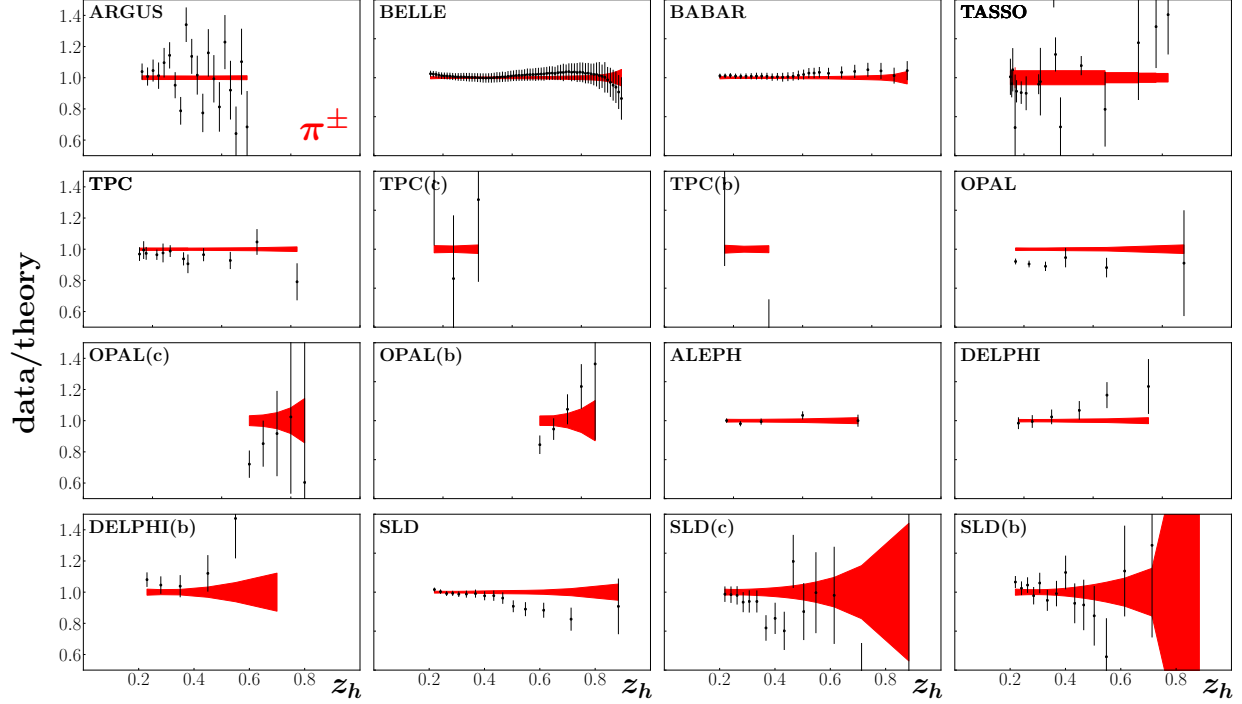


Figure 26: Figure taken from [151]. Data to theory ratios for SIA  $\pi^\pm$  production cross sections versus  $z_h$ , with the bands indicating the uncertainty on the fitted result.

by the reduced  $\chi_{\text{red}}^2$  values.

Starting with the datasets that have the largest  $\chi_{\text{red}}^2$  values, namely,  $\chi_{\text{red}}^2 \gtrsim 3$ , one can identify the OPAL ( $\pi^\pm$  and  $c \rightarrow K^\pm$ ), TPC ( $K^\pm$ ), SLD ( $c \rightarrow K^\pm$ ), and TASSO ( $\pi^\pm$  and  $h^\pm$ ) datasets. For the inclusive OPAL ( $\pi^\pm$ ) data, observe in Fig. 26 that for  $z_h < 0.5$  the data are indeed in tension with the corresponding inclusive ALEPH and SLD results, and the overall trend of the data/theory ratio suggests a possible normalization issue with this dataset. Similarly, from Fig. 27 one can see that the TPC ( $K^\pm$ ) spectrum lies below the theory, suggesting again a normalization problem with these data. The situation for the TASSO ( $\pi^\pm$ ) data is less clear, as only the  $Q = 14$  GeV dataset seems to give a bad fit, while data at other energies can be described fairly well. This again hints at a problem with the overall normalization for this dataset. The same behavior appears also in the TASSO ( $h^\pm$ )

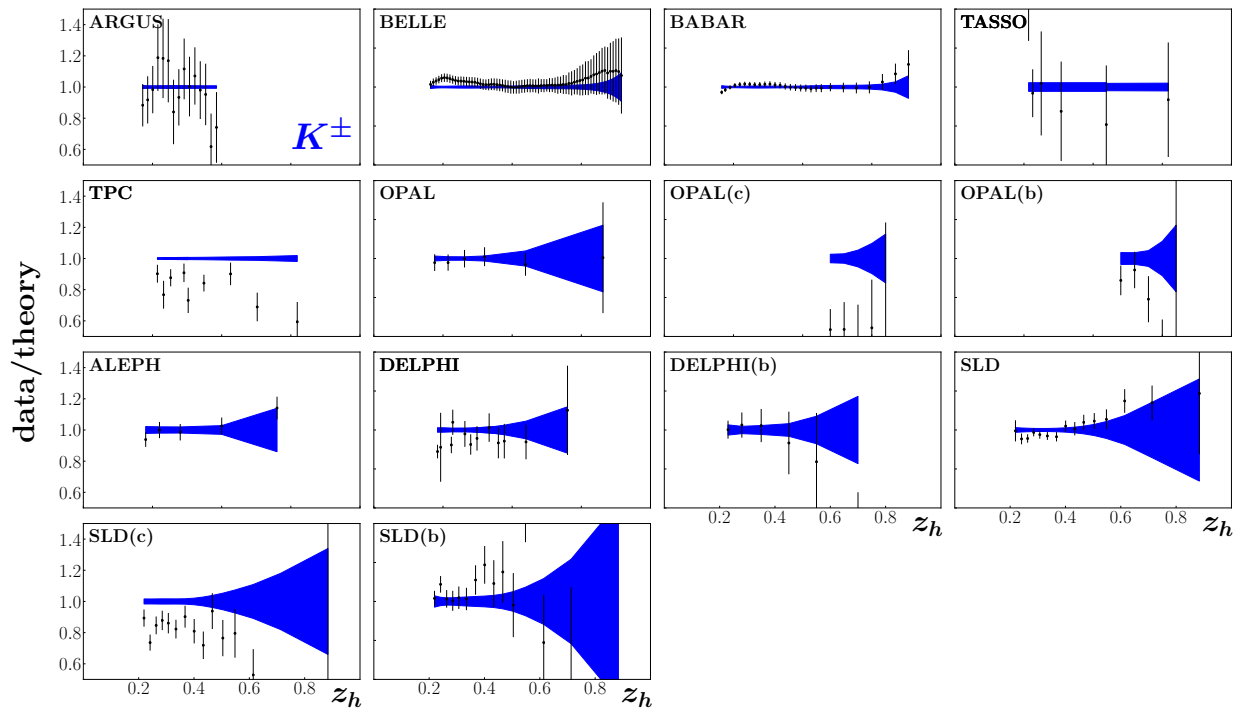


Figure 27: Figure taken from [151]. As in Fig. 26, but for SIA  $K^\pm$  production.

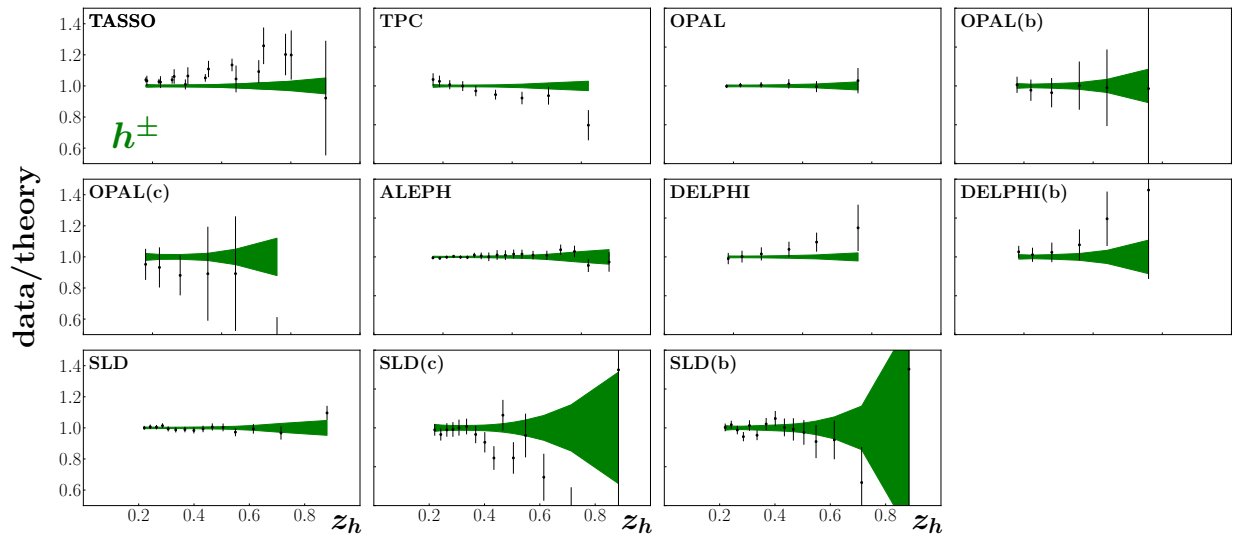


Figure 28: Figure taken from [151]. As in Fig. 26, but for SIA unidentified charged hadron  $h^\pm$  production.

data in Fig. 28, where both the  $Q = 35$  and  $45$  GeV datasets are above the theoretical cross sections. The case of SLD and OPAL ( $c \rightarrow K^\pm$ ) data in Fig. 27 shows a clear overestimation of the  $z_h$  spectra. While one can argue that this problem could be a reflection of the need for a more sophisticated heavy quark treatment in the theory, the description of  $b$ -tagged data from SLD, DELPHI and OPAL is relatively good, so that an explanation in terms of a normalization uncertainty in the SLD and OPAL ( $c \rightarrow K^\pm$ ) data may be more relevant.

For SIA datasets that have smaller, but still large,  $\chi_{\text{red}}^2$  values,  $2 \lesssim \chi_{\text{red}}^2 \lesssim 3$ , I identify the  $b$ -tagged TPC ( $b \rightarrow \pi^\pm$ ), OPAL ( $b \rightarrow \pi^\pm$ ) and OPAL ( $b \rightarrow K^\pm$ ) datasets, as well as the inclusive DELPHI ( $K^\pm$ ) data. For the case of the TPC ( $b \rightarrow \pi^\pm$ ) data, one sees from Fig. 26 that for the largest  $z_h$  bin the theory overestimates the data. On the other hand, good agreement is found for the SLD ( $b \rightarrow \pi^\pm$ ) data at the same kinematics. It is possible that at the smaller  $Q$  values of TPC relative to SLD the range in  $z_h$  where leading power factorization is applicable is narrower, in particular for the  $b$ -tagged data. The  $z_h$  dependence of the OPAL ( $b \rightarrow \pi^\pm$ ) data appear to be clearly different from the theory, even within the large uncertainties. Note here that the OPAL data are presented as truncated moments as a function of the lower limit of the integration,  $z_h^{\text{min}}$ , and the inclusion of the very high  $z_h$  bins may be problematic for the validity of factorization theorems at  $z_h \rightarrow 1$ . Lastly, for the DELPHI ( $K^\pm$ ) spectra one can observe a different shape for one of the energy settings, however, at the same kinematics the theory describes well the corresponding ALEPH and OPAL  $K^\pm$  data, again suggesting possible inconsistencies between some of the individual datasets.

For datasets that have  $\chi_{\text{red}}^2 \lesssim 2$ , I consider the agreement to be generally acceptable. Indeed, the vast majority of datasets in this category have  $\chi_{\text{red}}^2 \approx 1$  or below. These include all of the recent high-statistics  $B$ -factory data from BaBar ( $\pi^\pm, K^\pm$ ) and Belle ( $\pi^\pm, K^\pm$ ), most of the TASSO ( $\pi^\pm, K^\pm$ ), TPC ( $\pi^\pm, c \rightarrow \pi^\pm$ ) and SLD ( $h^\pm, b \rightarrow \pi^\pm, b \rightarrow h^\pm$ ) datasets, all of the ALEPH ( $\pi^\pm, K^\pm, h^\pm$ ) and most of the DELPHI ( $\pi^\pm, K^\pm, b \rightarrow K^\pm, h^\pm, b \rightarrow h^\pm$ ) data, along with the older ARGUS ( $K^\pm$ ), TOPAZ ( $\pi^\pm, K^\pm$ ) and OPAL ( $K^\pm, h^\pm, c \rightarrow h^\pm$ ),

$b \rightarrow h^\pm$ ) data. Slightly higher, but still reasonable,  $\chi_{\text{red}}^2$  values are obtained for the ARGUS ( $\pi^\pm$ ), TPC ( $h^\pm$ ), DELPHI ( $b \rightarrow \pi^\pm$ ), and SLD ( $\pi^\pm$ ,  $K^\pm$ ,  $c \rightarrow \pi^\pm$ ,  $c \rightarrow h^\pm$ ) datasets.

Finally, Note that most of the large  $\chi_{\text{red}}^2$  values found in this analysis were absent in the previous JAM Monte Carlo analysis of fragmentation functions [164]. The main reason is the restriction of the SIA datasets here to the range  $0.2 < z_h < 0.8$ , chosen to coincide with the range over which the SIDIS data in this work are able to be described within collinear factorization. For the LEP data in particular there are many data points at  $z_h < 0.2$  which can be well fitted within the current framework, and which would reduce the overall  $\chi_{\text{red}}^2$ . A careful point by point comparison of the individual  $\chi_{\text{red}}^2$  values for the various datasets indeed confirms that similar discrepancies also occurred in Ref. [164]. However, for consistency in this joint analysis of PDFs and FFs, the kinematic range is restricted to the region where both SIA and SIDIS can be simultaneously described. The same choice for the  $z_h$  range was made in the recent JAM19 analysis, which required SIDIS data to be restricted to  $z_h \gtrsim 0.2$  to ensure separation of the target and current fragmentation regions.

#### 7.4.2 Parton distributions and fragmentation functions

The proton PDFs from the simultaneous fit are displayed in Fig. 29 at a scale  $\mu^2 = 10 \text{ GeV}^2$ , where focus is on the kinematic region of parton momentum fractions  $x \gtrsim 0.01$  that is constrained by the SIDIS data. For comparison, I contrast the results with other next-to-leading order PDF parametrizations, namely, from the CJ15 [194] and NNPDF3.1 [195] global analyses. Compared with the other fits, the valence  $u$  and  $d$  quark distributions have slightly larger magnitude in the intermediate- $x$  region,  $x \sim 0.1$ , with a compensating stronger suppression at small  $x$  needed to ensure that the valence number sum rules are respected. The ratio  $d/u$  is quite compatible with the results from the other groups, on the other hand, but has a significantly larger uncertainty at large  $x$  compared with the CJ15 result, reflecting the Monte Carlo nature of the analysis.

The intermediate- $x$  enhancement in the valence PDFs in this fit is correlated with

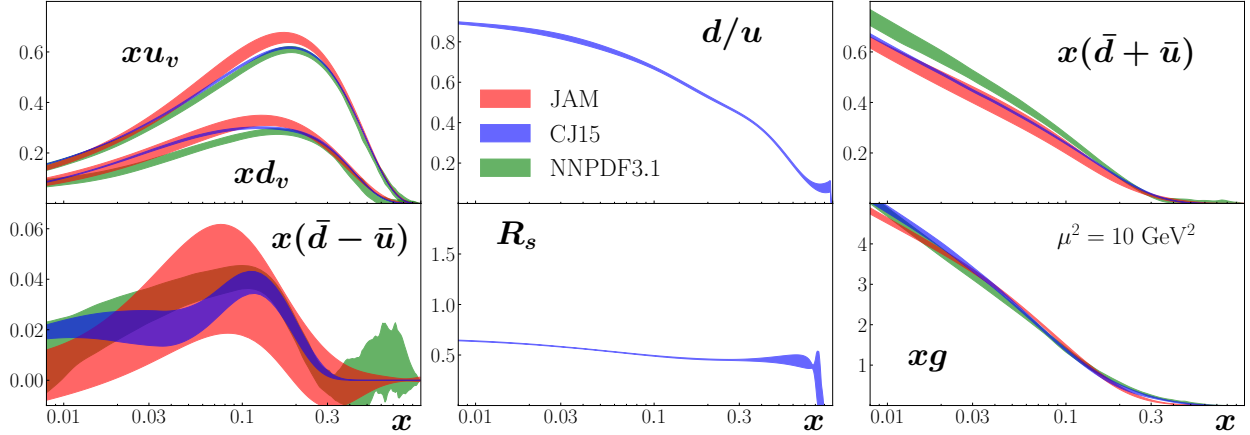


Figure 29: Figure taken from [151]. Proton PDFs from the present JAM20-SIDIS analysis (red bands) versus  $x$  at a scale  $\mu = 10 \text{ GeV}^2$ , compared with the CJ15 [194] (blue bands) and NNPDF3.1 [195] (green bands) parametrizations. The bands shown are  $\text{mean} \pm 1\sigma$ .

the slightly smaller  $\bar{d} + \bar{u}$  light antiquark sea compared with the CJ15 and NNPDF3.1 parametrizations. This in turn is correlated with the behavior of the strange quark sea, as seen in the ratio

$$R_s = \frac{s + \bar{s}}{\bar{d} + \bar{u}} \quad (231)$$

of the strange to nonstrange sea quark PDFs. In Fig. 29 this ratio is generally larger in this analysis than for the other parametrizations, with a somewhat bigger uncertainty. This is understood from the fact that in the CJ15 fit  $R_s$  is fixed to be 0.4 at the input scale, with deviations from the constant value arising only from DGLAP evolution. For the NNPDF3.1 fit the uncertainties are smaller because of their inclusion of the neutrino DIS data, which are not included in this analysis because of unknown nuclear corrections in neutrino scattering [196–198]. The light antiquark asymmetry  $\bar{d} - \bar{u}$  is also compatible with the other groups, but again with a larger uncertainty, which may be related to the absence of collider  $W$  and lepton asymmetry data in this fit. Finally, for the gluon distribution, the

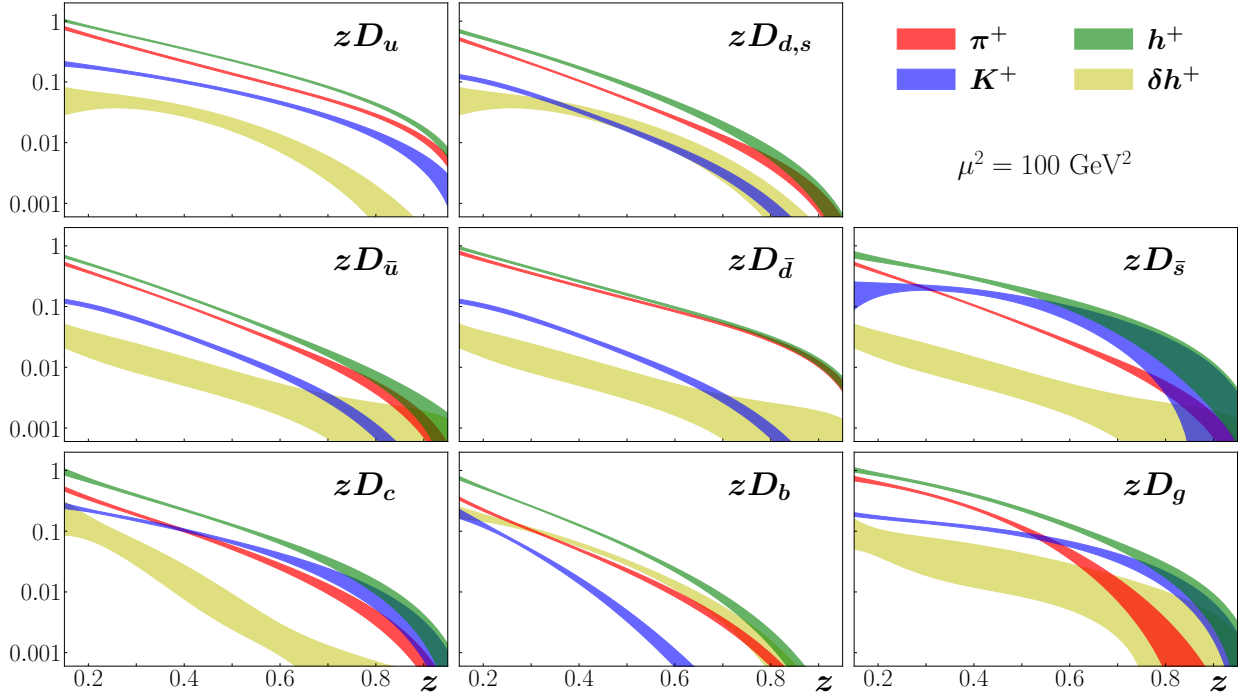


Figure 30: Figure taken from [151]. Parton to hadron FFs versus  $z$  at  $\mu^2 = 100 \text{ GeV}^2$  from the JAM20-SIDIS analysis for various parton flavors fragmenting to  $\pi^+$  (red bands),  $K^+$  (blue bands), unidentified hadrons  $h^+$  (green bands), and residual hadrons  $\delta h^+$  (yellow bands), defined as the difference between  $h^+$  and the sum of  $\pi^+$  and  $K^+$ . The bands shown are  $\text{mean} \pm 1\sigma$ .

magnitude and uncertainties are very similar across all the analyses, even though the fit does not include jet production data from hadron colliders. This reflects the fact that the HERA DIS data, which are included here, provide strong constraints on the shape of the gluon PDF via scaling violations.

For the parton to hadron FFs, I show in Fig. 30 the  $z$  dependence of the FFs at a scale  $\mu^2 = 100 \text{ GeV}^2$  for the positively charged  $\pi^+$ ,  $K^+$  and unidentified hadrons  $h^+$ , as well as for the residual hadrons  $\delta h^+$ , defined as the difference between  $h^+$  and the sum of  $\pi^+$  and

$K^+$  (so that the total is given by  $h^+ = \pi^+ + K^+ + \delta h^+$ ). For most of the flavors the quark  $\rightarrow \pi^+$  fragmentation dominates, as expected from the pion being the lightest hadron in the QCD spectrum. Exceptions to this are for  $\bar{s} \rightarrow K^+$  and  $c \rightarrow K^+$  at intermediate  $z$  values, and for  $b$  quark fragmentation into residual hadrons  $\delta h^+$ .

For gluon fragmentation, pion production dominates for  $z$  up to  $\sim 0.5 - 0.6$ , above which kaon fragmentation becomes as sizeable as the pion. This is consistent with the findings of previous FF analyses [164, 199], which observed that the production of heavier particles such as kaons requires larger momentum fractions from the fragmenting gluon compared to the production of lighter particles.

The production of hadrons heavier than kaons, as indicated in Fig. 30 by the residual hadrons  $\delta h^+$ , can be sizable and comparable to that of kaons, especially for the  $d$  and  $s$  quarks and at large values of  $z$ . The relatively large  $d \rightarrow \delta h^+$  FF can be understood in terms of the fragmentation into protons. Note that flavor symmetry has been imposed for the residual hadron fragmentation, so that  $D_d^{\delta h^+} = D_s^{\delta h^+}$ . In principle, the presence of hyperons such as  $\Sigma^+$  should brake this relation, but analysis of such effects is left for future work. As the case for the  $g \rightarrow K^+$ , the fragmentation of gluons into heavier particles peaks at large  $z$ , where larger momentum fractions from the fragmenting gluons are need for the production of heavier particles.

For production of hadrons initiated by heavy quarks, one can see similar fragmentation of charm quarks into pions and kaons, but a rather different pattern for the fragmentation of bottom quarks. Some of this difference can be explained by the flavor-changing properties of  $u$ -type quarks decaying into  $d$ -type quarks. While the charm quark can decay into strange quarks and hence enhance  $K^+$  production, the same does not occur for bottom quarks, which suppresses kaon production relative to pion production due to the mass difference. Interestingly, the production of other species of charged hadrons is much larger for  $b$  quarks than for  $c$  quarks, which may be understood from the greater phase space available for  $b$  quarks to decay into heavier hadrons to which charm quarks cannot transition.

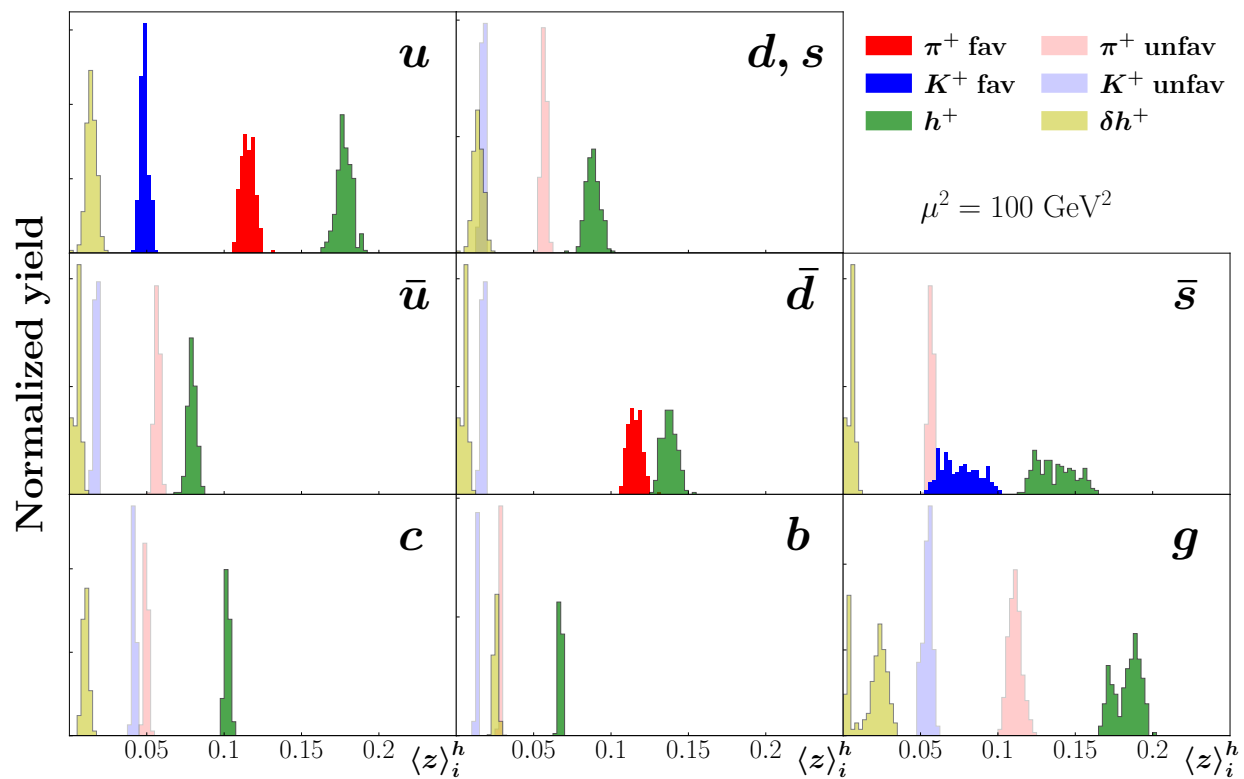


Figure 31: Figure taken from [151]. Normalized yield of truncated moments  $\langle z \rangle_i^h$  of the  $i \rightarrow h$  FFs  $zD_i^h$ , for the favored  $\pi^+$  (red) and favored  $K^+$  (blue), unfavored  $\pi^+$  (light red) and unfavored  $K^+$  (light blue), the total hadron  $h^+$  (green) and residual hadron  $\delta h^+$  (yellow) FFs, at a scale of  $\mu^2 = 100 \text{ GeV}^2$ .

In Fig. 31 I present truncated moments

$$\langle z \rangle_i^h = \int_{z_{\min}}^1 dz z D_i^h(z), \quad (232)$$

for each flavor  $i$  and final state hadron  $h$ , where the lower limits on the  $z$  integration is  $z_{\min} = 0.2$  to restrict the moment to the region of SIDIS kinematics. The truncated moment indicate how energetic is the production different a hadron species  $h$  relative to the parent parton  $i$ . In general, the production of hadron species heavier than pions and kaons is typically produced with lower energies, which is consistent with the physical picture whereby more energy is required to produce heavier hadrons than lighter hadrons.

As expected, the favored fragmentation of  $\bar{d}$  quarks is predominantly into highly energetic pions, while for the antistrange  $\bar{s}$  the production rate of energetic kaons is slightly higher than that of pions. The unfavored fragmentation of  $d, s$  and  $\bar{u}$  quarks follows a similar pattern, with the lightest (pion) state produced at the highest energies followed by kaons and other heavier charged hadrons. An exception to this behavior is for charm and bottom quark fragmentation: for  $c$  quarks kaons are produced with energies comparable to those of pions, while for  $b$  quarks kaon production is suppressed with heavier mass hadrons produced at similar energies as pions.

Interestingly, the production of hadrons from gluons follows the same pattern as for  $u$ -quark fragmentation. While the latter can be explained in terms of mass differences between the produced hadron species, the fact that  $u$  quarks and gluons give a similar average energy profile across hadron species is intriguing. On perturbative grounds one can argue that gluon fragmentation is enhanced because of the  $C_A = 3$  factor in the the gluon splitting function,  $P_{gg}$ , relative to quark splitting functions,  $P_{qq}$  and  $P_{gq}$ , which are proportional to  $C_F = 4/3$ . The absence of direct constraints on the gluon FF beyond scaling violations, however, anything drawing more than speculative conclusions at present.

I conclude the discussion of the numerical results by focusing on the correlation between

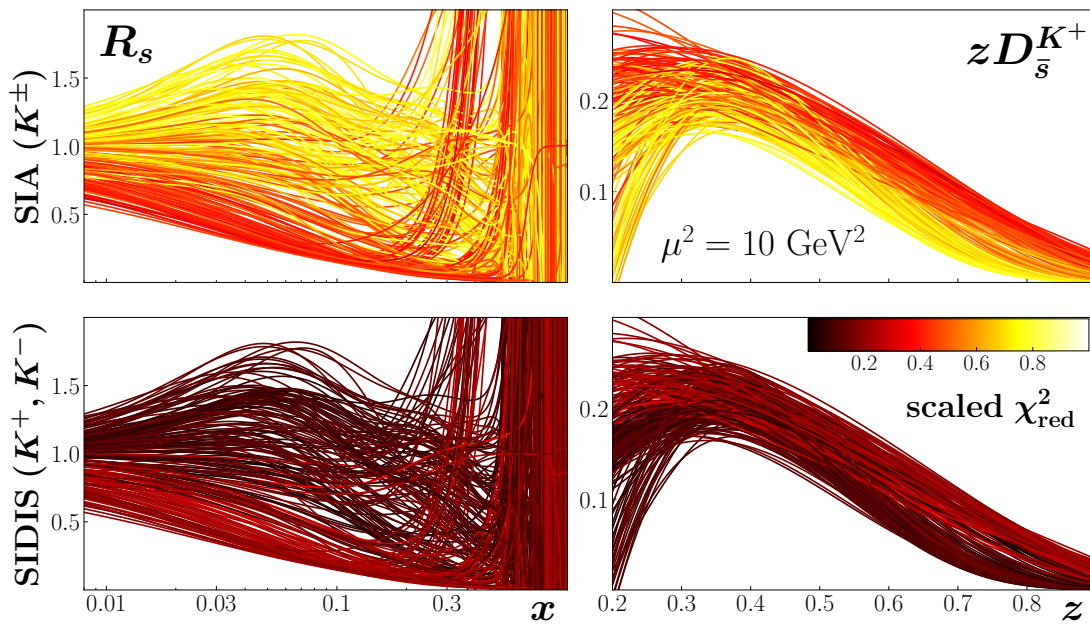


Figure 32: Figure taken from [151]. Monte Carlo samples for the  $R_s$  ratio (left) and  $zD_{\bar{s}}^{K^+}$  FF (right) at  $\mu^2 = 10 \text{ GeV}^2$ , color coded according to the  $\chi^2_{\text{red}}$  for the SIA ( $K^\pm$ ) (top row) and SIDIS ( $K^+, K^-$ ) (bottom row) datasets.

the strange to nonstrange PDF ratio  $R_s$  and the strange to kaon fragmentation function  $D_{\bar{s}}^{K^+}$ . In Fig. 32 I show  $R_s$  and the  $\bar{s} \rightarrow K^+$  FF, with individual Monte Carlo samples color coded by the scaled  $\chi_{\text{red}}^2$  intensity (with darker replicas indicating higher likelihoods) computed for the specific cases of SIA ( $K^\pm$ ) and SIDIS ( $K^+, K^-$ ) datasets. The SIA datasets have a clear preference for a smaller  $R_s$  and enhanced  $D_{\bar{s}}^{K^+}$ , as was found in the previous JAM19 analysis [28]. Interestingly, the SIDIS ( $K^+, K^-$ ) data, which have smaller  $\chi_{\text{red}}^2$ , have a slight tendency to favor solutions with a larger  $R_s$  and smaller  $D_{\bar{s}}^{K^+}$ , however, this preference is much weaker than the preference of the SIA data for smaller  $R_s$  values.

Also note that in the current analysis the flexibility of the PDF and FF parametrizations have been extended, which allowed obtaining a more uniform Monte Carlo distribution of  $R_s$  compared JAM19, where a more restricted parametrization gave rise to multiple solutions. This new analysis confirms that the most probable solutions found in JAM19 did not result from parametrization bias, and corroborates the need for a suppressed strange quark PDF in the proton in order to simultaneously describe both the SIA and SIDIS datasets within leading power QCD factorization.

## 7.5 Transverse momentum dependent SIDIS predictions

One motivation for the work in this chapter was to assess the possible role of limitations in collinear PDF and FF fits in explaining discrepancies between theory and data in the range of intermediate and large transverse momentum across a number of transversely differential processes [23–25, 36]. This can be explored by comparing theoretical predictions for the transverse momentum dependent SIDIS multiplicities generated using the JAM20-SIDIS results discussed in this chapter with available COMPASS data [31]. Fig. 33 shows the results for the  $h^+$  COMPASS data. The dotted lines in Fig. 33 are the predictions using the JAM20-SIDIS results. It is clear that even with this new fit, the theoretical predictions significantly undershoot the data.

To explore this further, two additional fits were performed using the JAM20-SIDIS results

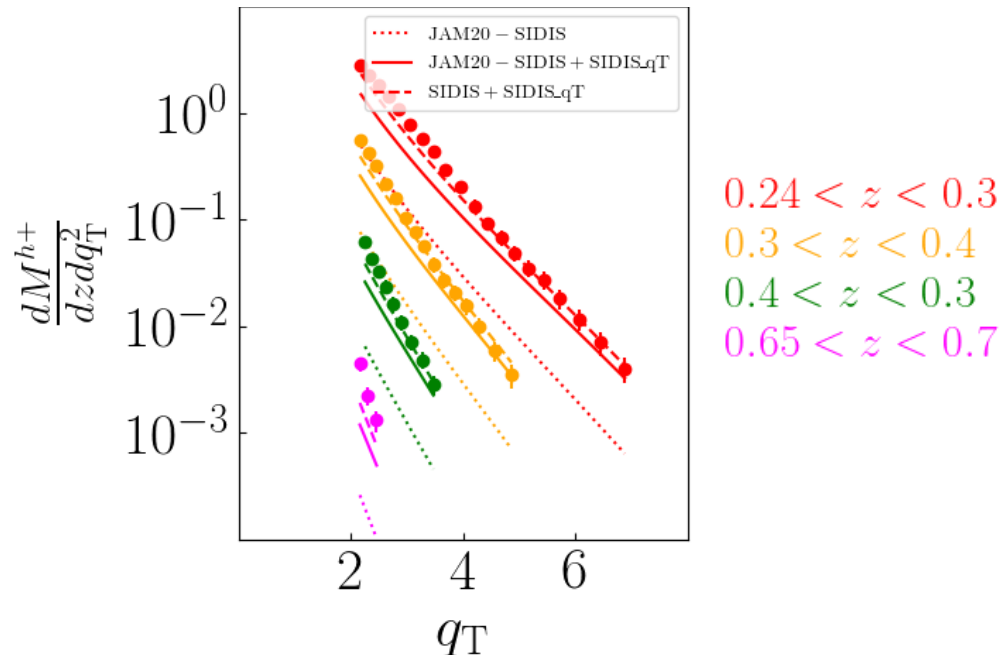


Figure 33: Comparison of theoretical predictions to SIDIS data.

as priors. The first included all of the data from the JAM20-SIDIS fit and added the transverse momentum dependent COMPASS data with the kinematic constraint  $q_T > Q$ . The predictions using the results of this fit are the solid lines in Fig. 33. For the second fit, the data included was only the COMPASS data (the transverse momentum integrated data sets used in JAM20-SIDIS and the transverse momentum dependent data set). The dashed lines in Fig. 33 show the results of that fit. These results clearly demonstrate that inclusion of transverse momentum dependent data in the fit can significantly improve the agreement between theory and data.

## CHAPTER 8

### CONCLUSIONS

In this thesis, I have presented an exploration of the limitations of QCD factorization at more moderate energy scales where the standard approximations may not be valid. Chapter 2 reviewed the kinematics of the various QCD processes relevant to this work. Chapter 3 then presented the basic steps of collinear factorization in DIS to ensure that those approximations were well understood.

In Chapter 4, a simple field theory was used to explore the relevant corrections to collinear factorization. If it is accepted that the range of values for  $m_q$  and  $m_s$  discussed in Secs. 4.1.2 and 4.4.1 is reasonable, then the results in Sec. 4.4.2 indeed imply that all types of power corrections in Eqs. (130a)–(130d) are important in the range of  $Q \sim 1$  GeV and  $x_{Bj} \gtrsim 0.5$ . For such kinematics, all components of partonic momentum are potentially non-negligible, and a power series expansion around the collinear limit may not be sufficient. Here parton transverse momentum and parton virtuality are as important as the target mass in determining the size and behavior of power corrections to collinear factorization. Moreover,  $k^2$  and  $k_T$  are generally not fixed, but rather are correlated with external kinematic variables such as  $x_{Bj}$  and  $Q$ , and in principle take a spectrum of values in convolution integrals.

For slightly larger  $Q$  and smaller  $x_{Bj}$ , power corrections will be smaller but still possibly important. In all cases, they should be calculated explicitly in terms of higher twist functions as in Ref. [53], or with generalizations of factorization that take parton kinematics more fully into account.

In Chapter 4, analysis of power corrections is put into the context of factorization derivations by the application of the canonical collinear factorization approximations for low-order graphs discussed in Chapter 3. This is the appropriate approach to the treatment of power corrections because collinear factorization is, fundamentally, the first term in a  $1/Q$  expansion, performed order-by-order in  $\alpha_s$  in QCD, or in  $\lambda^2$  in the scalar theory of Eq. (99).

There are opportunities for extending analyses like the one in Sec. 4.4 and perhaps using

them directly for phenomenological modeling. In particular, it might be possible to improve constraints on numerical values for  $m_q$  and  $m_s$  in a model theory like the scalar Yukawa theory used here by determining if and how they can be connected to detailed considerations of nonperturbative physics in QCD. The values used in this chapter were chosen through a combination of basic kinematical constraints, extractions of transverse momentum dependent functions, and mass scales typical of nonperturbative quark models. In the future, I hope to obtain tighter and more reliable estimates of the boundary to the factorization collinear regime by appealing to more sophisticated descriptions of nonperturbative physics. Including higher-order radiation to model the effects of parton showering may remove unrealistic features associated with having a fixed target remnant mass. Some of these considerations overlap with the discussions in Ref. [200] of the need to understand nonperturbative aspects of parton momentum.

I stress that there is in principle a distinction between the boundary of the collinear kinematics of collinear factorization and the boundary of the small- $\alpha_s(Q)$  perturbative regime more broadly. Thus, an exciting possibility is that there is a DIS regime at very large  $x_{Bj}$  and large  $Q$  where collinear factorization kinematics break down entirely but an alternative small- $\alpha_s(Q)$  perturbative QCD method applies. An approach like that of Accardi and Qiu [59], which takes into account the role of final states in constraining overall kinematics, is likely needed, but in a form that incorporates more general noncollinear correlation functions. Generalizations of PDFs which smoothly map onto the elastic or exclusive limits may perhaps be appropriate to describe DIS at very large  $x_{Bj}$ . Models such as the quark–diquark theory used in this work can provide hints towards more optimal approaches. The concept of a virtuality-dependent function, discussed recently by Radyushkin [201, 202], may also play an important role in an improved treatment. If a particular approximation is valid or useful, it should be possible to demonstrate the validity of the collinear approximation in the appropriate limits of Sec. 4.3.

In Chapter 5, I have presented a detailed description of the basic structure function

analysis of deeply inelastic scattering in the context of QCD factorization, fully taking into account hadronic masses in order to give clarity to the notion of “purely kinematical” mass effects. Even when clearly stated, however, the meaning of an improvement in the theoretical description of the scattering process from purely kinematical effects of the target mass begs for a physical interpretation.

The discussions in Secs. 5.1–5.4 make clear that an improvement is natural if factorization is understood to apply to scattering off a small invariant mass subsystem or cluster inside a composite target. Models of the nucleon with multiple scales and a clustering structure imply a particular kind of phenomenological prediction — that standard collinear QCD factorization, in the form of AOT framework for treating target masses with exact external kinematics, can be extended to smaller  $Q$  and larger  $x_{Bj}$  than might otherwise be expected from perturbative QCD arguments. In the limit of large  $Q$ , with all other scales fixed, and assuming  $x_{Bj}M \approx Q$ , it is the first terms on the right hand sides of Eqs. (161a) and (161b) that give the asymptotic behavior. The clustering hypothesis suggests that, as  $Q$  decreases, the power corrections initially come mainly from switching between  $x_{Bj}$  and  $x_N$  in the usual factorized expressions, and also accounting for overall kinematic factors such as in Eq. (161b).

An interesting consequence is that the degree of purely kinematical improvement found by keeping the target mass can be viewed as probing the degree of clustering in the target. To quantify this, it will be interesting to investigate how much improvement can be expected within specific models of the target. This way of viewing the target mass effects suggests a variety of future directions for research.

From phenomenological and global QCD analyses of deep inelastic lepton–nucleon scattering data, it is already well established that treatments of the target mass that switch  $x_{Bj}$  to  $x_N$  significantly improve the description of the data and extend its range to lower  $Q$  and larger  $x_{Bj}$  values [74, 194, 203–208]. On the other hand, clear room for refinement exists, for example to distinguish between precise implementations of TMCs that have been proposed in the literature [43, 53, 58–60, 72, 73, 209, 210]. Also, upcoming experiments will

allow for comparison between different target structures, including pions, kaons, and nuclei [211–214]. While the discussion in Chapter 5 was for simplicity restricted to a single flavor, the generalization to the more realistic case of multiple flavors is straightforward. Moreover, the treatment of structure functions in Secs. 5.1 through 5.2 can be directly extended to spin and polarization dependent structure functions. This will be important since the extraction of certain spin dependent effects can be especially sensitive to target mass effects [61–64, 215, 216]. I leave these interesting and important topics for future consideration.

As one of the simplest processes with non-trivial transverse momentum dependence, dihadron production in  $e^+e^-$  annihilation is ideal for testing theoretical treatments of transverse momentum distributions generally. A goal of Chapter 6 was to spotlight its possible use as a probe of the transition between kinematical regions corresponding to different types of QCD factorization. There have been a number of studies highlighting tension between large transverse momentum collinear factorization based calculation and cross section measurements for Drell-Yan and SIDIS, Refs. [21–25]. Whether the resolution lies with a need for higher orders, a need to refit correlation functions, large power-law corrections in the region of moderate  $Q$  [150], or still other factors that are not yet understood remains unclear.

An important early step toward clarifying the issues is an examination of trends in standard methods of calculation in the large transverse momentum region. Motivated by this, I have examined the simplest LO calculation relevant for large deviation from the back-to-back region in detail. Agreement with Monte Carlo-generated distributions at large  $Q$  supports the general validity of such calculations. However, when comparing the result in the intermediate transverse momentum region with expectations obtained from TMD fragmentation functions, one finds trends reminiscent of those discussed above for SIDIS and Drell-Yan scattering at lower  $Q$ . Namely, the collinear factorization calculation appears to be overly suppressed. This is significant motivation to study the intermediate transverse momentum region both theoretically and experimentally. In this respect, forthcoming data sets for dihadron production with transverse momentum dependence from low to moderate

$Q$ , such as the energy available at the BES-III and Belle-II experiments, will be extremely valuable to address these tensions and to investigate the generation of transverse momentum during the hadronization process. Moreover, an advantage in the  $e^+e^-$  annihilation is the larger value of  $Q$  relative to processes like semi-inclusive deep inelastic scattering.

While I have focused on the large transverse momentum limit, the observations above are relevant to other kinematical regions such as small transverse momentum, as well as to polarization dependent observables, and their physical interpretation, since the detailed shape of the transverse momentum distributions for any region depend on the transitions to other regions.

It is important to note that order  $\alpha_s^2$  corrections can be quite large [21–24], and these will be addressed in future studies, though generally higher order effects have not been sufficient in other processes to eliminate tension. Keeping this in mind, it is worthwhile nevertheless to speculate on other possible resolutions. One is that the hard scale  $Q$  might be too low for a simplistic division of transverse momentum into regions such as discussed in Sec. 6.2. It is true that as  $Q$  gets smaller, the separation between large and small transverse momentum becomes squeezed, and it is possible that the standard methods for treating the transition between separately well defined regions is inapplicable. As a hard scale, however,  $Q \sim 12$  GeV is well above energies that are normally understood to be near to the lower limits of applicability of standard perturbation theory methods (typical scales for SIDIS measurements are around  $Q \sim 2$  GeV, for example). Another possibility is that fragmentation functions in the large  $\zeta$  range probed at large  $q_T$  are not sufficiently constrained. An important next step is to determine whether the description of large transverse momentum processes generally can be improved via a simultaneous analysis of multiple processes at moderate  $Q$  with simple and well-established collinear factorization treatments. The need to investigate this motivated the work discussed in the next chapter.

In Chapter 7 I have presented the results of a simultaneous Monte Carlo analysis of PDFs and FFs constrained by a diverse array of data from inclusive and semi-inclusive DIS, Drell-

Yan lepton-pair production, and SIA in  $e^+e^-$  collisions. The analysis extends the previous JAM19 [28] simultaneous fit by including in addition unidentified charged hadrons in the final states of SIDIS and SIA, and increasing the flexibility of the PDF and FF parametrizations.

The analysis — referred to as “JAM20-SIDIS” — represents the most comprehensive determination of parton to hadron ( $\pi^\pm$ ,  $K^\pm$ ,  $h^\pm$ ) FFs fitted concurrently with spin-averaged parton distributions, broadening the test of universality of parton correlation functions to more observables. The more thorough exploration of the parameter space and reduced  $\chi_{\text{red}}^2$  values for each of the  $\approx 70$  datasets fitted in this study confirmed the previous finding [28] that the combination of SIA and SIDIS datasets have a strong preference for a smaller strange to nonstrange PDF ratio,  $R_s$ , correlated with an enhanced  $D_s^{K^+}$  FF. As further tests of this scenario, it is the plan in the future to extend the experimental datasets to include weak-boson and jet production in hadronic collisions, from both Tevatron and LHC data, as well as to relax the  $W^2$  cuts for inclusive DIS to incorporate more fixed-target DIS data at high  $x_{\text{Bj}}$  values [217].

The comparison of theoretical predictions with transverse momentum dependent SIDIS data in Sec. 7.5 demonstrated that the JAM20-SIDIS results still have a significant disagreement with the data. However, when the transverse momentum dependent data is included in the fit, the agreement with the data significantly improves. This is indicative of the necessity of including transverse momentum dependent data in global fits of collinear PDFs and FFs in order to accurately predict the large transverse momentum behavior.

In conclusion, this work has identified corrections to standard factorization that are necessary at moderate energy scales. Masses of initial and final state particles that are large relative to  $Q$  should be accounted for using a purely kinematic approach consistent with the AOT method discussed in Chapter 5. As Chapter 7 demonstrates, fitting of collinear functions should include large transverse momentum data. Ideally, TMD and collinear functions should be fit simultaneously with the full  $W+Y$  calculated at every point to better account for the transition region observed in Chapter 6 where neither the  $W$  nor the  $Y$  contributions

are negligible. Finally, with these corrections incorporated, one would be better positioned to explore corrections due to more dynamic quantities such as parton virtualities found to be relevant in Chapter 4.

## BIBLIOGRAPHY

- [1] E. Rutherford, *Phil. Mag. Ser.6* **21**, 669 (1911).
- [2] E. Rutherford, *Phil. Mag. Ser.6* **37**, 581 (1919), [*Phil. Mag.90,no.sup1,31(2010)*].
- [3] J. Chadwick, *Nature* **129**, 312 (1932).
- [4] J. Chadwick, *Proc. Roy. Soc. Lond.* **A136**, 692 (1932).
- [5] H. Yukawa, *Proc. Phys. Math. Soc. Jap.* **17**, 48 (1935), [*Prog. Theor. Phys. Suppl.1,1(1935)*].
- [6] M. Gell-Mann, *Phys. Lett.* **8**, 214 (1964).
- [7] G. Zweig, (1964).
- [8] G. Zweig, in *DEVELOPMENTS IN THE QUARK THEORY OF HADRONS. VOL. 1. 1964 - 1978*, edited by D. Lichtenberg and S. P. Rosen (1964) pp. 22–101.
- [9] F. Tkachov, (2009), arXiv:0904.0343 [physics.hist-ph] .
- [10] O. W. Greenberg, *Phys. Rev. Lett.* **13**, 598 (1964).
- [11] M. Y. Han and Y. Nambu, *Phys. Rev.* **139**, B1006 (1965), [,187(1965)].
- [12] E. D. Bloom, D. Coward, H. DeStaebler, J. Drees, G. Miller, *et al.*, *Phys.Rev.Lett.* **23**, 930 (1969).
- [13] M. Breidenbach, J. I. Friedman, H. W. Kendall, E. D. Bloom, D. H. Coward, H. C. DeStaebler, J. Drees, L. W. Mo, and R. E. Taylor, *Phys. Rev. Lett.* **23**, 935 (1969).
- [14] J. D. Bjorken and E. A. Paschos, *Phys. Rev.* **185**, 1975 (1969).
- [15] R. P. Feynman, *3rd International Conference on High Energy Collisions Stony Brook, N.Y., September 5-6, 1969*, *Conf. Proc.* **C690905**, 237 (1969).

- [16] H. Fritzsch, M. Gell-Mann, and H. Leutwyler, Phys. Lett. **B47**, 365 (1973).
- [17] D. J. Gross and F. Wilczek, Phys. Rev. Lett. **30**, 1343 (1973).
- [18] H. D. Politzer, Phys. Rev. Lett. **30**, 1346 (1973).
- [19] J. D. Bjorken, Phys. Rev. **179**, 1547 (1969).
- [20] M. A. G. Aivazis, F. I. Olness, and W.-K. Tung, Phys. Rev. D **50**, 3085 (1994).
- [21] A. Daleo, D. de Florian, and R. Sassot, Phys. Rev. **D71**, 034013 (2005), arXiv:hep-ph/0411212 [hep-ph] .
- [22] B. A. Kniehl, G. Kramer, and M. Maniatis, Nucl. Phys. **B711**, 345 (2005), [Erratum: Nucl. Phys.B720,231(2005)], arXiv:hep-ph/0411300 [hep-ph] .
- [23] J. O. Gonzalez-Hernandez, T. C. Rogers, N. Sato, and B. Wang, Phys. Rev. **D98**, 114005 (2018), arXiv:1808.04396 [hep-ph] .
- [24] B. Wang, J. O. Gonzalez-Hernandez, T. C. Rogers, and N. Sato, (2019), arXiv:1903.01529 [hep-ph] .
- [25] A. Bacchetta, G. Bozzi, M. Lambertsen, F. Piacenza, J. Steiglechner, and W. Vogel-sang, (2019), arXiv:1901.06916 [hep-ph] .
- [26] T. Sjöstrand, S. Mrenna, and P. Z. Skands, JHEP **05**, 026 (2006), arXiv:hep-ph/0603175 .
- [27] T. Sjöstrand, S. Ask, J. R. Christiansen, R. Corke, N. Desai, P. Ilten, S. Mrenna, S. Prestel, C. O. Rasmussen, and P. Z. Skands, Comput. Phys. Commun. **191**, 159 (2015), arXiv:1410.3012 [hep-ph] .
- [28] N. Sato, C. Andres, J. Ethier, and W. Melnitchouk, Phys. Rev. D **101**, 074020 (2020), arXiv:1905.03788 [hep-ph] .

- [29] C. Adolph *et al.*, Phys. Lett. B **764**, 1 (2017), arXiv:1604.02695 [hep-ex] .
- [30] C. Adolph *et al.*, Phys. Lett. B **767**, 133 (2017), arXiv:1608.06760 [hep-ex] .
- [31] M. Aghasyan *et al.* (COMPASS), Phys. Rev. D **97**, 032006 (2018), arXiv:1709.07374 [hep-ex] .
- [32] M. Boglione, A. Dotson, L. Gamberg, S. Gordon, J. O. Gonzalez-Hernandez, A. Prokudin, T. C. Rogers, and N. Sato, JHEP **10**, 122 (2019), arXiv:1904.12882 [hep-ph] .
- [33] O. W. Greenberg and D. Bhaumik, Phys. Rev. **D4**, 2048 (1971).
- [34] O. Nachtmann, Nucl. Phys. **B63**, 237 (1973).
- [35] J. C. Collins, *Foundations of Perturbative QCD* (Cambridge University Press, Cambridge, 2011).
- [36] E. Moffat, T. C. Rogers, N. Sato, and A. Signori, Phys. Rev. D **100**, 094014 (2019), arXiv:1909.02951 [hep-ph] .
- [37] C. S. Lam and W.-K. Tung, (1978).
- [38] E. Moffat, W. Melnitchouk, T. C. Rogers, and N. Sato, Phys. Rev. **D95**, 096008 (2017), arXiv:1702.03955 [hep-ph] .
- [39] R. P. Feynman, R. D. Field, and G. C. Fox, Phys. Rev. **D18**, 3320 (1978).
- [40] M. Anselmino, M. Boglione, J. Gonzalez H., S. Melis, and A. Prokudin, JHEP **1404**, 005 (2014), arXiv:arXiv:1312.6261 [hep-ph] .
- [41] A. Signori, A. Bacchetta, M. Radici, and G. Schnell, JHEP **1311**, 194 (2013), arXiv:arXiv:1309.3507 [hep-ph] .

- [42] R. K. Bhaduri, *Models of the Nucleon: From Quarks to Soliton* (Addison-Wesley (1988) (Lecture Notes and Supplements in Physics, 22), Redwood City, USA, 1988) p. 360 p.
- [43] H. Georgi and H. D. Politzer, *Phys. Rev. D* **14**, 1829 (1976).
- [44] C. G. Callan and D. J. Gross, *Phys. Rev. Lett.* **22**, 156 (1969).
- [45] A. W. Thomas and W. Weise, *The Structure of the Nucleon* (Wiley-VCH, Berlin, Germany, 2001) p. 389 p.
- [46] V. N. Gribov and L. N. Lipatov, *Sov. J. Nucl. Phys.* **15**, 438 (1972).
- [47] Y. L. Dokshitzer, *Sov. Phys. JETP* **46**, 641 (1977).
- [48] G. Altarelli and G. Parisi, *Nucl. Phys.* **B126**, 298 (1977).
- [49] G. Sterman, *Nucl. Phys.* **B281**, 310 (1987).
- [50] S. Catani and L. Trentadue, *Nucl. Phys.* **B327**, 323 (1989).
- [51] Yu. L. Dokshitzer, G. Marchesini, and G. P. Salam, *Phys. Lett.* **B634**, 504 (2006), arXiv:hep-ph/0511302 [hep-ph] .
- [52] A. V. Manohar, *Phys. Rev.* **D68**, 114019 (2003), arXiv:hep-ph/0309176 [hep-ph] .
- [53] R. K. Ellis, W. Furmanski, and R. Petronzio, *Nucl. Phys.* **B212**, 29 (1983).
- [54] U. D'Alesio, E. Leader, and F. Murgia, *Phys. Rev. D* **81**, 036010 (2010).
- [55] R. K. Ellis, W. J. Stirling, and B. R. Webber, *Camb. Monogr. Part. Phys. Nucl. Phys. Cosmol.* **8**, 1 (1996).
- [56] E. Moffat, T. C. Rogers, W. Melnitchouk, N. Sato, and F. Steffens, *Phys. Rev. D* **99**, 096008 (2019), arXiv:1901.09016 [hep-ph] .
- [57] S. Kretzer and M. H. Reno, *Phys. Rev. D* **66**, 113007 (2002).

- [58] I. Schienbein *et al.*, J. Phys. G **35**, 053101 (2008).
- [59] A. Accardi and J. Qiu, JHEP **07**, 090 (2008).
- [60] L. T. Brady, A. Accardi, T. J. Hobbs, and W. Melnitchouk, Phys. Rev. D **84**, 074008 (2011).
- [61] S. Wandzura, Nucl. Phys. **B122**, 412 (1977).
- [62] S. Matsuda and T. Uematsu, Nucl. Phys. **B168**, 181 (1980).
- [63] A. Piccione and G. Ridolfi, Nucl. Phys. **B513**, 301 (1998).
- [64] J. Blümlein and A. Tkabladze, Nucl. Phys. **B553**, 427 (1999).
- [65] A. Accardi and A. Signori, PoS **DIS2018**, 158 (2018), arXiv:1808.00565 [hep-ph] .
- [66] G. F. Sterman, Nucl. Phys. **B281**, 310 (1987).
- [67] J. V. Guerrero and A. Accardi, Phys. Rev. D **97**, 114012 (2018).
- [68] J. C. Collins, D. E. Soper, and G. Sterman, Adv. Ser. Direct. High Energy Phys. **5**, 1 (1988), hep-ph/0409313 .
- [69] A. De Rújula, H. Georgi, and H. D. Politzer, Phys. Rev. D **15**, 2495 (1977).
- [70] P. W. Johnson and W.-K. Tung, in *7th International Conference on Neutrinos, Weak Interactions and Cosmology – Neutrino '79, Bergen, Norway* (1979).
- [71] K. Bitar, P. W. Johnson, and W.-K. Tung, Phys. Lett. B **83**, 114 (1979).
- [72] F. M. Steffens and W. Melnitchouk, Phys. Rev. D **73**, 055202 (2006).
- [73] F. M. Steffens, M. D. Brown, W. Melnitchouk, and S. Sanches, Phys. Rev. **C86**, 065208 (2012).
- [74] A. De Rújula, H. Georgi, and H. D. Politzer, Annals Phys. **103**, 315 (1977).

- [75] D. F. Geesaman, K. Saito, and A. W. Thomas, *Ann. Rev. Nucl. Part. Sci.* **45**, 337 (1995).
- [76] S. Malace, D. Gaskell, D. W. Higinbotham, and I. Cloet, *Int. J. Mod. Phys. E* **23**, 1430013 (2014).
- [77] A. W. Thomas, *Phys. Lett.* **126B**, 97 (1983).
- [78] A. I. Signal and A. W. Thomas, *Phys. Lett. B* **191**, 205 (1987).
- [79] Y. Salamu, C.-R. Ji, W. Melnitchouk, and P. Wang, *Phys. Rev. Lett.* **114**, 122001 (2015).
- [80] X. G. Wang, C.-R. Ji, W. Melnitchouk, Y. Salamu, A. W. Thomas, and P. Wang, *Phys. Rev. D* **94**, 094035 (2016).
- [81] D. F. Geesaman and P. E. Reimer, (2018), arXiv:1812.10372 [nucl-ex] .
- [82] F. E. Close, *An Introduction to Quarks and Partons* (Academic Press, London, 1979).
- [83] J.-M. Richard, in *Ferrara International School Niccolò Cabeo 2012: Hadronic Spectroscopy* (2012) arXiv:1205.4326 [hep-ph] .
- [84] J. C. Collins and D. E. Soper, *Nucl. Phys.* **B194**, 445 (1982).
- [85] J. Dudek *et al.*, *Eur. Phys. J.* **A48**, 187 (2012), arXiv:1208.1244 [hep-ex] .
- [86] A. Accardi *et al.*, *Eur. Phys. J.* **A52**, 268 (2016), arXiv:1212.1701 [nucl-ex] .
- [87] J. C. Collins and D. E. Soper, *Nucl. Phys. B* **193**, 381 (1981), [Erratum: *Nucl.Phys.B* 213, 545 (1983)].
- [88] J. C. Collins, D. E. Soper, and G. Sterman, *Nucl. Phys.* **B250**, 199 (1985).
- [89] M. G. Echevarría, A. Idilbi, and I. Scimemi, *JHEP* **1207**, 002 (2012), arXiv:1111.4996 [hep-ph] .

- [90] J. Qiu and X.-F. Zhang, Phys. Rev. **D63**, 114011 (2001), arXiv:hep-ph/0012348 .
- [91] M. Anselmino, M. Boglione, U. D'Alesio, A. Kotzinian, F. Murgia, A. Prokudin, and C. Turk, Phys. Rev. **D75**, 054032 (2007), arXiv:hep-ph/0701006 [hep-ph] .
- [92] M. Anselmino, M. Boglione, U. D'Alesio, A. Kotzinian, F. Murgia, A. Prokudin, and S. Melis, *Proceedings, Ringberg Workshop on New Trends in HERA Physics 2008: Ringberg Castle, Tegernsee, Germany, 5-10 October 2008*, Nucl. Phys. Proc. Suppl. **191**, 98 (2009), arXiv:0812.4366 [hep-ph] .
- [93] M. Anselmino, M. Boglione, U. D'Alesio, S. Melis, F. Murgia, *et al.*, Phys. Rev. **D87**, 094019 (2013), arXiv:1303.3822 [hep-ph] .
- [94] R. Angeles-Martinez *et al.*, Acta Phys. Polon. **B46**, 2501 (2015), arXiv:1507.05267 [hep-ph] .
- [95] Z.-B. Kang, A. Prokudin, P. Sun, and F. Yuan, Phys. Rev. **D93**, 014009 (2016), arXiv:1505.05589 [hep-ph] .
- [96] M. Anselmino, M. Boglione, U. D'Alesio, J. O. Gonzalez Hernandez, S. Melis, F. Murgia, and A. Prokudin, Phys. Rev. **D93**, 034025 (2016), arXiv:1512.02252 [hep-ph] .
- [97] M. Anselmino, M. Boglione, U. D'Alesio, J. O. Gonzalez Hernandez, S. Melis, F. Murgia, and A. Prokudin, Phys. Rev. **D92**, 114023 (2015), arXiv:1510.05389 [hep-ph] .
- [98] A. Bacchetta, M. G. Echevarria, P. J. G. Mulders, M. Radici, and A. Signori, JHEP **11**, 076 (2015), arXiv:1508.00402 [hep-ph] .
- [99] A. Bacchetta, F. Delcarro, C. Pisano, M. Radici, and A. Signori, JHEP **06**, 081 (2017), arXiv:1703.10157 [hep-ph] .

- [100] V. Bertone, I. Scimemi, and A. Vladimirov, JHEP **06**, 028 (2019), arXiv:1902.08474 [hep-ph] .
- [101] A. Vladimirov, (2019), arXiv:1907.10356 [hep-ph] .
- [102] P. M. Nadolsky, AIP Conf.Proc. **753**, 158 (2005), arXiv:hep-ph/0412146 [hep-ph] .
- [103] A. Bacchetta, G. Bozzi, M. Radici, M. Ritzmann, and A. Signori, Phys. Lett. **B788**, 542 (2019), arXiv:1807.02101 [hep-ph] .
- [104] G. Bozzi and A. Signori, Adv. High Energy Phys. **2019**, 2526897 (2019), arXiv:1901.01162 [hep-ph] .
- [105] A. Bermudez Martinez *et al.*, (2019), arXiv:1906.00919 [hep-ph] .
- [106] O. Lupton and M. Vesterinen, (2019), arXiv:1907.09958 [hep-ex] .
- [107] D. Boer, Nucl. Phys. **B806**, 23 (2009), arXiv:0804.2408 [hep-ph] .
- [108] A. Metz and A. Vossen, Prog. Part. Nucl. Phys. **91**, 136 (2016), arXiv:1607.02521 [hep-ex] .
- [109] A. Vossen (CLAS), in *13th Conference on the Intersections of Particle and Nuclear Physics (CIPANP 2018) Palm Springs, California, USA, May 29-June 3, 2018* (2018) arXiv:1810.02435 [hep-ex] .
- [110] J. C. Collins, S. F. Heppelmann, and G. A. Ladinsky, Nucl. Phys. **B420**, 565 (1994), hep-ph/9305309 .
- [111] R. L. Jaffe, X.-m. Jin, and J. Tang, Phys. Rev. Lett. **80**, 1166 (1998), arXiv:hep-ph/9709322 [hep-ph] .
- [112] A. Courtoy, A. Bacchetta, M. Radici, and A. Bianconi, Phys. Rev. **D85**, 114023 (2012), arXiv:1202.0323 [hep-ph] .

- [113] H. H. Matevosyan, A. Bacchetta, D. Boer, A. Courtoy, A. Kotzinian, M. Radici, and A. W. Thomas, *Phys. Rev.* **D97**, 074019 (2018), arXiv:1802.01578 [hep-ph] .
- [114] M. Radici, R. Jakob, and A. Bianconi, *Phys. Rev.* **D65**, 074031 (2002), arXiv:hep-ph/0110252 [hep-ph] .
- [115] M. Radici, A. Courtoy, A. Bacchetta, and M. Guagnelli, *JHEP* **05**, 123 (2015), arXiv:1503.03495 [hep-ph] .
- [116] M. Radici and A. Bacchetta, *Phys. Rev. Lett.* **120**, 192001 (2018), arXiv:1802.05212 [hep-ph] .
- [117] J. J. Ethier, N. Sato, and W. Melnitchouk, *Phys. Rev. Lett.* **119**, 132001 (2017), arXiv:1705.05889 [hep-ph] .
- [118] I. Borsa, R. Sassot, and M. Stratmann, *Phys. Rev.* **D96**, 094020 (2017), arXiv:1708.01630 [hep-ph] .
- [119] V. Bertone, S. Carrazza, N. P. Hartland, E. R. Nocera, and J. Rojo (NNPDF), *Eur. Phys. J.* **C77**, 516 (2017), arXiv:1706.07049 [hep-ph] .
- [120] V. Bertone, N. P. Hartland, E. R. Nocera, J. Rojo, and L. Rottoli (NNPDF), *Eur. Phys. J.* **C78**, 651 (2018), arXiv:1807.03310 [hep-ph] .
- [121] D. de Florian, R. Sassot, M. Epele, R. J. Hernández-Pinto, and M. Stratmann, *Phys. Rev.* **D91**, 014035 (2015), arXiv:1410.6027 [hep-ph] .
- [122] P. B. Arnold and R. P. Kauffman, *Nucl. Phys.* **B349**, 381 (1991).
- [123] E. L. Berger, J.-w. Qiu, and Y.-l. Wang, *Phys. Rev.* **D71**, 034007 (2005), arXiv:hep-ph/0404158 [hep-ph] .
- [124] J. Collins, L. Gamberg, A. Prokudin, T. C. Rogers, N. Sato, and B. Wang, *Phys. Rev.* **D94**, 034014 (2016), arXiv:1605.00671 [hep-ph] .

- [125] M. G. Echevarria, T. Kasemets, J.-P. Lansberg, C. Pisano, and A. Signori, *Phys. Lett.* **B781**, 161 (2018), arXiv:1801.01480 [hep-ph] .
- [126] M. Boggione, J. O. G. Hernandez, S. Melis, and A. Prokudin, *JHEP* **02**, 095 (2015), arXiv:1412.1383 [hep-ph] .
- [127] M. Boggione, J. O. Gonzalez Hernandez, S. Melis, and A. Prokudin, *Proceedings, QCD Evolution Workshop (QCD 2014): Santa Fe, USA, May 12-16, 2014*, *Int. J. Mod. Phys. Conf. Ser.* **37**, 1560030 (2015), arXiv:1412.6927 [hep-ph] .
- [128] P. Sun, J. Isaacson, C. P. Yuan, and F. Yuan, (2014), arXiv:1406.3073 [hep-ph] .
- [129] J. Alwall, R. Frederix, S. Frixione, V. Hirschi, F. Maltoni, O. Mattelaer, H. S. Shao, T. Stelzer, P. Torrielli, and M. Zaro, *JHEP* **07**, 079 (2014), arXiv:1405.0301 [hep-ph] .
- [130] M. Bahr *et al.*, *Eur. Phys. J.* **C58**, 639 (2008), arXiv:0803.0883 [hep-ph] .
- [131] J. Bellm *et al.*, *Eur. Phys. J.* **C76**, 196 (2016), arXiv:1512.01178 [hep-ph] .
- [132] E. Bothmann *et al.*, (2019), arXiv:1905.09127 [hep-ph] .
- [133] G. Schnell, *Proceedings, 4th International Workshop on Transverse Polarization Phenomena in Hard Processes (Transversity 2014): Cagliari, Italy, June 9-13, 2014*, *EPJ Web Conf.* **85**, 02024 (2015).
- [134] F. Hautmann, H. Jung, M. Krämer, P. J. Mulders, E. R. Nocera, T. C. Rogers, and A. Signori, *Eur. Phys. J.* **C74**, 3220 (2014), arXiv:1408.3015 [hep-ph] .
- [135] M. Anselmino, M. Guidal, and P. Rossi, *The European Physical Journal A* **52**, 164 (2016).
- [136] A. Bacchetta, *Eur. Phys. J.* **A52**, 163 (2016).

- [137] E. C. Aschenauer, U. D'Alesio, and F. Murgia, *Eur. Phys. J.* **A52**, 156 (2016), arXiv:1512.05379 [hep-ph] .
- [138] M. Boglione and A. Prokudin, *Eur. Phys. J.* **A52**, 154 (2016), arXiv:1511.06924 [hep-ph] .
- [139] M. Diehl, *Eur. Phys. J.* **A52**, 149 (2016), arXiv:1512.01328 [hep-ph] .
- [140] T. C. Rogers, (2015), arXiv:1509.04766 [hep-ph] .
- [141] I. Garzia and F. Giordano, *Eur. Phys. J.* **A52**, 152 (2016).
- [142] H. Avakian, A. Bressan, and M. Contalbrigo, *Eur. Phys. J.* **A52**, 150 (2016), [Erratum: *Eur. Phys. J.*A52,no.6,165(2016)].
- [143] J. C. Collins, T. C. Rogers, and A. M. Staśto, *Phys. Rev.* **D77**, 085009 (2008), 0708.2833 .
- [144] A. Accardi and A. Signori, (2019), arXiv:1903.04458 [hep-ph] .
- [145] P. Nadolsky, D. R. Stump, and C. P. Yuan, *Phys. Rev.* **D61**, 014003 (1999), arXiv:hep-ph/9906280 [hep-ph] .
- [146] I. Scimemi, *Adv. High Energy Phys.* **2019**, 3142510 (2019), arXiv:1901.08398 [hep-ph] .
- [147] P. Schweitzer, T. Teckentrup, and A. Metz, *Phys. Rev.* **D81**, 094019 (2010), arXiv:1003.2190 [hep-ph] .
- [148] A. V. Konychev and P. M. Nadolsky, *Phys. Lett.* **B633**, 710 (2006), arXiv:hep-ph/0506225 .
- [149] J. Cammarota, L. Gamberg, Z.-B. Kang, J. A. Miller, D. Pitonyak, A. Prokudin, T. C. Rogers, and N. Sato, *Phys. Rev. D* **102**, 054002 (2020), arXiv:2002.08384 [hep-ph] .

- [150] T. Liu and J.-W. Qiu, (2019), arXiv:1907.06136 [hep-ph] .
- [151] E. Moffat, W. Melnitchouk, T. Rogers, and N. Sato, (2021), arXiv:2101.04664 [hep-ph] .
- [152] J. C. Collins, D. E. Soper, and G. F. Sterman, “Factorization of Hard Processes in QCD,” (1989) pp. 1–91, arXiv:hep-ph/0409313 .
- [153] R. Devenish and A. Cooper-Sarkar, *Deep inelastic scattering* (Oxford University Press, Oxford, 2004).
- [154] G. Altarelli, R. K. Ellis, G. Martinelli, and S.-Y. Pi, Nucl. Phys. **B160**, 301 (1979).
- [155] P. Nason and B. R. Webber, Nucl. Phys. **B421**, 473 (1994).
- [156] W. Furmanski and R. Petronzio, Z. Phys. C **11**, 293 (1982).
- [157] D. Graudenz, Nucl. Phys. **B432**, 351 (1994), arXiv:hep-ph/9406274 .
- [158] A. Vogt, Comput. Phys. Commun. **170**, 65 (2005), arXiv:hep-ph/0408244 .
- [159] M. Stratmann and W. Vogelsang, Phys. Rev. D **64**, 114007 (2001), arXiv:hep-ph/0107064 .
- [160] P. Zyla *et al.* (Particle Data Group), PTEP **2020**, 083C01 (2020).
- [161] E. G. Floratos, C. Kounnas, and R. Lacaze, Nucl. Phys. **B192**, 417 (1981).
- [162] S. Kretzer, Phys. Rev. D **62**, 054001 (2000), arXiv:hep-ph/0003177 .
- [163] C. Anastasiou, L. J. Dixon, K. Melnikov, and F. Petriello, Phys. Rev. Lett. **91**, 182002 (2003), arXiv:hep-ph/0306192 .
- [164] N. Sato, J. Ethier, W. Melnitchouk, M. Hirai, S. Kumano, and A. Accardi, Phys. Rev. D **94**, 114004 (2016), arXiv:1609.00899 [hep-ph] .

- [165] D. de Florian, R. Sassot, and M. Stratmann, Phys. Rev. D **76**, 074033 (2007), arXiv:0707.1506 [hep-ph] .
- [166] A. Benvenuti *et al.*, Phys. Lett. B **223**, 485 (1989).
- [167] A. Benvenuti *et al.*, Phys. Lett. B **237**, 592 (1990).
- [168] L. W. Whitlow, E. M. Riordan, S. Dasu, S. Rock, and A. Bodek, Phys. Lett. **B282**, 475 (1992).
- [169] M. Arneodo *et al.*, Nucl. Phys. **B483**, 3 (1997), arXiv:hep-ph/9610231 .
- [170] M. Arneodo *et al.*, Nucl. Phys. **B487**, 3 (1997), arXiv:hep-ex/9611022 .
- [171] H. Abramowicz *et al.*, Eur. Phys. J. C **75**, 580 (2015), arXiv:1506.06042 [hep-ex] .
- [172] R. Brandelik *et al.*, Phys. Lett. B **94**, 444 (1980).
- [173] M. Althoff *et al.*, Z. Phys. C **17**, 5 (1983).
- [174] W. Braunschweig *et al.*, Z. Phys. C **42**, 189 (1989).
- [175] X.-Q. Lu, *Heavy quark jets from  $e^+e^-$  annihilation at 29 GeV*, Ph.D. thesis, John Hopkins University (1986).
- [176] H. Aihara *et al.*, Phys. Rev. Lett. **52**, 577 (1984).
- [177] H. Aihara *et al.*, Phys. Rev. Lett. **61**, 1263 (1988).
- [178] G. D. Cowan, *Inclusive  $\pi^\pm$ ,  $K^\pm$  and  $p\bar{p}$  production in  $e^+e^-$  annihilation at  $\sqrt{s} = 29$  GeV*, Ph.D. thesis, University of California, Berkeley (1988).
- [179] M. Derrick *et al.*, Phys. Rev. D **35**, 2639 (1987).
- [180] R. Itoh *et al.*, Phys. Lett. B **345**, 335 (1995), arXiv:hep-ex/9412015 .
- [181] K. Abe *et al.*, Phys. Rev. D **69**, 072003 (2004), arXiv:hep-ex/0310017 .

- [182] D. Buskulic *et al.*, Z. Phys. C **66**, 355 (1995).
- [183] R. Akers *et al.*, Z. Phys. C **63**, 181 (1994).
- [184] P. Abreu *et al.*, Eur. Phys. J. C **5**, 585 (1998).
- [185] H. Albrecht *et al.*, Z. Phys. C **44**, 547 (1989).
- [186] M. Leitgab *et al.*, Phys. Rev. Lett. **111**, 062002 (2013), arXiv:1301.6183 [hep-ex] .
- [187] M. Leitgab, *Precision measurement of charged pion and kaon multiplicities in  $e^+e^-$  annihilation at  $Q = 10.52$  GeV*, Ph.D. thesis, UIUC (2013).
- [188] J. Lees *et al.*, Phys. Rev. D **88**, 032011 (2013), arXiv:1306.2895 [hep-ex] .
- [189] E. Hawker *et al.*, Phys. Rev. Lett. **80**, 3715 (1998), arXiv:hep-ex/9803011 .
- [190] R. Towell *et al.*, Phys. Rev. D **64**, 052002 (2001), arXiv:hep-ex/0103030 .
- [191] J. C. Webb, *Measurement of continuum dimuon production in 800-GeV/c proton nucleon collisions*, Ph.D. thesis, New Mexico State U. (2003), arXiv:hep-ex/0301031 .
- [192] S. Alekhin, K. Melnikov, and F. Petriello, Phys. Rev. **D74**, 054033 (2006), arXiv:hep-ph/0606237 .
- [193] G. Abbiendi *et al.*, Eur. Phys. J. C **16**, 407 (2000), arXiv:hep-ex/0001054 .
- [194] A. Accardi, L. T. Brady, W. Melnitchouk, J. F. Owens, and N. Sato, Phys. Rev. D **93**, 114017 (2016).
- [195] R. D. Ball *et al.*, Eur. Phys. J. C **77**, 663 (2017), arXiv:1706.00428 [hep-ph] .
- [196] A. Accardi, F. Arleo, W. Brooks, D. D'Enterria, and V. Muccifora, Riv. Nuovo Cim. **32**, 439 (2010), arXiv:0907.3534 [nucl-th] .
- [197] K. Kovarik, I. Schienbein, F. Olness, J. Yu, C. Keppel, J. Morfin, J. Owens, and T. Stavreva, Phys. Rev. Lett. **106**, 122301 (2011), arXiv:1012.0286 [hep-ph] .

- [198] N. Kalantarians, C. E. Keppel, and M. E. Christy, Phys. Rev. C **96**, 032201 (2017), arXiv:1706.02002 [hep-ph] .
- [199] M. Hirai, S. Kumano, T.-H. Nagai, and K. Sudoh, Phys. Rev. D **75**, 094009 (2007), arXiv:hep-ph/0702250 .
- [200] M. Boglione, J. Collins, L. Gamberg, J. O. Gonzalez-Hernandez, T. C. Rogers, and N. Sato, (2016), arXiv:arXiv:1611.10329 [hep-ph] .
- [201] A. Radyushkin, (2016), arXiv:arXiv:1612.05170 [hep-ph] .
- [202] A. Radyushkin, (2017), arXiv:arXiv:1701.02688 [hep-ph] .
- [203] X. Ji and P. Unrau, Phys. Rev. D **52**, 72 (1995).
- [204] N. Bianchi, A. Fantoni, and S. Liuti, Phys. Rev. D **69**, 014505 (2004).
- [205] A. Accardi, M. E. Christy, C. E. Keppel, P. Monaghan, W. Melnitchouk, J. G. Morfin, and J. F. Owens, Phys. Rev. D **81**, 034016 (2010).
- [206] J. Owens, A. Accardi, and W. Melnitchouk, Phys. Rev. D **87**, 094012 (2013).
- [207] S. A. Kulagin and A. V. Sidorov, Eur. Phys. J. A **9**, 261 (2000).
- [208] S. I. Alekhin, S. A. Kulagin, and R. Petti, Phys. Rev. D **96**, 054005 (2017).
- [209] R. Barbieri, J. R. Ellis, M. K. Gaillard, and G. G. Ross, Nucl. Phys. **B117**, 50 (1976).
- [210] N. Isgur, S. Jeschonnek, W. Melnitchouk, and J. W. Van Orden, Phys. Rev. D **64**, 054005 (2001).
- [211] J. Arrington *et al.*, Phys. Rev. D **64**, 014602 (2001).
- [212] J. Arrington, R. Ent, C. E. Keppel, J. Mammei, and I. Niculescu, Phys. Rev. D **73**, 035205 (2006).

- [213] W. Melnitchouk, Phys. Rev. D **67**, 077502 (2003).
- [214] W. Melnitchouk, R. Ent, and C. Keppel, Phys. Rep. **406**, 127 (2005).
- [215] P. E. Bosted *et al.*, Phys. Rev. C **75**, 035203 (2007).
- [216] P. Solvignon *et al.*, Phys. Rev. Lett. **101**, 182502 (2008).
- [217] C. Cocuzza *et al.*, in preparation (2021).

**VITA**

Eric Alan Moffat

Department of Physics, Old Dominion University

306 Oceanography and Physics Building

4600 Elkhorn Ave, Norfolk, VA 23529

**Education:****Old Dominion University, Norfolk, VA**

M.S. Physics, Dec 2015

**Purdue University, West Lafayette, IN**

B.S. Nuclear Engineering, Dec 2002

**Research Experience:**

2015-Present    Research Assistant, Old Dominion University, Norfolk, VA

**Publications:**

1. E. Moffat, W. Melnitchouk, T. C. Rogers, and N. Sato, Simultaneous Monte Carlo analysis of parton densities and fragmentation functions (2021), arXiv:2101.04664 [hep-ph]
2. E. Moffat, T. C. Rogers, N. Sato, and A. Signori, Collinear factorization in wide-angle hadron pair production in  $e^+e^-$  annihilation, *Phys. Rev. D* 100, 094014 (2019)
3. E. Moffat, T. C. Rogers, W. Melnitchouk, N. Sato, and F. Steffens, What does kinematical target mass sensitivity in DIS reveal about hadron structure?, *Phys. Rev. D* 99, 096008 (2019)
4. E. Moffat, W. Melnitchouk, T. C. Rogers, and N. Sato, What are the low- $Q$  and large- $x$  boundaries of collinear QCD factorization theorems?, *Phys. Rev. D* 95, 096008 (2017)  
\*Editor's Suggestion